

May 2016

# Nanostructured Organic/Inorganic Semiconductor Photovoltaics: Investigation on Morphology and Optoelectronics Performance

Aruna Wanninayake

*University of Wisconsin-Milwaukee*

Follow this and additional works at: <https://dc.uwm.edu/etd>



Part of the [Materials Science and Engineering Commons](#), and the [Physics Commons](#)

---

## Recommended Citation

Wanninayake, Aruna, "Nanostructured Organic/Inorganic Semiconductor Photovoltaics: Investigation on Morphology and Optoelectronics Performance" (2016). *Theses and Dissertations*. 1225.  
<https://dc.uwm.edu/etd/1225>

This Dissertation is brought to you for free and open access by UWM Digital Commons. It has been accepted for inclusion in Theses and Dissertations by an authorized administrator of UWM Digital Commons. For more information, please contact [open-access@uwm.edu](mailto:open-access@uwm.edu).

NANOSTRUCTURED ORGANIC/INORGANIC SEMICONDUCTOR  
PHOTOVOLTAICS: INVESTIGATION ON MORPHOLOGY AND  
OPTOELECTRONICS PERFORMANCE

by

W.T.M. Aruna Pushpa Kumara Wanninayake

A Dissertation Submitted in  
Partial Fulfillment of the  
Requirements for the Degree of

Doctor of Philosophy  
in Engineering

at

University of Wisconsin-Milwaukee

May 2016

# ABSTRACT

## NANOSTRUCTURED ORGANIC/INORGANIC SEMICONDUCTOR PHOTOVOLTAICS: INVESTIGATION ON MORPHOLOGY AND OPTOELECTRONICS PERFORMANCE

by

W.T.M. Aruna Pushpa Kumara Wanninayake

The University of Wisconsin-Milwaukee, 2016  
Under the Supervision of Professor Nidal H. Abu-Zahra

Organic solar cell is a promising technology because of the versatility of organic materials in terms of tunability of their electrical and optical properties. In addition, their relative insensitivity to film imperfections potentially allows for very low-cost high-throughput roll-to-roll processing. However, the power conversion efficiency of organic solar cell is still limited and needs to be improved in order to be competitive with grid parity. This work is focused on the design and characterization of a new organic/inorganic hybrid device to enhance the efficiency factors of bilayer organic solar cells such as: light absorption, exciton diffusion, exciton dissociation, charge transportation and charge collection at the electrodes. In a hybrid solar cell operation, external quantum efficiency is determined by these five factors. The external quantum efficiency has linear relationship to the power conversation efficiency via short circuit current density.

Bulk heterojunction (BHJ) PSCs benefit from a homogeneous donor-acceptor (D-A) contact interface compared to their inorganic counterpart. A homogenous D-A interface offers a longer free path for charge carriers, resulting in a longer diffusional pathway and a larger coulomb interaction between electrons and holes. This is triggered by the low dielectric constant of organic semiconductors. Among various conventional donor-acceptor structures, poly(3-hexylthiophene)/[6,6]-phenyl-C70-butyric acid methyl ester (P3HT/PCBM) mixture is the most

promising and ideal donor-acceptor pair due to their unique properties. In order to take benefits from both organic and inorganic materials, inorganic nanoparticles are incorporated in this donor-acceptor polymer structure.

Light trapping enhances light absorption and increases efficiencies with thinner device structure. In this study, copper oxide nanoparticles are used in the P3HT/PC70BM active layer to optimize the optical absorption properties in the blend. In addition, zinc oxide nanoparticles are used for tuning the conjugated polymer films due to their high electron accepting ability and optical absorption properties. In the zinc oxide structure, electrons exhibit higher mobility, which enhances the exciton dissociation efficiency. In addition, metal nanoparticles such as gold are added to the hole transport layer to enhance the overall hole transport ability.

The optimum morphology of P3HT/PCBM films is described by two main features: 1) the molecular ordering within the donor or acceptor phase, which affects the photon absorption and carrier mobility; and 2) the scale of phase separation between the donor and the acceptor, which can directly influence the exciton dissociation and charge transport and/or collection processes. Hence, the molecular ordering and the phase separation between the donor and acceptor phases are crucial for solar cells with high efficiency. Optimization of the morphology of the organic/inorganic hybrid layers will be achieved via thermal annealing.

The main goal of this work is to fabricate inorganic nanoparticles incorporated polymer PV devices with increased power conversion efficiency (PCE). This goal is achieved through four research objectives which are 1) enhancement of exciton generation and morphology by CuO NPs, 2) enhancement of exciton transportation and carrier diffusion by thermal annealing, 3) Improvement of exciton dissociation and electron mobility using ZnO NPs, and 4)

improvement of hole collection ability using Au NPs. The key findings in this research can be applied to fabricate solar cells with higher power conversion efficiencies.

© Copyright by W.T.M. Aruna Pushpa Kumara Wanninayake, 2016  
All Rights Reserved

# TABLE OF CONTENTS

ABSTRACT.....	ii
TABLE OF CONTENTS.....	vi
LIST OF FIGURES .....	ix
LIST OF TABLES.....	xiii
LIST OF NOMENCLATURE.....	xiv
LIST OF ABBREVIATIONS.....	xv
ACKNOWLEDGEMENTS.....	xvii
CHAPTER 1 .....	1
Introduction.....	1
1.1 Background .....	1
1.2 Research Motivation and Goals .....	3
1.3 Novelty .....	4
References .....	7
CHAPTER 2 .....	8
Physics of Organic Photovoltaics .....	8
2.1 Basic Electronic Structure of Organic Semiconductors.....	8
2.1.1 Occupation of the Energy Bands .....	9
2.2 Organic Photovoltaic Principles.....	12
2.2.1 Photon Absorption.....	15
2.2.2 Exciton Diffusion .....	19
2.2.3 Exciton Dissociation.....	22
2.2.4 Charge Carrier Transportation.....	26
2.2.5 Charge Carrier Collection.....	28
2.3 Recombination Process .....	30
2.4 Solidification Process of Polymer .....	32
2.5 Photovoltaic Parameters.....	34
References .....	38
CHAPTER 3 .....	42
Experimental Methods.....	42

3.1 Materials.....	42
3.1.1 P3HT (poly 3-hexylthiophene).....	43
3.1.2 PCBM ([6, 6]-phenyl-C71-butyric acid methyl ester).....	43
3.1.3 PEDOT: PSS (Poly (3, 4-ethylenedioxythiophene)-poly (styrenesulfonate)).....	43
3.1.4 Copper oxide, Zinc Oxide and Gold nanoparticles .....	44
3.2 Device Fabrication .....	45
3.2.1 CuO NPs incorporated P3HT/PC70BM solar cells.....	45
3.2.2 CuO and ZnO NPs incorporated P3HT/PC70BM solar cells.....	46
3.2.3 Au/PEDOT: PSS-P3HT/PCBM/CuO solar cells.....	48
3.3 Characterization .....	48
References .....	50
CHAPTER 4 .....	51
Objective 1: Enhancement of Exciton Generation and Morphology of Polymer Solar Cells by CuO NPs .....	51
4.1 Introduction .....	51
4.2 Results and Discussion.....	55
4.2.1 Performance Characteristics .....	55
4.2.2 Morphology and Surface Characteristics .....	65
4.3 Conclusions .....	73
References .....	74
CHAPTER 5 .....	76
Objective 2: Enhancement of Exciton Transportation and Carrier Diffusion in CuO Incorporated Polymer Solar Cells by Thermal Annealing .....	76
5.1 Introduction .....	76
5.2 Results and Discussion.....	78
5.2.1 Morphological Analysis .....	78
5.2.2 Optical and Electrical Properties .....	84
5.3 Conclusions .....	92
References .....	94
CHAPTER 6 .....	97
Objective 3: Improvement of Exciton Dissociation and Electron Mobility in Polymer Solar Cells Using ZnO NPs .....	97
6.1 Introduction .....	97



6.2 Results and Discussion.....	100
6.2.1 Electrical and Optical Performance .....	100
6.2.2 Annealing Effect.....	107
6.3 Conclusion.....	115
References .....	117
CHAPTER 7 .....	120
Objective 4: Improvement of Hole Collection Ability in Polymer Solar Cells Using Au NPs..	120
7.1 Introduction .....	120
7.2 Results and Discussion.....	123
7.2.1 Performance Characteristics .....	123
7.2.2 Plasmonic Effect of Au NPs in the PEDOT: PSS Layer .....	128
7.2.3 Effect of CuO NPs in the Active Layer .....	131
7.2.4 SEM and EDX Analysis .....	134
7.3 Conclusion.....	135
References .....	137
CHAPTER 8 .....	139
Conclusions and Future Work .....	139
8.1 Summary and Conclusions.....	139
8.2 Future Outlook .....	140
CURRICULUM VITAE.....	142

# LIST OF FIGURES

Figure 2.1: An illustration of simple two-level system [1] .....	8
Figure 2.2: Device architecture of a typical organic photovoltaic device .....	13
Figure 2.3: Illustration of the charge carrier generation process: (a) absorption, (b) exciton diffusion, (c) exciton dissociation, (d) charge transport and (e) charge collection [6] .....	14
Figure 2.4: Electron excitation in a molecule: a) stable molecules and b) unstable molecules with $\Delta Q$ adjustment .....	16
Figure 2.5: Schematic presentation of weak coupling regimes in ideal H- and J aggregates. The vibrationless ground state is given by $G >$ and the $v^{\text{th}}$ vibronic band and free exciton bandwidth are depicted as $ Av + 1 >$ and $W$ respectively [7] .....	18
Figure 2.6: Representation of the spectral overlap (J) of a donor (D) emission and acceptor absorption .....	20
Figure 2.7: Schematic presentation of the Exciton diffusion process at low and room temperatures [16] .....	22
Figure 2.8: Charge transfer process in organic solar cells (a) direct electron transfer to acceptor (b) Forster energy transfer from donor to acceptor [20] .....	23
Figure 2.9: Illustration of a polaron pair at the donor-acceptor interface [20] .....	24
Figure 2.10: Schematic representation of charge transport concept [6, 20] .....	27
Figure 2.11: Nongeminate recombination: (a) mobile and a trapped polaron yielding a recombination rate $\propto n$ (b) two mobile polarons yielding a recombination rate $\propto n^2$ [31] .....	31
Figure 2.12: Current density–voltage (J–V) characteristics for a generic illuminated solar cell [39] .....	34
Figure 3.1: Chemical structures of conjugated polymers .....	42
Figure 3.2: Schematic illustration of the structure of polymer solar cells .....	45
Figure 4.1: Structure of CuO crystal shown by four unit cells [2] .....	52
Figure 4.2: Calculated band structures and density of states (DOS) of CuO [2] .....	53
Figure 4.3: Current Density-Voltage characteristics of P3HT/PCBM/CuO-NPs hybrid solar cells .....	56
Figure 4.4: External quantum efficiency of P3HT/PCBM/CuO-NPs hybrid solar cells .....	57

Figure 4.5: Optical absorption spectra of P3HT/PCBM/CuO-NPs hybrid solar cell .....	58
Figure 4.6: The absorption spectra of these CuO NPs.....	60
Figure 4.7: EDX mapping showing the distribution of elemental copper in the P3HT/PCBM active layer of PSCs containing: (a) 0.2 mg, (b) 0.4 mg, (c) 0.6 mg, (d) 0.8 mg and (e) 1 mg CuO NPs.....	61
Figure 4.8: Converted EDX images with the optimized threshold.....	63
Figure 4.9: (a) Schematic band structure of the P3HT/PCBM/CuO NP active layer, (b) SEM image of the polymer solar cell.....	64
Figure 4.10: XRD pattern of CuO NPs sample.....	65
Figure 4.11: XRD spectra for CuO NPs incorporated P3HT/PCBM thin films.....	67
Figure 4.12: Crystallinity of PSC's determined by XRD and DSC-Eq: (4.9) .....	68
Figure 4.13: Crystallinity of PSC's determined by XRD and DSC-Eq: (4.10) .....	70
Figure 4.14: Effect of CuO NPs on the crystallinity and PCE of the PSCs.....	71
Figure 4.15: AFM images for P3HT/PCBM layers with (a) No CuO NPs, (b) 0.2mg CuO NPs, (c) 0.4mg CuO NPs, (d) 0.6mg CuO NPs, (e) 0.8mg CuO NPs, (f) 1mg CuO NPs.....	72
Figure 5.1: Schematic illustration of internal structure of thin films.....	76
Figure 5.2: XRD spectra for CuO NPs incorporated P3HT/PCBM thin films after annealing ....	78
Figure 5.3: Diffraction peak intensity before and after annealing .....	79
Figure 5.4: Effect of CuO NPs on crystallite size ( $L$ ) after thermal annealing.....	80
Figure 5.5: Percent crystallinity before and after annealing .....	82
Figure 5.6: AFM images for annealed P3HT/PCBM layers with (a) No CuO NPs, (b) 0.2mg CuO NPs, (c) 0.4mg CuO NPs, (d) 0.6mg CuO NPs, (e) 0.8mg CuO NPs, (f) 1mg CuO NPs ...	83
Figure 5.8: Optical absorption intensities from UV-vis spectroscopy before and after annealing	85
Figure 5.7: Optical absorption spectra after annealing .....	87
Figure 5.9: Effect of annealing on the EQE values of PSCs with CuO NPs .....	88
Figure 5.10: PCE of P3HT/PCBM/CuO-NPs hybrid solar cells before and after annealing .....	90
Figure 5.11: $J_{sc}$ and $V_{oc}$ of P3HT/PCBM/CuO-NPs hybrid solar cells after annealing .....	91

Figure 6.1: (a) The wurtzite crystal structure of ZnO with the lattice parameters $a$ and $c$ indicated and (b) the calculated band structure of ZnO using the HSE hybrid functional .....	97
Figure 6.2: Graphical representation of the hybrid device architecture (a) Layer structure with ZnO buffer layer, (b) energy level diagram .....	101
Figure 6.3: AFM images of active layer ( $2 \times 2 \mu\text{m}^2$ scans) with (a) P3HT/PCBM/CuO-0.6mg NPs (sample A), (b) P3HT/PCBM/CuO-0.6mg NPs with 20mg of ZnO NPs buffer layer (sample C), and (c) P3HT/PCBM/CuO-0.6mg NPs with 40mg of ZnO NPs buffer layer (sample E) .....	102
Figure 6.4: Optical absorption spectra of the hybrid solar cells with CuO and ZnO NPs .....	103
Figure 6.5: EQE of the hybrid solar cells with ZnO buffer layer .....	104
Figure 6.6: $J$ - $V$ characteristics of hybrid polymer solar cells ZnO buffer layer .....	106
Figure 6.7: $J$ - $V$ characteristics of hybrid polymer solar cells ZnO buffer layer after annealing .....	108
Figure 6.8: Effect of thermal annealing on the EQE values of PSCs with ZnO buffer layer .....	110
Figure 6.9: Optical absorption spectra of PSCs with CuO and ZnO NPs before and after annealing .....	111
Figure 6.10: XRD pattern of ZnO NPs sample .....	112
Figure 6.11: XRD spectra for 0.6 mg of CuO NPs incorporated P3HT/PCBM thin films .....	113
Figure 6.12: AFM images (2D) of active layer: (a) P3HT/PC70BM/0.6mg CuO NPs (b) P3HT/PCBM/CuO-0.6mg NPs with 20mg of ZnO NPs buffer layer (c) P3HT/PCBM/CuO-0.6mg NPs with 20mg of ZnO NPs buffer layer after annealing .....	114
Figure 7.1: (a) Schematic indication of surface plasmon resonance on plasmonic nanoparticles [5] and (b) an illuminated nanoparticle .....	121
Figure 7.2: $J$ - $V$ characteristics of hybrid polymer solar cells with different amount of Au NPs in PEDOT: PSS layer .....	124
Figure 7.3: EQE of the hybrid solar cells with various Au NPs concentrations in PEDOT: PSS .....	125
Figure 7.4: EQE and $J_{sc}$ of the hybrid solar cells .....	126
Figure 7.5: Optical absorption spectra of the hybrid solar cells with various Au NPs concentrations in PEDOT: PSS layer .....	127
Figure 7.6: Electric field distribution in the PEDOT:PSS:Au NPs/ P3HT:PCBM PSCs [12] ...	128

Figure 7.7: AFM images (non-contact mode) of PEDOT:PSS layers ( $2 \times 2 \mu\text{m}$ scans) with (a) No Au NPs, (b) 0.02 mg Au NPs, (c) 0.06 mg Au NPs, (d) 0.10 mg Au NPs, (e) 0.14 mg Au NPs, (f) 0.18 mg Au NPs.....	130
Figure 7.8: Energy band diagram of the P3HT/PCBM/CuO NPs device [17] .....	133
Figure 7.9: (a) EDX mapping showing the distribution of Au NPs in the PEDOT: PSS layer (b) SEM image of the hybrid polymer solar cell (c) EDX mapping showing the distribution of elemental copper in the P3HT/PCBM active layer.....	135

## LIST OF TABLES

Table 2.1: The state of the reported electrical parameters of polymer solar cells .....	37
Table 3.1: Impurity level in the nanoparticle samples in ppm: (a) CuO NPs, (b) ZnO NPs, and (c) Au NPs .....	44
Table 4.1: Performance parameters of P3HT/PCBM/CuO-NPs hybrid solar cells .....	55
Table 5.1: Comparison of roughness values of the PSCs before and after annealing .....	84
Table 5.2: Comparison of maximum light absorption intensities of the CuO NPs and the P3HT/PCBM/CuO NPs active layer before and after annealing .....	86
Table 5.3: Performance parameters of P3HT/PCBM/CuO-NP hybrid solar cells before and after annealing (B/A: before annealing, A/A: after annealing) .....	89
Table 6.1: Electric parameters of ITO/PEDOT:PSS P3HT/PCBM/CuO-0.6mg NPs/ZnO NPs/ Al solar cells. ....	105
Table 6.2: Performance parameters of PEDOT:PSS/P3HT/PCBM/CuO-NPs/ZnO NPs hybrid solar cells before and after heat treatment 200°C for 30 minutes (B/A: before annealing, A/A: after annealing) .....	107
Table 6.3: Performance characteristics of polymer solar cells with different annealing temperatures .....	109
Table 7.1: Device parameters of ITO/PEDOT:PSS (with Au-NPs)/P3HT/PCBM/ CuO-0.6 mg NPs/Al solar cells.....	124
Table 7.2: The root-mean-square roughness $\sigma_{rms}$ (nm) values of the Au NPs added PEDOT: PSS layers .....	130

## LIST OF NOMENCLATURE

$C$	Velocity of light
$E_g$	Energy band gap
$h$	Planck's constant
$q$	Charge of the carriers
$\Delta H_c$	Enthalpy of crystallization
$\Delta H_m$	Enthalpy of melting
$\Delta H$ or $\Delta H_m^o$	Enthalpy of 100% crystalline polymer
$\eta$	Power conversion efficiency
$\eta_A$	Photon absorption efficiency
$\eta_{cc}$	Charge collection yield
$\eta_{tr}$	Charge carrier transport yield
$\eta_{diff}$	Exciton diffusion yield
$\eta_{diss}$	Exciton dissociation yield
$\lambda$	Wavelength
$\sigma_{rms}$	Root mean square roughness
$k_B$	Boltzmann constant
$K_{D \rightarrow A}^F$	Forster transfer rate
$\nu$	Frequency
$n$	Density of free electrons
$N$	Avogadro constant
$N_A$	Doping density

## LIST OF ABBREVIATIONS

J-V curve	Current density-voltage curve
AM1.5G	Air Mass 1.5 Global
PCE	Power conversion efficiency
$J_{sc}$	Short-circuit current density
$V_{oc}$	Open-circuit voltage
FF	Fill factor
EQE	External quantum efficiency
IQE	Internal quantum efficiency
IPCE	Incident photon-to-electron conversion efficiency
$P_{in}$	Incident power density
BHJ	Bulk heterojunction
CT	Charge-transfer
DA	Donor-acceptor
DOS	Density of states
HOMO	Highest occupied molecular orbital
LUMO	Lowest unoccupied molecular orbital
MO	Molecular orbital
PV	Photovoltaic
XPS	X-ray photoelectron spectroscopy
XRD	Single crystal X-ray diffraction
AFM	Atomic Force Microscopy



PL	Photoluminescence
RMS	Root mean square

## **ACKNOWLEDGEMENTS**

I would like to express my sincere appreciation and deepest gratitude to my advisor, Professor Nidal Abu-Zahra, for introducing an important research field to me and for immense encouragement, guidance, and support given throughout the research to succeed this event. I believe, the skills that I have learnt from him have largely contributed to make me a better researcher. I am very grateful to my co-advisor Professor Benjamin C. Church, for his comments, encouragement and support for my work in every possible way to make my study a success.

I am also grateful to my committee members, Prof. Pradeep Rohatgi, Prof. Junhong Chen, and Prof. Wilkistar Otieno, for serving on my doctoral committee and reviewing the dissertation. Their suggestions, patience and intellectual contributions have helped me complete my dissertation successfully. I extend my special thanks to Prof. Junhong Chen for providing me with research facilities in his solar cell simulation lab.

I would like to thank Dr. H. A. Owen at the Biology Department at University of Wisconsin-Milwaukee for technical support with SEM analyses and thermal evaporator coating. I would also like to thank Dr. Steven Hardcastle for providing me with equipment facilities in his lab. He helped me a lot with equipment training, techniques and related issues throughout my research. I am pleased to acknowledge with gratitude the worthy assistance offered to me by Dr. Mahmoud Algazzar at the beginning of my research. I am very grateful to doctoral student Xiaoru Guo for his assistance to characterize the solar cell devices. I would like to express my gratitude to Dr. Subhasini Gunasekar and doctoral student Shengyi Li for their assistance,

corporation and support to me in numerous ways. My sincere thanks also go to my friends giving me courage and help during my research period.

# CHAPTER 1

## Introduction

### 1.1 Background

Bulk heterojunction polymer solar cells (PSCs), which are based on solution-processed conjugated polymer donor (P3HT: poly 3-hexylthiophene) and fullerene derivative acceptor (PCBM: [6, 6]-phenyl-C71-butyric acid methyl ester) materials, have attracted much attention due to their advantages of easy fabrication, simple device structure, low cost, light weight, and capability to be fabricated into flexible devices [1]. In addition, they can have high optical absorption coefficients which offer the possibility of production of very thin solar cells. On the other hand, inorganic semiconductors possess better electronic properties, such as high dielectric constant, extremely high optical absorption, high charge mobility, and better thermal stability. The nanoparticles of these inorganic semiconductors exhibit even better electronic, optical, photoconducting, and luminescent properties [2].

The oxides of transition metals are an important class of semiconductors having applications in multiple technical fields such as solar energy transformation. Among transition metal oxides, copper oxide nanoparticles (CuO NPs) are of special interest as they are of low cost, non-toxic, and have high optical absorption capabilities. CuO is a p-type semiconductor which has a band gap energy of 1.5 eV and this value is close to the ideal energy gap of 1.4 eV required for solar cells to allow good solar spectral absorption. The ZnO is also a well-known and attractive semiconductor material in photovoltaic applications [3]. The n- type ZnO is a direct band gap semiconductor with a band gap of 3.44 eV and strong electron acceptor with high electron mobility, high thermal conductivity, wide and direct band gap and large exciton

binding energy [3]. These properties make ZnO suitable for a wide range of devices, including photovoltaic cells.

Furthermore, the metal nanoparticles such as Au, can be used in conjugated polymer films as light-scattering centers which facilitate efficient charge collection at the electrodes. The combine effect of these nanoparticles in the PEDOT: PSS/P3HT/PC70BM devices may result in higher power conversion efficiency (PCE) of the solar cell. In order to take advantages of both organic and inorganic materials, nanoparticles of inorganic semiconductors can be combined with semiconducting polymers. The combined absorption bands of both materials can yield better sun energy harvest in hybrid photovoltaic-cell [4].

To achieve high PCE, the photovoltaic device should possess five crucial factors which are photon absorption, exciton diffusion, exciton dissociation, charge carrier transport, and charge collection. Sunlight photons which are absorbed inside the device excite the donor molecule, leading to the creation of excitons. Efficient conversion of solar energy requires the compounds to absorb strongly in the visible region of the spectrum [5]. However, the acceptor phase can also absorb light, but for simplicity only the photons that are absorbed by the donor phase are considered here. The created excitons start to diffuse within the donor phase and if they encounter the interface with the acceptor then a fast dissociation takes place leading to charge separation. The resulting metastable electron-hole pairs across the D/A interface may still be Coulombically bound and an electric field is needed to separate them into free charges. Therefore, at typical operation conditions, the photon-to-free-electron conversion efficiency is not maximal. Subsequently, the separated free electrons/holes are transported with the aid of the internal electric field, caused by the use of electrodes with different work functions, towards the cathode/anode where they are collected by the electrodes and driven into the external circuit [6].

Compared to inorganic solar cells, PSCs usually have insufficient light absorption due to the thin active layer which is restricted by the short exciton diffusion length and low carrier mobility. The idea behind a heterojunction is to use two materials (donor and acceptor) with different electron affinities and ionization potentials [7]. At the interface, the resulted potentials are strong and may favor exciton dissociation: the electron will be accepted by the material with the larger electron affinity and the hole by the material with the lower ionization potential, provided that the differences in potential energy are larger than the exciton binding energy. The photo-induced charge separation mainly occurs at the interfaces between inorganic semiconductors and conducting polymers, where electrons are injected from the conducting polymers into inorganic semiconductors and holes remain in the polymers. This interfacial charge separation is capable of preventing the recombination of separated electrons and holes [8].

## **1.2 Research Motivation and Goals**

As the global energy demand continues to increase every year, the limiting supply of the current main energy sources (oil, coal, uranium) and their detrimental long-term effects on the natural balance on our planet, underscore the urgency of developing renewable energy sources. The renewable energy sources which neither run out nor have any significant harmful effects on the environment. Harvesting energy directly from the sunlight using photovoltaic (PV) technology is being widely recognized as an essential component of future global energy production.

A great deal of research has been implemented on fabricating different photovoltaic devices to extract sun energy which are based on organic and inorganic semiconductors.

However, there are still critical drawbacks of the PCE due to insufficient photon absorption, low carrier mobility and less exciton dissociation. Further studies are needed to find ways and means to solve these problems.

The main goal of this research is to design inorganic nanoparticles incorporated polymer PV devices with increased power conversion efficiency (PCE) through enhancing the efficiency factors of photon absorption, exciton diffusion, exciton dissociation, charge carrier transport, and charge collection. A secondary goal is to understand and explain the effect of inorganic nanoparticles (CuO, ZnO and Au NPs) on power conversion efficiencies of the organic/inorganic hybrid devices.

### **1.3 Novelty**

Previous studies [7, 8] of hybrid solar cells have directly incorporated inorganic nanoparticles (INPs) as electron acceptors (ZnO, TiO<sub>x</sub>, or CdSe INPs), light-harvesting absorbers, or light-scattering centers (Au, Ag, or CdSe INPs) in conjugated polymer film. Compared to these inorganic NPs, CuO NPs have excellent electronic and optical properties including high light absorption in the range of visible region. Since CuO is a photogenerating material it will inject the excess electrons to the structure. Hence, P3HT donor property could be tuned by generating electrons from the CuO NPs. However, to the best of our knowledge, there is no published work on the use of CuO NPs to improve the light absorption in the P3HT/PCBM active layer.

The charge injecting possibility from the photo active layer to the electrodes is represented by the charge collection efficiency. The magnitude of the conduction band energy level of the acceptor material is a critical parameter for better electron injection into the cathode.

For possible electron injecting, this should be lower than the work function of donor. Correspondingly, the magnitude of conduction band energy level should be greater than the work function of the anodic material for possible hole injection to anode. Considering the conduction and valence band energy levels of CuO and ZnO, they are most suitable for donor and acceptor pair. The electron accepting property of ZnO could modify the PC70BM material providing better exciton dissociation efficiency. Furthermore, the metallic nanoparticles such as Au NPs contribute to reflect and scatter the light increasing the optical absorption in the thin films. However, no conclusive work has been conducted to study the role of CuO, ZnO and Au NPs in the P3HT/PC70BM thin film solar cells. This study will be revealing the phenomena behind this.

The morphology of the polymer film is also an important factor to maximize the power conversion efficiency of the active films, as it describes the energy level, band gap and the hole mobility of the conjugated polymer. In general, morphology in materials research is the study of forms comprising shape, size, and structure. For nanostructured materials, morphology has special significance since the form of nanoparticles dictates physical and chemical properties [9, 10]. Unlike bulk materials, properties of nanomaterials are strongly correlated to shape, which is attained during growth through a self-assembling process dictated by the interplay of size and molecular interactions [10, 11]. Deviations from bulk properties become prominent as the size of nanomaterials starts to be comparable to the size of constituent molecules or to some other characteristic length scale like electron mean-free path [9]. In a typical application, one deals with a collection of nanomaterials, which may be dispersed in a matrix [12] forming a composite material. Compared to their inorganic counterparts, the key challenges of nanoparticles incorporated P3HT/PCBM thin films are high exciton binding energy and the short diffusion



length of excitons. To overcome these, the tailoring of the internal morphology of the active layer is as important as the electronic properties of the polymers.

The optimum morphology of P3HT/PCBM films describes two main features: 1) the molecular ordering within the donor or acceptor phase, which affects the photon absorption and carrier mobility; and 2) scale of phase separation between the donor and the acceptor, which can directly influence the exciton dissociation and charge transport and/or collection processes [13]. The aforementioned factors are crucial for solar cells with high performance efficiency. Therefore, optimization of the morphology of CuO NPs incorporated P3HT/PCBM thin films by thermal annealing will be investigated. In this study the focus is on the influence of external parameters; such as materials, composition, solvents and annealing, on the formation of the surface and internal morphology and its influence on spectroscopic properties and photovoltaic performance. The morphology of the active layer is probed with imaging and scattering techniques. The following key questions are addressed in this work: how can the morphology of the active layer in an organic solar cell be controlled? And to what extent does the morphology influence the efficiency of the active layer? In addition, this will be the first demonstration that P3HT/PCBM thin films with added CuO NPs can be tuned by thermal annealing treatment.

## References

- [1] Abu-Zahra N. and Algazzar M, 2013. Effect of Crystallinity on the Performance of P3HT/PC70BM/n-Dodecylthiol Polymer Solar Cells. *J. Sol. Energy Eng.* 136(2):021023.
- [2] Kim, C.H., Cha, S.H., Kim, S.C., Song, M., Lee, J., Shin, W.S., Moon, S.J., Bahng, J.H., Kotov N.A., Jin S.H., 2011. Silver nanowire embedded in P3HT: PCBM for high-efficiency hybrid photovoltaic device applications. *ACS Nano.* 5: 3319-3325.
- [3] Wanninayake A. P., Gunashekar S., Li S., church B.C., Abu-Zahra N., 2015 CuO Nanoparticles Based Bulk Heterojunction Solar Cells: Investigations on Morphology and Performance. *J. Sol. Energy Eng.* 137: 031016.
- [4] Thompson, B.C., and Frechet, J. M. J., 2008. Polymer–Fullerene Composite Solar Cells. *Angewandte Chemie.* 47: 58–77
- [5] Chou S. Y., and Ding W., 2013. Ultrathin, high-efficiency, broad-band, omni-acceptance, organic solar cells enhanced by plasmonic cavity with subwavelength hole array. *Opt. Express.* 21: 60-76
- [6] Jin, S., Naidu, B.V.K. Jeon, H. Park, S. Park, J., Kim, S.C., Lee, J.W., and Gal, Y., 2007. Optimization of process parameters for high-efficiency polymer photovoltaic devices based on P3HT: PCBM system. *Solar Energy Materials and Solar Cells.* 91: 1187–1193.
- [7] Beek, W. J. E., Wienk, M. M., and Janssen, R. A. J., 2004. Efficient Hybrid Solar Cells from Zinc Oxide Nanoparticles and a Conjugated Polymer. *Advanced Materials.* 16(12): 1009-1013.
- [8] Wright M., and Uddin A., 2012. Organic-inorganic hybrid solar cells: A comparative review. *Solar Energy Mater. Solar Cells.* 107: 87–111.
- [9] Bundgaard E., Shaheen S.E., Krebs F.C., Ginley D.S., 2007. Bulk heterojunctions based on a low band gap copolymer of thiophene and benzothiadiazole. *Solar Energy Materials and Solar Cells.* 91: 1631–1637.
- [10] Bundgaard E., Shaheen S.E., Krebs F.C., Ginley D.S., 2007. Bulk heterojunctions based on a low band gap copolymer of thiophene and benzothiadiazole. *Solar Energy Materials and Solar Cells.* 91: 1631–1637.
- [11] Gunes S, Neugebauer H, and Sariciftci N S, 2007. Conjugated Polymer-Based Organic Solar Cells. *Chemical Reviews.* 107: 1324-1338.
- [12] Hollingsworth, M. D. 2002. Crystal engineering: from structure to function. *Science.* 295: 2410.
- [13] Nguyen B.P., Kim T., and Park C.R. 2014. Nanocomposite-Based Bulk Heterojunction Hybrid Solar Cells. *J. Nanomater.* 2014:243041

## CHAPTER 2

### Physics of Organic Photovoltaics

#### 2.1 Basic Electronic Structure of Organic Semiconductors

Both organic and inorganic semiconductors are characterized in terms of charge carrier transport between two quasi-continua of energy levels. The energetically lower quasi-continuum level is fully occupied by electrons, whereas the upper one is nearly empty at  $T=0$  K. They are separated by an energy gap ( $E_g$ ) which is equal to  $k_B T$  at average temperatures  $T$ . At room temperature this energy gap is nearly equal to 0.26 meV [1]. Therefore, an electron transition from the lower level to the upper level by thermal excitation is impossible at room temperature. In the region within the lower and upper levels (quasi-continua), there are no available quantum levels. This region is called forbidden region with energy gap  $E_g$  as shown in the Figure 2.1 [1].

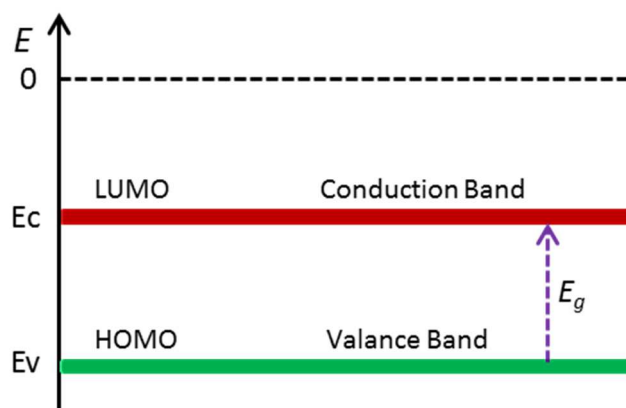


Figure 2.1: An illustration of simple two-level system [1]

In perfectly crystallized ideal inorganic semiconductor, the valence band (lower level) is delocalized over the whole material. In the organic semiconductors, the primitive units are molecules which have weak Van-der-Waals coupling bonds leading to lower delocalization of

the energy levels. These energy bands are created due to the occupied binding orbitals of the single molecules which are called molecular orbitals (MO). The highest occupied molecular orbital (HOMO) and the lowest unoccupied molecular orbital (LUMO) in the organic semiconductor are set to the valence band in inorganic semiconductors and conduction band respectively. Here HOMO is represented by the lower energy level of the donor material while the LUMO is represented by the upper energy level of the acceptor material of donor-acceptor (D/A) dual system in the organic solar cells [1].

### 2.1.1 Occupation of the Energy Bands

The occupation of the upper energy level is very low in the dark condition (radiation of 300 K) and under thermally equilibrium state. The Fermi-Dirac statistic describes the probability of occupation  $f_F(E)$  of an electron (half-integer spin particles when neglecting mutual interaction) with energy  $E$  [2];

$$f_F(E) = \frac{1}{\exp\left(\frac{E-E_F}{k_B T}\right)+1} \quad (2.1)$$

where  $E_F$  is the Fermi energy.

The occupied number  $n$  of electrons per unit volume within the energy levels of  $[E, E + dE]$ , is given by integral in energy over the product of states occupation probability  $f_F(E)$  and the density of states  $D_e(E)$  in this energy interval. The electron density between  $E$  and  $(E + dE)$  can be expressed as [2];

$$d_n(E) = \int D_e(E) f_F(E) dE \quad (2.2)$$

The  $D_e(E)$  describes the number of occupied electrons in a distinct energy level within an arbitrary volume of the semiconductor material. To have a clear idea about density of state of  $D_e$

( $E$ ), a simple model of free electron gas in three-dimensional space can be considered. The solution of the stationary Schrödinger equation of an electron in a box with edge length  $L$  in real space can be written as [2],

$$-\frac{\hbar^2}{2m}\nabla^2\psi(\vec{r}) + V(\vec{r})\psi(\vec{r}) = E\psi(\vec{r}) \quad (2.3)$$

The general solution represents an electron wave of the form  $\exp(\pm k \cdot r)$ . Electric field ( $\epsilon$ ) can accelerate an electron wave packet and the energy can be obtained as;

$$a = -\frac{q\epsilon}{\hbar^2} \frac{d^2 E}{dk^2} \quad (2.4)$$

$$\frac{dE}{dk} = \frac{\hbar^2 k}{m^*} \quad (2.5)$$

The free electron mass can be replaced by effective mass which incorporates the electronic interactions with the lattice.

$$m^* = \frac{\hbar^2}{d^2 E / dk^2} \quad (2.6)$$

Here,  $k$  is the wave vector and  $k = 2\pi/L$ , which results directly from the solution of the stationary Schrödinger equation. Hence for allowed  $k$ -value in three dimensions, the volume is  $(2\pi/L)^3$ . Considering a sphere in  $k$ -space, the number of allowed states  $N$  can be written as the ratio between the volume of the sphere and the volume of  $k$ -value. For counting the degeneracy of the spin this should be multiplied by two [1, 2].

$$N(k) = \frac{\frac{4}{3}\pi k^3}{\frac{2\pi}{L}^3} \cdot 2 = \frac{V k^3}{3\pi^2} \quad (2.7)$$

Where,  $V=L^3$  represents the real space crystal volume. Replacing  $k$  in Equation 2.7 with energy  $E$ ,

$$\frac{dN}{dE} = \frac{d\left\{\frac{V}{3\pi^2}\left(\frac{2m^*E}{\hbar^2}\right)^{3/2}\right\}}{dE} = \frac{V}{2\pi^2} \left(\frac{2m^*}{\hbar^2}\right)^{3/2} E^{1/2} = D_e(E)V \quad (2.8)$$

Using equation 2.2, the density of electrons  $n$  ( $n=N/V$ ) in the conduction band can then be calculated.

$$n = \int_{E_c}^{\infty} D_e(E) f_F(E) dE \approx \int_{E_c}^{\infty} 4\pi \left( \frac{2m^*}{h^2} \right)^{3/2} (E - E_c)^{1/2} \frac{1}{\exp \frac{E - E_F}{k_B T} + 1} dE$$

$$= N_c \exp \left( -\frac{E_c - E_F}{k_B T} \right) \quad (2.9)$$

where,  $N_c = 2 \left( \frac{2\pi m^* k_B T}{h^2} \right)^{3/2}$  is effective density of state and  $E_c$  is the energy of the conduction band edge. The equation can be used for smaller  $n$  compared to  $N_c$ . Using similar methods, the density of holes  $p$  which is unoccupied electron states in the valance band can be obtained [1, 2].

$$p = \int_{-\infty}^{E_v} D_e(E) [1 - f_F(E)] dE = N_v \exp \left( -\frac{E_F - E_v}{k_B T} \right) \quad (2.10)$$

The  $N_v$  is the effective density of state of the valence band and  $E_v$  is the energy of the valence band edge.

Hence, the production of electrons and holes densities can be expressed as,

$$np = n_i^2 = N_c N_v \exp \left( -\frac{E_c - E_v}{k_B T} \right) = N_c N_v \exp \left( -\frac{E_g}{k_B T} \right) \quad (2.11)$$

In the intrinsic semiconductors, occupation of the conduction band is a result from thermal excitation of electrons from the valence to conduction band. Therefore, intrinsic semiconductors have equal electron and hole densities ( $n = p = n_i$ ) in the relevant energy levels.

Under the illuminated condition, electron in the valance band can absorb energy photons which exceed the  $E_g$  energy gap and excited to the conduction band leaving a hole in the valence band. Hence, electrons and holes densities will be increased with same amounts as determined by the charge carrier generation rate  $G$ . Therefore, this system cannot be described by above Equation (2.11). The Boltzmann statistics associated with two separate quasi-Fermi energies for

electrons and holes will address new system. The corresponding densities of electrons and holes can be expressed as:

$$n = N_c \exp\left(-\frac{E_c - E_{F,c}}{k_B T}\right) \quad (2.12)$$

$$p = N_v \exp\left(-\frac{E_{F,v} - E_v}{k_B T}\right) \quad (2.13)$$

Here  $E_{F,c}$  and  $E_{F,v}$  are the quasi-Fermi energy levels (QFL) for electrons and holes respectively.

The production of electrons and holes densities can be expressed as [2],

$$np = N_v N_c \exp\left(-\frac{E_c - E_v}{k_B T}\right) \exp\left(-\frac{E_{F,c} - E_{F,v}}{k_B T}\right) = n_i^2 \exp\left(-\frac{E_{F,c} - E_{F,v}}{k_B T}\right) \quad (2.14)$$

The opposite process of the generation is charge carrier recombination  $R$ . This electron-hole pair annihilation generally occurs when the excited electron-hole pairs recombine back to the ground state before they fully dissociate into free charge carriers. This process is known as geminate recombination. Even after dissociation, the free holes and electrons can recombine each other and come back to the ground state which is called nongeminate recombination. In both cases the incident photon energy is lost and few charge carriers are contributed to the photocurrent [3].

## 2.2 Organic Photovoltaic Principles

The organic photovoltaics represent the carbon molecule based optoelectronic devices which convert light to electricity. These organic photovoltaics cells purely made of organic compounds as well as hybrid solar cells which combine organic and inorganic materials. The organic photovoltaic devices consist of a multilayer structure including cathode, active layer, hole transport layer and anode. A layer structure of typical photovoltaic device is shown in

Figure 2.2. Conducting and transparent glass substrates like indium tin oxide (ITO) are used for the anode. The cathode material should be a metal layer. The hole transport layer is composed of conducting polymer which can be modified by optical spaces to improve the solar cell efficiency. The main layer of the device is the active layer in which the incident light is directly converted to charge carriers. The input light photons to the solar cell through transparent electrode are absorbed by the active layer.

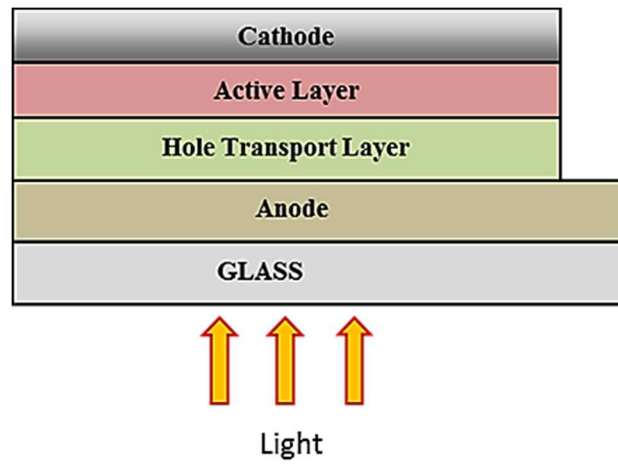


Figure 2.2: Device architecture of a typical organic photovoltaic device

Most of the organic semiconductors in the active layer are conjugated polymers such as polythiophenes, polyphenylenevinylenes and polypyrrols. These conjugated polymers consist of a backbone with alternating single and double bonds resulting in bonding ( $\pi$ ) and anti-bonding ( $\pi^*$ ) orbital states which are energetically separated within a few eV. These states form the HOMO and the LUMO with an energy gap  $E_g$  in the range of 1.5 eV to 3 eV [4]. However, the electrons-holes generation in the active layer is a multi-step complex process due to the high exciton binding energies ( $\sim 0.5$  eV) as well as a short exciton diffusion length ( $\sim 10$  nm) [5]. Figure 2.3 shows this process schematically.



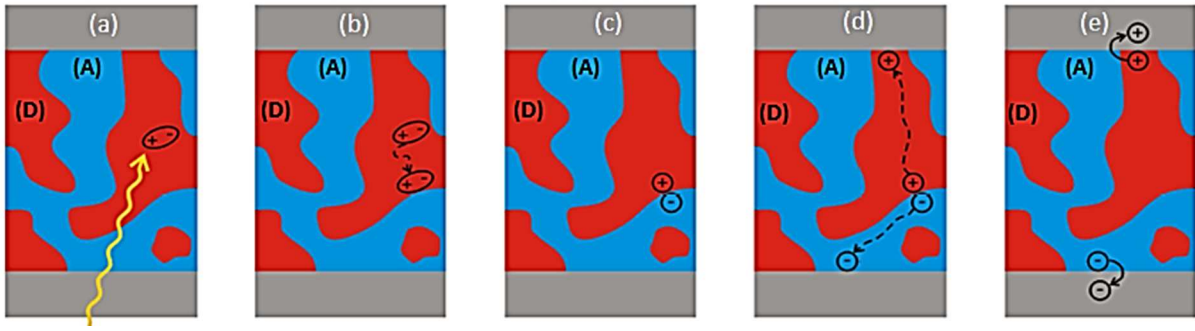


Figure 2.3: Illustration of the charge carrier generation process: (a) absorption, (b) exciton diffusion, (c) exciton dissociation, (d) charge transport and (e) charge collection [6]

After light incident on the active layer, an energy photon is absorbed by an organic donor semiconductor generating an exciton to the structure. Self-exciton dissociation probability in the pure donor material is very low due to the high exciton binding energy. Therefore, an acceptor material should be included in the structure to form an n-type and p-type interface between the molecules. The generated exciton has to diffuse to this D/A interface to dissociate and after the exciton dissociation, the separated charge carriers are transported to the electrodes. Interpenetrating blends of donor acceptor semiconductors are much better than the bilayer system due to their high exciton binding energy and short exciton diffusion length [6]. The electrodes can collect the charge carriers and direct to an external circuit. These five steps strongly affect the power conversion efficiency (PCE) of organic photovoltaic devices.

### 2.2.1 Photon Absorption

The photoelectron generation process initiates with the photon absorption in all kind of solar cells as shown in Figure 2.3a. In the organic materials, after absorbing a photon, electron is excited from the HOMO energy level to the LUMO energy level. The energy of the incident photon  $E = h\nu = hc/\lambda$  should exceed the  $E_g$  value for successful electron transition from HOMO to LUMO. The Einstein's absorption coefficient ( $B_{lu}$ ) determines the probability of exciting an electron by absorbing an energy photon. If an electron is exciting from a lower electronic state  $l$  to an upper electronic state  $u$  [6] the Einstein's absorption coefficient can be written as,

$$B_{lu} = \frac{c}{n} \int \frac{\sigma(\nu)}{h\nu} d\nu \quad (2.15)$$

where  $c/n$  represents the speed of light in a material with refractive index  $n$ ,  $h$  is Planck's constant and  $\nu$  the frequency of the photons.  $\sigma(\nu)$  is the cross section to capture a photon. The relationship of this cross section to the extinction coefficient  $\epsilon(\nu)$  can be expressed as [6],

$$\sigma(\nu) \propto \epsilon(\nu) \quad (2.16)$$

Imaginary part of the complex refractive index represents the extinction coefficient  $\epsilon(\nu)$  which describes the attenuation of light in a material. Ignoring the scattering effect,  $\epsilon(\nu)$  is equal to the absorption coefficient  $\alpha(\nu)$  of the material. The shape of the absorption spectra of organic molecules is determined by the type of monomers and they exhibit both sharp peaks as well as extended fine structures from vibrational excitations. These fine structures arise with variation of the molecular structure which is resulted by electronic excitation in organic molecules leading to an expansion of the chemical bonds [7].

Two different electronic states with vibrational modes of a molecule are depicted in Figure 2.4. The upper band ( $u$ ) and lower band ( $l$ ) represent the electronic states and  $m$  and  $n$  are

relevant vibrational levels respectively.  $Q$  and  $E$  indicate the displacement coordinate and the energy respectively. The vertical lines of the Figure 2.4 represent the electronic transitions of a molecule.

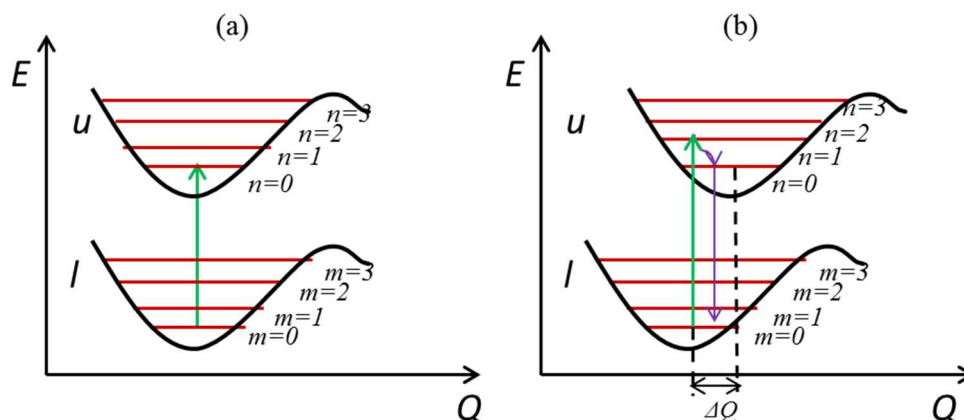


Figure 2.4: Electron excitation in a molecule: a) stable molecules and b) unstable molecules with  $\Delta Q$  adjustment

The Franck-Condon principle states that as electrons move faster than nuclei, the nuclei are effectively stationary during an electronic transition. Therefore, there is little or no geometry change in the molecular system [7].

As shown in the Figure 2.4(a), without displacement an electron is excited from the lowest vibrational state  $m = 0$  of the lower electronic level  $l$  to the lowest vibrational state  $n = 0$  of the upper electronic level  $u$ . Depending on the life time of the excited state, the absorption spectrum of these types of transition consists of a single peak with a certain width. However, the electron excitations of organic materials with certain spatial displacements allow the transitions to different vibrational states of  $n$ . The overlapped initial and the final state of wave functions indicate the probability of the electron transition [7]. The quantity  $S_{nm}$  which is the overlap-integral between the ground and excited state wavefunctions can be written as;

$$S_{nm} = \int_{-\infty}^{\infty} \psi_n^{g*}(x) \psi_m^e(x) dx \quad (2.17)$$

Here,  $\psi$  is the normalized wavefunction,  $g$  denotes the ground electronic state,  $e$  denotes the excited electronic state, and  $x$  is the bond displacement. A molecule with a different number of monomers ( $n_p$ ) shows the same shape of absorption spectra (fine structure). But after increasing the  $n_p$ , the absorption spectrum is red shifted [8].

$$\omega(n_p) = \omega_o + \frac{\Delta\omega}{n_p} \quad (2.18)$$

where  $\omega(n_p)$  is the absorption frequency.

Excitations in organic materials can be considered as Frenkel excitons (or excitonic polarons) along with a vibronically excited central molecule. This exciton contains an electron-hole pair which is bounded together with a Coulomb bond. A singlet exciton with an opposite spin is created due to the spin conservation of electrons and holes. These excitons are extended over several monomer units and the excitons binding energy generally on the order of 0.5 eV. However, the Wannier-Mott type excitons are generated in inorganic semiconductors with binding energies of about 20 meV. Due to the high binding energy, the excitons created in organic materials are not dissociated at the room temperature [9].

The intra-chain order as well as the inter-chain interactions influence on the absorption spectrum of an organic material. Interactions of two molecules change their electronic properties which are basically determined by electron exchange and Coulomb interactions. Therefore, the absorption spectrum can be altered after coupling excitations with the vibrational modes of the molecules. This phenomenon depends on the type of molecular aggregation. There are two types of aggregations called J- and H-aggregates. In J-aggregates, the dipoles are oriented in a head-to-tail fashion, and in H-aggregates, nearest-neighbor dipoles are oriented in a more side-by-side orientation [10].

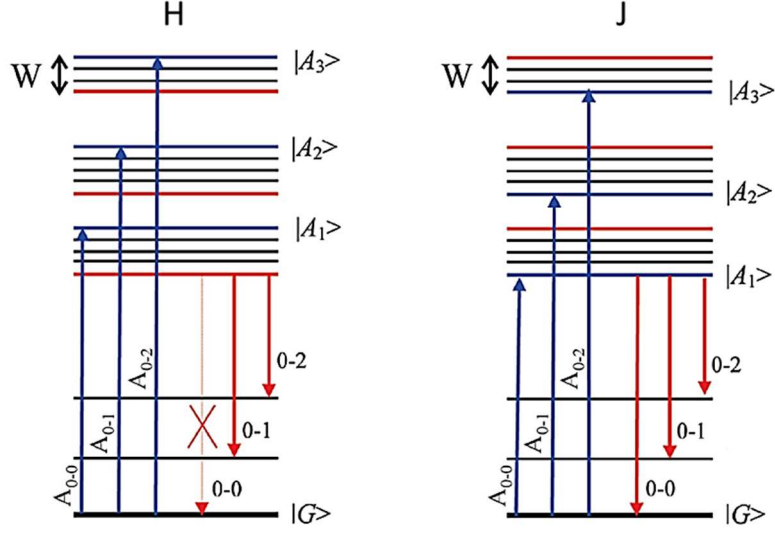


Figure 2.5: Schematic presentation of weak coupling regimes in ideal H- and J aggregates. The vibrationless ground state is given by  $|G\rangle$  and the  $v^{\text{th}}$  vibronic band and free exciton bandwidth are depicted as  $|A_{v+1}\rangle$  and  $W$  respectively [7]

The absorption spectrum of a P3HT film spun from chloroform consists two parts: a lower-energy area from regions of weakly coupled H-aggregates and a higher-energy area from the more disordered intra-chain states. Considering the relative absorbance of the 0-0 and 0-1 vibronic lines  $A_{0-0}/A_{0-1}$  the free exciton bandwidth  $W$  can be extracted [11].

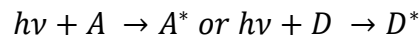
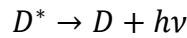
$$\frac{A_{0-0}}{A_{0-1}} = \frac{n_{0-0}}{n_{0-1}} \left[ \frac{E_p - 0.24W}{E_p + 0.07W} \right] \quad (2.19)$$

Here,  $n_{0-0}$  and  $n_{0-1}$  are refractive index at the 0-0 and 0-1 peaks, respectively. The conjugation length increment is leading to a decrease in the free exciton band width  $W$  and hence inter-chain ordering can be influenced by conjugation length of the molecules.

### 2.2.2 Exciton Diffusion

The exciton can be considered as a mobile quasi-particle with zero net charge and separation of electron-hole is essential for charge transport. However, this dissociation typically occurs at the donor and acceptor (D/A) interface due to high binding energy of the exciton at the room temperature. Therefore, the excitons generated in the donor material should be diffused to the D/A interface. The energy transfer process of the donor – acceptor molecules determines the mobility of excitons in the structure. When an exciton is diffusing in a polymer blend, excitation is taken place in the donor molecules and the excitation transferring site is the acceptor molecule [12, 13].

The energy transfer process can be divided in to two main categories which are trivial energy transfer process (or photon reabsorption) and the Forster energy (or florescence resonant energy transfer process). In trivial energy transfer process, the donor molecule emits an energy photon towards acceptor molecule and after absorbing this photon by acceptor, a new excitation is created.



Then the energy transfer rate from  $D$ - $A$  by phonon reabsorption can be expressed as [6],

$$K_{D-A} = R^{-2} \quad (2.20)$$

where  $R$  is the distance between donor and acceptor molecules.

The Forster transfer (F) is a non-radiation process which is typically used dipole – dipole coupling to transfer the energy from  $D$  to  $A$ . This non-radiative transfer of excitation energy requires some interaction between a donor and an acceptor molecule. It can occur if the emission spectrum of the donor overlaps the absorption spectrum of the acceptor.

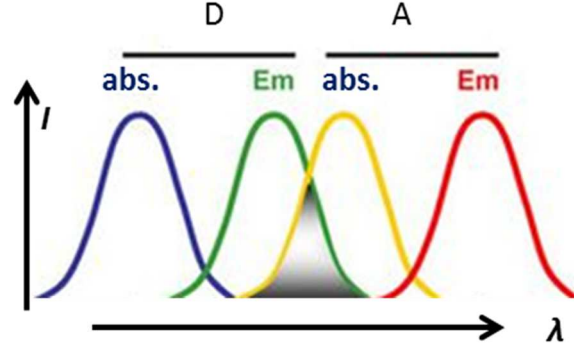


Figure 2.6: Representation of the spectral overlap ( $J$ ) of a donor (D) emission and acceptor absorption

The strength of the spectral overlap, which is distinguished by the overlap integral ( $J$ );  $J$  can be shown as,

$$J = \int_0^{\infty} I(\lambda) \epsilon(\lambda) \lambda^{-4} d\lambda \quad (2.21)$$

The Forster transfer rate can be expressed as [6, 14],

$$K_{D \rightarrow A}^F = \frac{1}{\tau_D} \left[ \frac{R_0}{R} \right]^6 \quad (2.22)$$

Here,  $\tau_D$  represents the lifetime of the donor.  $R$  is the distance between donor and acceptor.  $R_0$  is the critical transfer distance [15].

$$R_0^6 \propto k^2 \int \lambda^4 f_D(\lambda) \epsilon_A(\lambda) d\lambda \quad (2.23)$$

Here,  $f_D(\lambda)$  describes the normalized donor emission spectrum as a function of wavelength  $\lambda$ .

The  $\epsilon_A(\lambda)$  is the normalized acceptor extinction coefficient. The  $k$  is the dipole orientation factor which describes the dipole orientation between the D and A molecules.

$$K = n_D \cdot n_A - 3(n_A \cdot r)(n_D \cdot r) \quad (2.24)$$

$$K = (\cos\theta_{DA} - 3\cos\theta_D \cos\theta_A) \quad (2.25)$$

Where  $r$  is the unit vector of the direction joining donor and acceptor, and  $n_D$  and  $n_A$  are the unit vectors along the D and A transition moment directions, respectively.  $\theta_{DA}$  is the angle between the dipoles of the D and A molecules. The  $\theta_D$  and  $\theta_A$  are the angles between the corresponding dipoles and the connecting vector of molecule D and A. The  $K$  varies from 4 to 0 depending on parallel to perpendicular arrangement. In the Frost process, the transfer rate  $k_{D \rightarrow A}^F$  is maximum for the parallel dipoles of the donor and acceptor molecules. Also, the distance between the molecules has to be sufficiently low ( $R < 10$  nm) due to the  $k_{D \rightarrow A}^F = R^{-6}$  [15].

The exciton diffusion can be explained based on the energy migration process. The exciton diffusion can be interpreted as a random hopping-like motion that leads to spreading from the areas of high concentration to the areas of low concentration. Generally diffusion can be described by the following equation [16]:

$$\frac{\partial n}{\partial t} = D \nabla^2 n - \frac{n}{\tau} \quad (2.26)$$

where  $n$  is the particles concentration,  $D$  is the diffusion coefficient,  $\nabla^2$  is the Laplace operator, and  $\tau$  is the exciton lifetime which is in the range of ns. The root mean square displacement of a particle from its initial position due to the diffusion process is called diffusion length ( $L_D$ ). The  $L_D$  can be written as:

$$L_D = \sqrt{\frac{\sum dL_i^2}{N}} = \sqrt{2DZ\tau} \quad (2.27)$$

Here,  $dL_i$  represents an  $i$ th exciton displacement from its initial position,  $N$  is the total number of excitons, and  $Z$  is the dimensionality of the diffusion. However, exciton diffusion in organic semiconductors, the factor of two is ignored as:

$$L_D = \sqrt{DZ\tau} \quad (2.28)$$



In a disordered material, the  $L_D$  value approximately gives the average displacement of an exciton from its initial position [16-18].

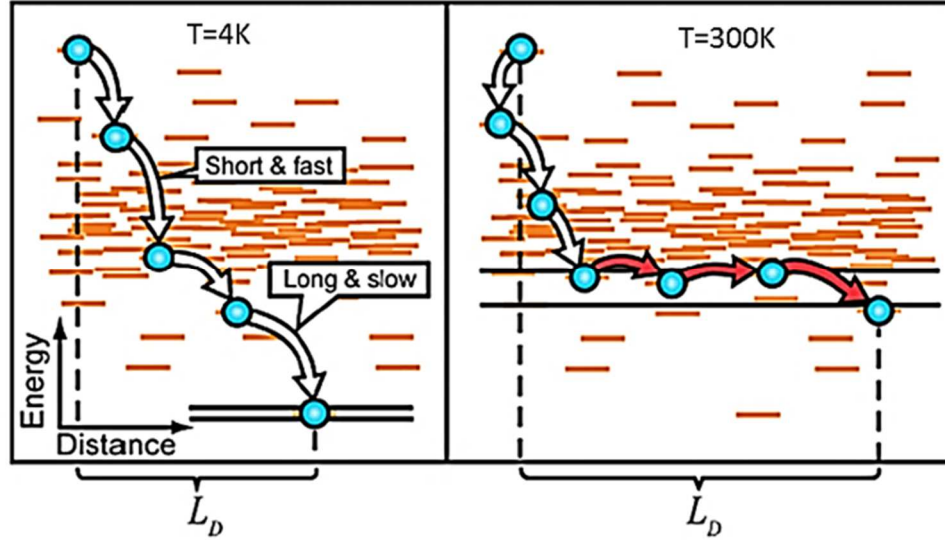


Figure 2.7: Schematic presentation of the Exciton diffusion process at low and room temperatures [16]

The key processes of exciton diffusion in a disordered medium are indicated in Figure 2.7 considering a Gaussian distribution of excitonic energies. After absorption of a light photon, an exciton is created in a conjugated segment with certain energy. For lower energy conjugated segments, the exciton is inclined to a downward migration via energy transfer toward the lower energy sites. The temperature activated hopping occurs between the similar energy sites with approximately same site-to-site distances. These downward migration and thermally activated hopping are available for both singlet and triplet excitons [19].

### 2.2.3 Exciton Dissociation

After generating an exciton with the help of a suitable donor and acceptor pair, electron and hole are still bounded with Coulomb force. Therefore, this polaron pair has to be separated to

have free charge carriers. The excitons dissociation is a two-step process at the donor and acceptor (D/A) interface. In generally, polymer phase of the polymer: fullerene systems, absorbs the majority of the photons and donor materials absorption is in the range of visible regime. Here, the exciton dissociation process is explained for an exciton which is initially generated in the donor phase [20].

The HOMO and LUMO energy levels of the donor and acceptor materials should be matched with each other for efficient exciton dissociation (Figure 2.8). A rapid dissociation can be obtained at the interfaces of the electronically matching materials which is much faster than any decay process. In both charge transfer processes, the electron and hole reside on the acceptor and donor materials, respectively [21]. However in this discussion, the charge carriers are considered as polarons or quasiparticles which consist of a charge and polarization of the surrounding.

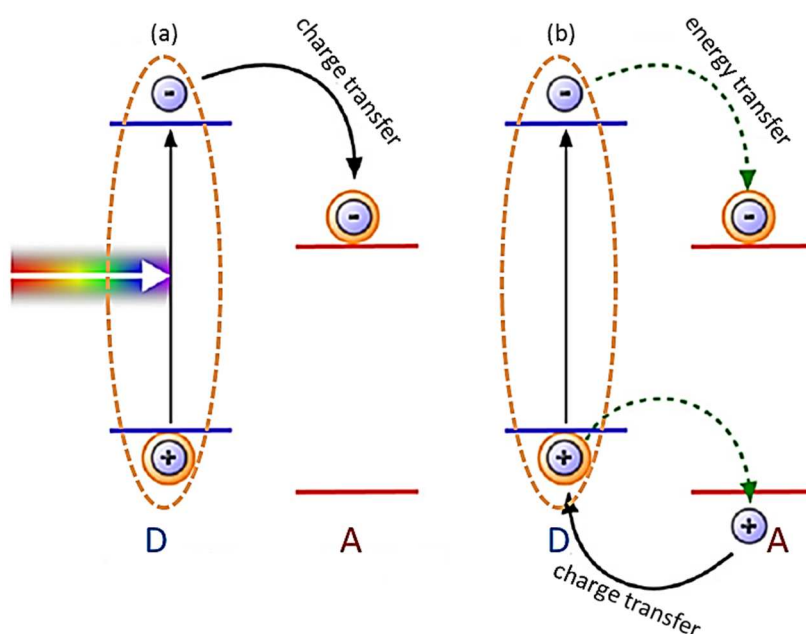


Figure 2.8: Charge transfer process in organic solar cells (a) direct electron transfer to acceptor (b) Forster energy transfer from donor to acceptor [20]

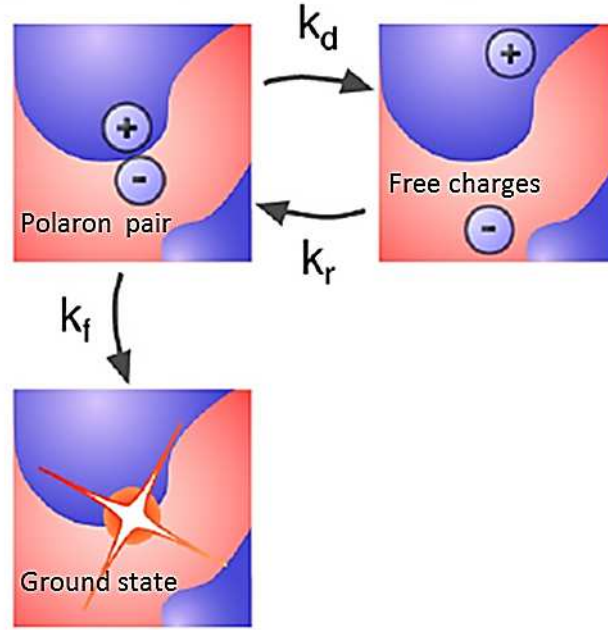


Figure 2.9: Illustration of a polaron pair at the donor-acceptor interface [20]

The Braun-Onsager model is used to describe the polaron pair dissociation. This model can be used to calculate the dissociating probability of a Coulomb-bounded opposite charge pair with a given initial distance in a given external electric field. The generated polaron pair can be recombined to the ground state or dissociated to free charges. The recombination rate is given by  $K_f = \tau_{pp}^{-1}$  which is inverse of its lifetime and the dissociation rate is given by  $K_d$  [22].

The electric field dependent polaron pair-separation is calculated by the Onsager-Braun model which gives the probability  $P(E, T)$  of electron-hole pair dissociation [22];

$$P(E, T) = \frac{K_d(E, T)}{K_d(E, T) + K_f} \quad (2.29)$$

with the field-dependent dissociation rate

$$K_d(E, T) = \frac{3\gamma}{4\pi r_{pp}^3} \exp\left(-\frac{E_b}{KT}\right) \frac{J_1(2\sqrt{-2b(E, T)})}{\sqrt{-2b(E, T)}} \quad (2.30)$$

$$= \frac{3\gamma}{4\pi r_{pp}^3} \exp\left(-\frac{E_b}{kT}\right) \left[1 + b + \frac{b^2}{3} + \dots\right]$$

Here  $\gamma = q\mu/\epsilon\epsilon_o$  represents the Langevin recombination factor [6] with charge  $q$ ,  $\mu$  is the sum of hole and electron mobilities and the effective dielectric constant of the organic semiconductor is denoted by  $\epsilon\epsilon_o$ . The  $r_{pp}$  is initial polaron-pair radius,  $E_b = e^2/4\pi\epsilon\epsilon_o r_{pp}$  is the Coulombic binding energy of the charge pair,  $kT$  is the thermal energy,  $J_1$  is the order one Bessel function and  $b$  is the reduced field with  $b = q^3 F / (8\pi\epsilon\epsilon_o (kT)^2)$ . Thus, the Onsager-Braun model gives the probability  $P(E, T)$  of electron-hole pair dissociation which can be expressed as;

$$P(E, T) = \frac{K_d(E, T)}{K_d(E, T) + (\mu\tau_f)^{-1}} \quad (2.31)$$

Here,  $K_d(F)$  is replaced with  $k_d(F) = \mu K_d(F)$ . The polaron pair dissociation probability  $P(E, T)$  strongly relies on the charge carrier mobilities  $\mu$  and the polaron-pair lifetime  $\tau_f$ . Therefore, the charge carrier generation efficiency is remarkably higher in the systems with high mobilities and long polaron-pair life times, at the acceptor-donor interface [22].

Considering the disorder in the blend, probability distribution of the excitons with different separation distances has been studied using numerical simulations. Hence, a distribution of separation distances can be written as:

$$P(r_{pp}, E, T) = \int_0^\infty P(Z, E, T) f(r_{pp}, Z) dZ \quad (2.32)$$

where  $f(r_{pp}, z)$  is a normalized distribution function given by:

$$f(r_{pp}, Z) = \frac{4}{r_{pp}^3 \sqrt{\pi}} Z^2 \exp\left[-\frac{Z^2}{r_{pp}^2}\right] \quad (2.33)$$

Where,  $p(z, E, T)$  is the dissociation probability at a given distance  $z$  in an organic solar cell.

### 2.2.4 Charge Carrier Transportation

After exciton dissociation and polaron pair separation, the free charge carriers, i.e. the polarons, should be transported towards the respective electrodes. Due to the high disordered behavior of organic semiconductors, the charge transportation generally occurs by hopping from one localized state to the next. This hopping occurs with weakly overlapped wave functions of neighboring sites. The Marcus hopping rate  $v_{ij}$  for a charge transport from site  $i$  to site  $j$  can be written as [23, 24],

$$v_{ij} = \frac{|J_{ij}|}{\hbar} \left( \frac{\pi}{\xi kT} \right)^{1/2} \exp \left( -\frac{(\Delta G_{ij} + \xi)^2}{4\xi kT} \right) \quad (2.34)$$

where  $\hbar$  is the reduced Planck constant,  $kT$  is the thermal energy and  $\xi$  is the reorganization energy.  $\Delta G_{ij}$  is the Gibbs free energy of two sites  $i$  and  $j$ .  $J_{ij}$  represents the transfer integral. This describes the overlap of the wave functions of the sites  $i$  and  $j$  which is proportional to the tunneling rate.

The Miller–Abrahams expression which is related to phonon-assisted tunneling mechanism can be expressed as [20, 25];

$$v_{ij} = v_o \exp(\gamma' r_{ij}) = \begin{cases} \exp \left( -\frac{\Delta E_{ij}}{kT} \right), & \Delta E_{ij} > 0 (\uparrow \text{hopping}) \\ 1, & \Delta E_{ij} \leq 0 (\downarrow \text{hopping}) \end{cases} \quad (2.35)$$

where  $\gamma'$  is the inverse localization radius based on the overlap integral of the wave functions assuming exponential decay with distance.  $v_o$  is the maximum hopping rate and  $r_{ij}$  is the distance between the  $i$  and  $j$  sites. The first exponential term describes the tunneling contribution of the system.  $\Delta E_{ij}$  is the energy difference between the sites  $i$  and  $j$  which is related to the thermal activation energy contribution for hops upwards. Next approach for the charge transfer rate is based on the polaronic effect, which relates to the coupling between the physical molecule configuration and its electronic energy. Therefore, it is assumed that the molecules involved in

the charge transfer have a different energy configuration for the charge being on one molecule or the other [26]. The resulting expression from this analysis can be shown as,

$$v_{ij} = \frac{J^2}{\hbar} \frac{\pi}{\sqrt{2E_b kT}} \exp\left(-\frac{E_b}{2kT}\right) \cdot \exp\left(-\frac{\Delta E_{ij}}{2kT} - \frac{\beta \Delta E_{ij}^2}{8kTE_b}\right) \quad (2.36)$$

where  $J$  is related to the overlap integral and  $E_b$  is the polaron binding energy.

Above mentioned methods explain the mesoscopic hopping mechanisms, rather than the macroscopic transport properties. However, the corresponding hopping rates can be applied in either Monte Carlo simulations or hopping master equations (ME) to simulate the macroscopic charge transport [26]. The basic approach of ME is the occupancy  $n_i$  of site  $i$  evolves in time according to the equation given by;

$$\frac{dn_i}{dt} = \sum_{j,j=i} (-n_i v_{ij} + n_j v_{ji}) \quad (2.37)$$

This assumption is correct for an ensemble of non-interacting particles if  $n_i$  represents the average occupancy of the site over a time scale much higher than the inverse of the characteristic hopping frequency.

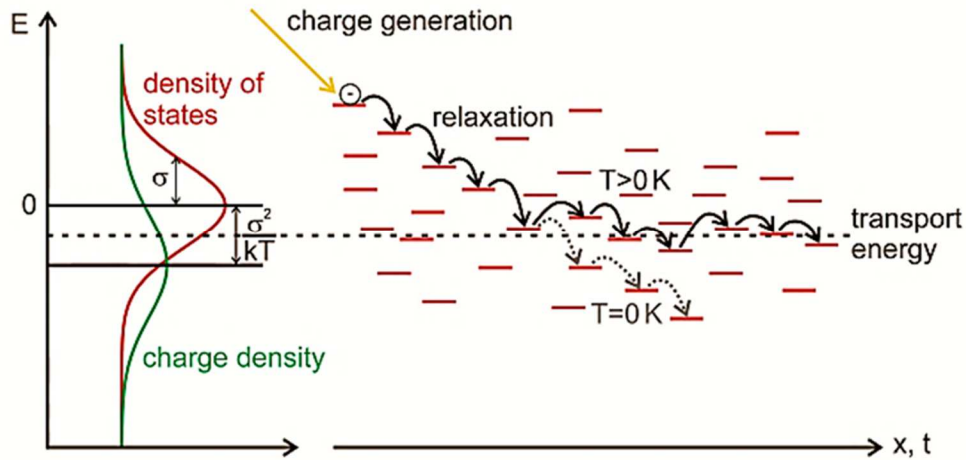


Figure 2.10: Schematic representation of charge transport concept [6, 20]

Bassler described the charge transport in a Gaussian density of states with Monte Carlo simulations, using the Miller–Abrahams hopping rate and the charge carrier mobility  $\mu_{GMD}$  which are dependent on the temperature  $T$  and field  $F$  [27];

$$\mu_{GMD} = \mu_{\infty} \exp \left\{ - \left( \frac{2\sigma}{3kT} \right)^2 + C \left( \left( \frac{\sigma}{kT} \right)^2 - \Sigma \right) F^{1/2} \right\} \quad (2.38)$$

Here,  $\sigma$  is called disorder parameter or energetic width of Gaussian density of states distribution.  $C$  and  $2/3$  are scaling factors. The  $\ln \mu \propto F^{1/2}$  and  $\ln \mu \propto 1/T^2$  are compatible with recent experiments.

For disordered organic materials, the average charge density can be written by  $-\sigma^2/kT$ . The  $\sigma$  represents the width of the Gaussian distribution. This is below the center of the density of states distribution for a given temperature. The charge transport mechanism involved in hopping processes around the transport energy can be shown in Figure 2.10. Charge carriers below the transport energy level are immobile and do not contribute to the charge transport. If the transport energy is increased due to the thermal activation energy, the number of available states for the mobile charge carriers is increased. The total carrier concentration is accounted as the sum of mobile, conductive charge carriers around the transport energy, and immobile charge carriers trapped in the tails of the Gaussian or exponential density of states. Therefore, the transport energy concept grants a method to describe the charge transporting mechanism in disordered organic semiconductors in equivalence to band transport plus trapping [20].

### 2.2.5 Charge Carrier Collection

After the transporting process, the charge carriers reach to the electrodes of the device. The electrodes should extract these carriers from the organic semiconductors and this process is

strongly affected by the device architecture. Furthermore, charge recombination strongly depends on the charge carrier concentration at the organic semiconductor-metal interface.

For qualitative analysis, recombination of free charge carriers and space-charge effects can be neglected. However, the charge carrier generation depends on the electric field. The internal field in the device is given by  $E = (V_0 - V)/L$ , where  $V$  is the applied voltage. Without recombination the photocurrent through the external circuit can be given as,

$$J_{P,max} = qGL \quad (2.39)$$

where  $q$  is the electric charge,  $G$  the generation rate of charge carriers, and  $L$  the thickness of the active layer.

According to the Equation 2.30, the  $J_{ph}$  is independent of  $V$ . Sokel and Hughes [28] pointed out that this result is incorrect due to neglected diffusion currents and voltage across the device. Using same approximation and including diffusion, Sokel and Hughes (SH) found an analytical solution for the photocurrent;

$$J_{Ph,SH} = J_{P,max} \left\{ \frac{\exp(qV/KT)+1}{\exp(qV/KT)-1} - \frac{2KT}{q} \right\} \quad (2.40)$$

Where,  $kT/q$  and  $V$  denote the thermal voltage and the internal voltage respectively.

The most important result is that the equation depends on the voltage across the device, although the exact shape can only be reconstructed by a convolution of models concerning polaron pair dissociation and charge extraction [28, 29]. Thus, the complete photocurrent can be written as;

$$J_P = qP(F)G_{pp}L \left\{ \frac{\exp(qV/KT)+1}{\exp(qV/KT)-1} - \frac{2KT}{q} \right\} \quad (2.41)$$

where  $P(F)$  is the polaron pair dissociation yield given by Onsager–Braun, equation and  $G_{pp}$  is the generation rate of polaron pairs. Here, the free charge generation rate  $G = P(F)G_{pp}$ .



### 2.3 Recombination Process

The annihilation of electron and hole, denoted as charge carrier recombination has a huge impact on the device performance of an organic solar cell. A successfully dissociated electron-hole pair can be recombined while transporting towards the respective electrodes. This process is called nongeminate recombination. If the created electron and hole pair decay to the ground state before they dissociate, this is denoted as geminate recombination. Geminate recombination is due to low mobility and conductivity in disordered semiconductors and short polaron-pair lifetimes [30]. The continuity equation describes the charge carrier dynamics and it can be written as [31];

$$\frac{dn}{dt} = -\frac{1}{q} \frac{dJ_n}{dx} + G - R \quad (2.42)$$

where  $n$  is the electron concentration,  $q$  the elementary charge and  $J_n$  the electron current. The optical generation rate  $G$  and the recombination rate  $R$ . The  $t$  and  $x$  are the time and the position. The generation current  $J_G$  and the loss current  $J_R$  can be obtained by integrating the equation 1.33 [31].

$$J_G = -q \int_0^d G(x) dx = qd\bar{G} \quad (2.43)$$

$$J_R = -q \int_0^d R(x) dx = qd\bar{R} \quad (2.44)$$

Where  $d$  is the thickness of the active layer. The  $\bar{G}$  and  $\bar{R}$  are spatially uniform generation and recombination rates. For low mobility free charges observed in organic semiconductors, a nongeminate recombination of the second order Langevin's theory is often employed. The recombination rate given by the Langevin theory as;

$$R = \gamma(np - n_i^2) \quad (2.45)$$

where charge carrier densities for electrons  $n$  and holes  $p$ ,  $n_i$  the intrinsic carrier concentration and the Langevin recombination prefactor  $\gamma$ . The Langevin recombination prefactor can be described by,

$$\gamma = \frac{q}{\epsilon_0 \epsilon_r} (\mu_e + \mu_h) \quad (2.46)$$

with the effective dielectric constant  $\epsilon_r \epsilon_0$  and the electron and hole mobilities  $\mu_e$  and  $\mu_h$  [31].

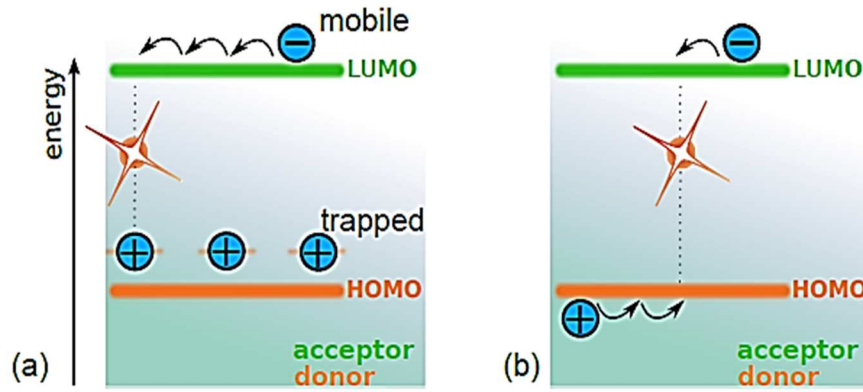


Figure 2.11: Nongeminate recombination: (a) mobile and a trapped polaron yielding a recombination rate  $\propto n$  (b) two mobile polarons yielding a recombination rate  $\propto n^2$  [31]

A mobile charge recombines with a trapped charge carrier is referred to as a first order process. If the trapped charge concentration is higher than the mobile charge density, the density of trapped charges is inexhaustible. If the trapped charge concentration is similar or lower than the mobile charge carrier concentration, the bimolecular decay is considered as second order process. For the organic bulk heterojunction solar cells, the Langevin model can be applied based on existing donor and acceptor phases where electrons and holes reside and can mainly recombine at the donor/acceptor interface. The Langevin recombination can be altered with the active layer morphology, the preparation conditions and the organic materials. Furthermore, a thermally activated recombination can reduce recombination rate, or lower the mobility of two

charges as shown in Equation 2.45. Other types of losses can occur due to structural defects or trapping charges in deep potential states which has low possibility to escape. These trapped charges will be recombined by mobile charge.

## 2.4 Solidification Process of Polymer

The organic semiconductors exhibit high exciton binding energy and the short exciton diffusion length due to their intrinsic electronic properties. Therefore, the arrangement of the single polymer chains is an important factor for the charge carrier mobility. The mobility of the charges in the crystalline regions is higher than the amorphous regions in the organic materials. However, the organic molecules form semicrystalline phases, but they do not form fully crystalline states. Formation of fully crystalline phases is interrupted by a high entropic activation barrier which is created with entanglement of the coiled polymer chains before crystallization. The amorphous region consists of entangled polymer chains, impurities and other defects. However, the crystallized region contains layered and laterally extended molecular structures. The size of the crystal does not depend on the molecular weight of the polymer, however it relies on the crystallization temperature. Therefore, crystalline lamellae of the polymer can be formed laterally up to micrometer range. The crystallization temperature ( $T_c$ ) of the polymers lies between the glass transition temperature  $T_g$  and the melting temperature  $T_m$ . Polymer crystallites are formed after super-cooling [32, 33].

Nuclei formation is the starting step of the polymer crystals in the amorphous melt. Nucleation can be defined as formation of a small amount of crystalline material due to fluctuations either in density or order in the supercooled melt. In the crystal growing process,

these particles (which are called embryos) convert to nuclei in the melt. If there is no second phase (existing nuclei) present and the nuclei formation occurs spontaneously due to supercooling the phenomenon is called homogenous nucleation [34]. But the heterogeneous nucleation occurs only after a second phase is formed (a foreign particle or surface from the same polymer nuclei/crystal). To form stable nuclei, the crystallization free energy barrier should be overcome. The size of the critical nucleus depends on this free energy barrier; i.e larger critical nuclei requiring longer times to form. The free energy of the nucleation can be given by [35];

$$\Delta G = \Delta G_c + \sum \gamma^* A \quad (2.47)$$

Where,  $\gamma^*$  is the specific surface free energy and  $\Delta G_c$  is the free energy of crystallization.

The large specific area to volume ratio decreases the free energy that can be obtained by crystallizing the small volume element of the nucleus. Generally, in a spherical nucleus with radius 'r', the free energy change can be expressed as [35]:

$$\Delta G = \frac{4}{3}\pi r^3 \Delta G_c + 4\pi r^2 \gamma^* \quad (2.48)$$

These two terms in the equation contribute to increase the free energy until a certain critical maximum is reached in free energy surface.

The nucleation rate is an exponential function of the temperature and it is inversely proportional to the volume of crystal domain  $V^{-1}$  as shown in Equations 2.49 and 2.50 respectively [36].

$$\frac{dN}{dt} = N_o \exp\left(-\frac{E_D + \Delta G^*}{RT}\right) \quad (2.49)$$

$$\tau_n \propto V^{-1} \quad (2.50)$$

where  $N_o$  is the number of molecules in a unit volume,  $E_D$  is the free energy of activation for diffusion across the phase boundary and  $\Delta G^*$  is the critical free energy barrier for primary

nucleation. This critical free energy barrier indicates free energy gain due to nuclei formation at high temperature. The behavior of the transport term  $E_D$  with the temperature is close to the viscosity. It remains constant at the high temperatures and rapidly increases at temperatures close to the glass transition. In undercoolings, the nucleation is dominated by the  $\Delta G^*$  term and it is  $\propto 1/\Delta T_c^2$ . Hence, the nucleation rate is zero at  $T_m$  and a large negative temperature coefficient is introduced by  $\exp(-\Delta G^*/RT)$ .

## 2.5 Photovoltaic Parameters

The power conversion efficiency (PCE) of a solar cell is defined as:  $PCE = (J_{sc} \cdot V_{oc} \cdot FF)/P_{in}$ , where  $J_{sc}$  is the short circuit current density,  $V_{oc}$  is the open circuit voltage, FF is the fill factor and  $P_{in}$  is the incident input power. To allow for valid comparison of device performance, an international standard for input power is used. This standard is an incident spectrum of AM 1.5 G, with an intensity of  $1000\text{W/m}^2$  ( $100\text{ mW/cm}^2$ ), whilst the cell is at a temperature of  $25^\circ\text{C}$ .

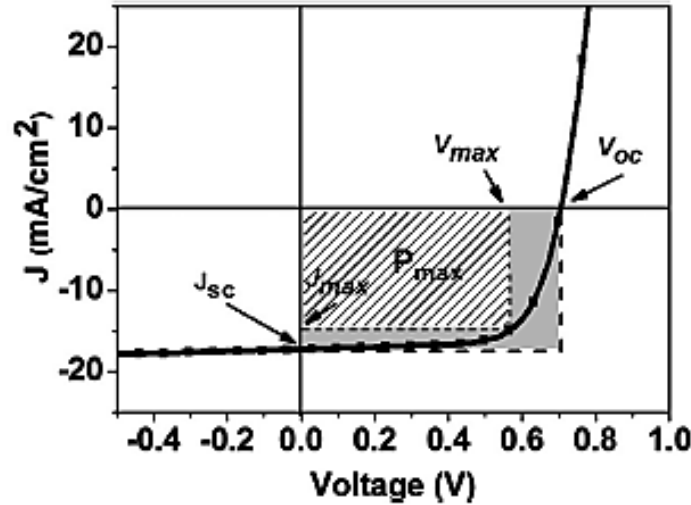


Figure 2.12: Current density–voltage (J–V) characteristics for a generic illuminated solar cell [39]

Therefore, there are three major device characteristics which completely determine the efficiency of the device. Figure 2.12 shows a typical illuminated J–V characteristic curve which illustrates these three characteristics. The above efficiency factors influence the device characteristics of organic–inorganic hybrid solar cells [37].

The short circuit current density ( $J_{sc}$ ) is the maximum photo-current density which can be extracted from the device at short circuit conditions. The  $J_{sc}$  is directly related to the external quantum efficiency (EQE). This relationship can be expressed as [38],

$$J_{sc} = \frac{q}{hc} \int_{\lambda_{min}}^{\lambda_{max}} EQE P_{in}(\lambda) \lambda d\lambda \quad (2.51)$$

where  $q$  is the value of the charge,  $P_{in}$  is the input power,  $h$  is the reduced Planck constant,  $C$  and  $\lambda$  are the velocity and the wavelength of the light respectively.

The EQE is defined as the ratio of the number of charge carriers collected by the solar cell to the number of photons shining on the solar cell from outside sources. It is calculated from the ratio of extracted electrons to incident photons measured at short circuit conditions. The EQE is especially interesting for solar cells with active layers consisting of blends of materials with complementary absorption spectra. In this case it can give insight into the contribution of charge generation of each of the components. In a hybrid solar cell operation, EQE is determined by five factors; each factor has a quantity of an associated efficiency [38]. Also, this relationship can be expressed as,

$$EQE = \eta_A \cdot \eta_{diff} \cdot \eta_{diss} \cdot \eta_{tr} \cdot \eta_{cc} \quad (2.52)$$

Here,  $\eta_A$ ,  $\eta_{diff}$ ,  $\eta_{diss}$ ,  $\eta_{tr}$  and  $\eta_{cc}$  represent the light absorption efficiency, the exciton diffusion efficiency, the exciton dissociation efficiency, the charge transport efficiency, and the electrons–holes collection efficiency, respectively. The parameters  $\eta_A$ ,  $\eta_{diff}$ ,  $\eta_{diss}$ ,  $\eta_{tr}$  and  $\eta_{cc}$  describe the

efficiency yields of the device, which represent the most effective way of increasing the  $J_{sc}$  of a hybrid device.

The fill factor describes the ‘squareness’ of the  $J$ – $V$  curve. It is defined as:  $FF = J_m V_m / J_{sc} V_{oc}$ . The  $J_m$  and  $V_m$  are defined as the maximum power point current density and voltage, respectively. Due to physical constraints on diode quality, the practical limit to fill factor is less than the ideal value of 1 ( $FF < 1$ ). The behavior of a real diode will deviate from the ideal, primarily as a result of recombination occurring at the junction. For OPV and organic–inorganic hybrid solar cells, the ‘junction’ is the D–A interface, which is distributed throughout the entire photoactive layer. Deviations from the ideal case, and thus the shape of the  $J$ – $V$  curve, can be quantitatively characterized by the parasitic loss mechanisms of series and shunt resistance. Zero series resistance ( $R_s = 0$ ) is ideal, however, poor conductivity through the active layer and reduced charge carrier injection to the electrodes represents increased series resistance. Conversely, the ideal diode case demands infinite shunt resistance ( $R_{sh} = \infty$ ). Reduction in  $R_{sh}$  is caused by imperfections within the photoactive film or current leaks at the interface between layers in the device [39].

The origin of open circuit voltage in bulk heterojunction devices is still not well understood. However, the open-circuit voltage ( $V_{oc}$ ) of a solar cell under light is defined as a voltage at which the net current in the cell is equal to zero. In a well behaving device, the current measured in the dark and under illumination conditions coincide for applied voltages exceeding the  $V_{oc}$ . This implies that, approximately, the  $V_{oc}$  corresponds to the net internal electric field of the device, which gives the flat band condition [39].

A great deal of research has been done on tuning the polymer solar cells with inorganic nanoparticles (INPs). The inorganic NPs of various sizes and configurations have been integrated

into organic solar cell architecture in order to fine tune and enhance the morphology, electronic and optical absorption of respective devices. As a result, significant enhancements in the power conversion were obtained. Depending on the position in the solar cell architecture, incorporation of NPs can be categorized into three main groups which are: (i) photoactive or hole transport layers, (ii) buffer layers, and (iii) between different interfaces. Table 1 summarizes the state of the reported electrical parameters of the polymer solar cells indicating the respective efficiency improvements.

Table 2.1: The state of the reported electrical parameters of polymer solar cells

NPs	Size (nm)	$J_{sc}(A/cm^2)$	$V_{oc}(V)$	FF	PCE (%)	Mechanism	Ref.
ZnO	<100	11.91	0.579	49	3.39	Low resistivity	[40]
ZnO	<15	12.2	0.55	52	3.5	High electron mobility	[41]
ZnO	<35	9.31	0.67	61	3.84	High electron accepting	[42]
ZnO	50	10.41	0.58	53	3.2	Morphology	[43]
ZnO	3–4	6.3	0.64	54	2.2	High electron mobility	[44]
Au	18	8.94	0.63	62	3.51	LSPR, hole collection	[45]
Au	30-40	10.18	0.59	69	4.19	LSPR	[46]
Au	1.5-20	9.77	0.6	63	3.71	LSPR, morphology	[47]
Au	5~10	9.71	0.48	62	3.36	Recombination	[48]
Ag	20	7.03	0.61	48	2.06	LSPR, morphology	[49]
Ag	60	8.07	0.58	58	2.75	LSPR	[50]
Ag	110	9.28	0.65	59	3.56	LSPR, scattering	[51]
TiO <sub>2</sub>	60	10.29	0.6	60	3.69	Morphology	[52]
TiO <sub>2</sub>	20-40	2.75	0.44	35	0.42	Morphology	[53]
Ag-TiO <sub>2</sub>	<100	9.5	0.64	65	3.96	LSPR, morphology	[54]



## References

- [1] Simone D. Z., 2009. Innovative solutions in organic photovoltaic devices, PhD Thesis.
- [2] Tress W., 2011. Device Physics of Organic Solar Cells, PhD Thesis.
- [3] Proctor, C. M., Kuika, M., Nguyena, T.Q., 2013. Charge carrier recombination in organic solar cells. *Progress in Polymer Science* 38:1941–1960.
- [4] Strobl, G. 2007. The Physics of Polymers. *Springer-Verlag Berlin Heidelberg*, 3rd edition.
- [5] Deibel, C., Mack, D., Gorenflot, J., Scholl, A., Krause, S., Reinert, F. Rauh, D., and Dyakonov, V., 2010. Energy levels and exciton binding energy in the conjugated polymer poly(3-hexyl thiophene). *Phys. Rev. B*, 8(085202):1-4.
- [6] Matthias A. R., 2012. *Morphology of polymer-based films for organic photovoltaics*, PhD Thesis.
- [7] Spano, F. C., 2010. The Spectral Signatures of Frenkel Polarons in H- and J-Aggregates, *Accounts of chemical research*. 43: 429-439.
- [8] Cornil, J., Beljonne, D., Shuai, Z., Hagler, T. W., Campbell, I., Bradley, D. D. C., Bredas, J. L., Spangler, C.W., and Mullen, K., 1995. Vibronic structure in the optical absorption spectra of phenylene vinylene oligomers: a joint experimental and theoretical study. *Chem. Phys. Lett.*, 247:425–432.
- [9] Luer, L., Egelhaaf, H.-J., Oelkrug, D., Cerullo, G., Lanzani, G., Huisman, B.-H., and de Leeuw, D., 2004. Oxygen-induced quenching of photoexcited states in polythiophene films. *Org. Electron.*, 5:83-88.
- [10] Frank C. S., and Carlos S., 2014. H- and J-Aggregate Behavior in Polymeric Semiconductors, *Annu. Rev. Phys. Chem.* 65:477–500.
- [11] Clark, J., Silva, C., Friend, R. H., and Spano, F. C., 2007. Role of intermolecular coupling in the photophysics of disordered organic semiconductors: Aggregate emission in regioregular polythiophene. *Phys. Rev. Lett.*, 98:206406.
- [12] Yasunari T., Hideo O., Hiroaki B., and Shinzaburo I., 2015. Exciton Diffusion in Conjugated Polymers: From Fundamental Understanding to Improvement in Photovoltaic Conversion Efficiency. *J. Phys. Chem. Lett.* 6: 3417–3428.
- [13] Ohkita, H., Ito, S., 2011. Transient Absorption Spectroscopy of Polymer-Based Thin-Film Solar Cells. *Polymer*. 52: 4397–4417.
- [14] Beenken, W. J. D., 2009. Excitons in conjugated polymers: Do we need a paradigm change? *Phys. Status Solidi A*. 206:2750–2756.

- [15] Pope, M. and Swenberg, C. E., 1999. Electronic processes in organic crystals and polymers. *Oxford University Press*, 2nd edition.
- [16] Oleksandr V. M., Paul W. M. B., and Nguyen T.Q., 2015. Exciton diffusion in organic semiconductors. *Energy Environ. Sci.*, 8: 1867-1888.
- [17] Kurrle, D., and Pflaum, J., 2008. Exciton diffusion length in the organic semiconductor diindenoperylene. *Appl. Phys. Lett.*, 92:133306.
- [18] Athanasopoulos, S., Emelianova, E. V., Walker, A. B., and Beljonne, D., 2009. *Phys. Rev. B.* 80: 195209.
- [19] Stavros A., Evguenia V. E., Alison B. W., and David B., 2009. Exciton diffusion in energetically disordered organic materials. *Physical Review B.* 80: 195209.
- [20] Carsten D., and Vladimir D., 2010. Polymer–fullerene bulk heterojunction solar cells. *Rep. Prog. Phys.* 73:096401.
- [21] Hwang, I.-W., Moses, D., and Heeger A. J., 2008. Photoinduced carrier generation in P3HT/PCBM bulk heterojunction materials. *J. Phys. Chem. C.* 112:4350–4354.
- [22] Mihailetschi, V. D., Koster, L. J. A., Hummelen, J. C., and Blom, P.W.M., 2004 Photocurrent generation in polymer–fullerene bulk heterojunctions. *Phys. Rev. Lett.* 93: 216601.
- [23] Marcus, R. A., 1956. On the theory of oxidation-reduction reactions involving electron transfer. *I. J. Chem. Phys.* 24: 966.
- [24] Kurrle, D., and Pflaum, J., 2008. Exciton diffusion length in the organic semiconductor diindenoperylene. *Appl. Phys. Lett.*, 92:133306.
- [25] Miller, A. and Abrahams, E., 1960. Impurity conduction at low concentrations. *Phys. Rev.* 120: 745.
- [26] Nir, T., Yevgeni P., Noam. and Yohai., 2009. Charge Transport in Disordered Organic Materials and Its Relevance to Thin-Film Devices: A Tutorial Review. *Adv. Mater.* 21: 2741–2761.
- [27] Bassler H., 1993. Charge transport in disordered organic photoconductors - a Monte Carlo simulation study. *Phys. Status Solidi b.* 175:15.
- [28] Sokel. R., and Hughes R. C., 1982. Numerical analysis of transient photoconductivity in insulators. *J. Appl. Phys.* 53: 7414.
- [29] Limpinsel, M., Wagenpfahl, A., Mingeback, M., and Deibel, C., 2010. Photocurrent in bulk heterojunction solar cells. *Phys. Rev. B.* 81: 085203.

- [30] Limpinsel, M., Wagenpfahl, A., Mingebach, M., Deibel, C., and Dyakonov, V., 2010 Investigation of the photocurrent in bulk heterojunction solar cells. *Phys. Rev. B.* 81: 085203.
- [31] Alexander F., 2013. Recombination Dynamics in Organic Solar Cells, PhD Thesis.
- [32] Hoffman, J. D., Davis, G. T., and Lauritzen, J. I., 1976. Treatise on Solid State Chemistry, 1976: 3.
- [33] Lotz B., 2000. What can polymer crystal structure tell about polymer crystallization processes? *Eur. Phys. J. E*, 3:185.
- [34] Massa, M. V., and Dalnoki, V. K., 2004. Homogeneous crystallization of poly(ethylene oxide) confined to droplets: The dependence of the crystal nucleation rate on length scale and temperature. *Phys. Rev. Lett.*, 92:255509.
- [35] Wunderlich, B., Macromolecular Physics, 1976. Crystal Nucleation, Growth, Annealing, Academic Press, New York, 1976:2.
- [36] Krebs, F.C., Thomann, Y., Thomann, R., and Andreasen, J.W., 2008. A simple nanostructured polymer/ZnO hybrid solar cell-preparation and operation in air. *Nanotechnology*. 19: 424013.
- [37] Moliton, A., and Nunzi, J. M., 2006, How to Model the Behavior of Organic Photovoltaic Cells. *Polym. Int.* 55(6): 583–600.
- [38] Wright, M., and Uddin, A., 2012, Organic–Inorganic Hybrid Solar Cells: A Comparative Review. *Sol. Energy Mater. Sol. Cells*. 107: 87–111.
- [39] Luyao, L., Tianyue, Z., Qinghe, W., Alexander M., Donglin Z., and Luping Y., 2015. Recent Advances in Bulk Heterojunction Polymer Solar Cells. *Chem. Rev.* 115: 12666–12731.
- [40] Oh, S.H., Heo, S.J., Yang, J.S., Kim, H.J., 2013. Effects of ZnO nanoparticles on P3HT:PCBM organic solar cells with DMF-modulated PEDOT:PSS buffer layers. *ACS Appl. Mater. Interfaces*. 5: 11530.
- [41] Zhu, F., Chen, X., Lu, Z., 2014. Efficiency Enhancement of Inverted Polymer Solar Cells Using Ionic Liquid-functionalized Carbon Nanoparticles-modified ZnO as Electron Selective Layer. *Nano-Micro Lett.* 6(1): 24-29.
- [42] Gao, H. L., Xing W.Z., Jun H.M., Zhi G. Y., Liu Q. Z., Jin L. W. and Xin L., 2015. Enhanced efficiency in polymer solar cells via hydrogen plasma treatment of ZnO electron transport layers *J. Mater. Chem. A*. 3: 3719–3725.
- [43] Sekine, N., Chou, C. H., Wei, L. K., Yang Y., 2009. ZnO nano-ridge structure and its application in inverted polymer solar cell, *Organic Electronics* 10:1473–1477.

- [44] Qian, L., Jihua Y., Renjia Z., Aiwei T., Ying Z., Tseng, T. K., Debasis B., Jiangeng X. and Paul. H. H., 2011. Hybrid polymer- CdSe solar cells with a ZnO nanoparticle buffer layer for improved efficiency and lifetime. *J. Mater. Chem.* 21: 3814-3817.
- [45] Fung D.D.S., Qiao L.F., Choy W.C.H. 2011. Optical and electrical properties of efficiency enhanced polymer solar cells with Au nanoparticles in a PEDOT–PSS layer. *J. Mater. Chem.* 21: 16349–16356.
- [46] Chen F. C., Wu J.L., Lee C.L. 2009. Plasmonic-enhanced polymer photovoltaic devices incorporating solution- processable metal nanoparticles. *Appl. Phys. Lett.* 95: 013305.
- [47] Spyropoulos, G.D., Stylianakis M.M., Emmanuel, E., and Kymakis, E., 2012. Organic bulk heterojunction photovoltaic devices with surfactant-free Au nanoparticles embedded in the active layer. *Appl. Phys. Lett.* 100: 213904.
- [48] Liu, R., 2014. Hybrid Organic/Inorganic Nanocomposites for Photovoltaic Cells. *Materials.* 7(4): 2747-2771.
- [49] Paci,B., Spyropoulos, G.D., Amanda G., Daniele B., Valerio, R. A., Emmanuel S., Emmanuel, K.,2011. Enhanced Structural Stability and Performance Durability of Bulk Heterojunction Photovoltaic Devices Incorporating Metallic Nanoparticles. *Adv. Funct. Mater.* 21: 3573–3582
- [50] Yang, J., You, J., Chen, C.C., Hsu, W.C., Tan, H.R., Zhang, X.W., Hong, Z., Yang, Y., 2011. Plasmonic polymer tandem solar cell. *ACS Nano.* 5(8):6210-7.
- [51] Kim C. H., 2011.Silver nanowire embedded in P3HT:PCBM for high-efficiency hybrid photovoltaic device applications. *ACS Nano* 5: 3319–3325.
- [52] Hu, X., Jian. X., Yanhong T., Conghua. Z., and Junliang, Y.,2015 Phys. Interface modification of polymer solar cells using graphene oxide and TiO<sub>2</sub> NPs. *Status Solidi A.* 212(3): 585–590.
- [53] Kwong, C. Y., Choy, W. C. H., Djurisi, A. B., Cheng, K. W., and Chan, W. K.,2004. Poly(3-hexylthiophene):TiO<sub>2</sub> nanocomposites for solar cell applications. *Nanotechnology.* 15:1156–1161.
- [54] Liu,K., Yu, B., Qu,S., Tan, F., Chi,D., Lu, S., Li, Y., Kou, Y., and Wang, Z., 2014. Efficient hybrid plasmonic polymer solar cells with Ag nanoparticle decorated TiO<sub>2</sub> nanorods embedded in the active layer, *Nanoscale.* 6: 6180.

## CHAPTER 3

### Experimental Methods

#### 3.1 Materials

The chemical structures for the donor polymers and fullerene acceptors used throughout the study are shown in Figure 3.1. Regioregular P3HT Rieke “E” was purchased from Rieke Metals, Inc., and PC70BM was purchased from SES Research Inc., USA. They are used as-received. Poly(3,4-ethylenedioxythiophene)-poly(styrenesulfonate) (PEDOT:PSS) 1.3 wt.% dispersion in H<sub>2</sub>O, conductive grade was purchased from Sigma-Aldrich, USA and diluted by adding equal volume of H<sub>2</sub>O. Indium tin oxide (ITO) coated glass slides measuring 25x75x1.1mm (10  $\Omega$ /sq., and ITO thickness 20–100 nm) were purchased from nanocs.com, USA. CuO NPs in the size range of 60–100nm, ZnO NPs (12nm) and Au NPs (15nm) were purchased from nanocs.com, USA. Ultra-high purity, oxygen free nitrogen gas was purchased from Airgas, USA. Aluminum wire of 0.15mm diameter was purchased from Ted Pella, Inc. USA.

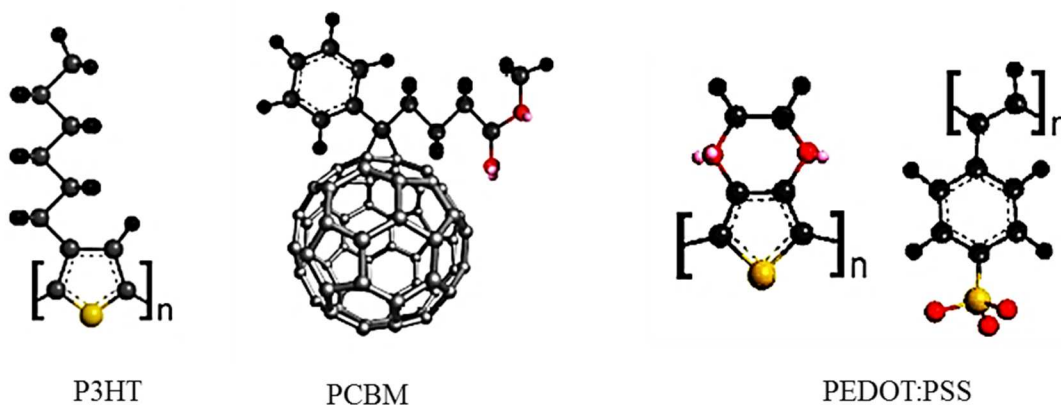


Figure 3.1: Chemical structures of conjugated polymers

### **3.1.1 P3HT (poly 3-hexylthiophene)**

An inherent conducting polymer, P3HT is an important material due to its solubility in various solvents and its high electrical conductivity. This electrical conductivity occurs when electrons are added or removed from the conjugated  $\pi$ -orbitals via doping [1, 2]. The P3HT molecules can be coupled as head-to-head (HH) or head-to-tail (HT) manner and HT-regioregularity improves electroconductivity, optical nonlinearity, and magnetic properties. Furthermore, P3HT shows photoluminescence properties based on the tunability during synthesis [3]. Crystallization mechanism of conjugated polymers; such as P3HT is more complex because of the rigidity of the polymer backbone and the presence of side chains. A precise crystallization mechanism for conjugated polymers has not yet been fully understood [4]. Generally, P3HT serves as a donor material in the polymer solar cells.

### **3.1.2 PCBM ([6, 6]-phenyl-C71-butyric acid methyl ester)**

PCBM is widely used as the soluble electron acceptor to fabricate efficient organic polymer solar cells. Previous studies [5] have shown that PCBM fullerene derivative provides better electronics properties in the polymer solar cells due to the exciton dissociation in P3HT/PCBM systems. However, it has very low absorption coefficients in UV-Vis region, thus limiting its light harvesting efficiency [6]. PCBM is considered as a disordered material with a reported mobility in the  $0.05\text{-}0.2\text{ cm}^2\text{ V}^{-1}\text{ s}^{-1}$  range [7].

### **3.1.3 PEDOT: PSS (Poly (3, 4-ethylenedioxythiophene)-poly (styrenesulfonate))**

The conducting polymer, PEDOT, is a promising candidate for electrodes in electronics devices. PEDOT is optically transparent and highly stable in thin oxidized films, which can be

chemically polymerized in a poly-styrenesulfonic acid (PSS) solution to give a PEDOT:PSS water emulsion. PEDOT is a positively doped conjugated polymer and the counter-ions of sulfonate anionic groups of PSS are used to balance the doping charges [8, 9]. Many studies have been instigated to increase the conductivity of PEDOT:PSS by introducing doping materials; however, the origin of the conductivity increment by those secondary dopants is still unclear.

### 3.1.4 Copper oxide, Zinc Oxide and Gold nanoparticles

Copper oxide, Zinc oxide, and gold are attractive candidates for solar cells fabrication due to their unique electronics, optical, and morphological properties. These properties will be discussed in the future chapters with more details. Considering the above mentioned properties, nanoparticles of these materials are used to improve the optoelectronic and morphological properties in the polymer semiconductors. In this study, commercially available CuO, ZnO and Au nanoparticles with a purity of 99.95+% (higher than 99.95%) were used. The levels of impurities are shown in Tables 3.1 (a), 3.1 (b) and 3.1 (c); respectively.

Table 3.1: Impurity level in the nanoparticle samples in ppm: (a) CuO NPs, (b) ZnO NPs, and (c) Au NPs

(a)

Mn	Pb	Fe	Mg	P	K	Ba	Ca	Sr	Zn	Co	Cd
0.0031	0.001	0.0083	0.0071	0.001	0.001	0.0076	0.004	0.0027	0.001	0.004	0.0021

(b)

Cu	Fe	Cd	Mn	K	Pb	Al
2	0.05	5.3	3.8	0.03	6.8	0.08

(c)

Ag	As	Cd	Cu	Fe	Pb	Sb
<0.0015	<0.001	<0.003	<0.0085	<0.001	<0.005	<0.001

### 3.2 Device Fabrication

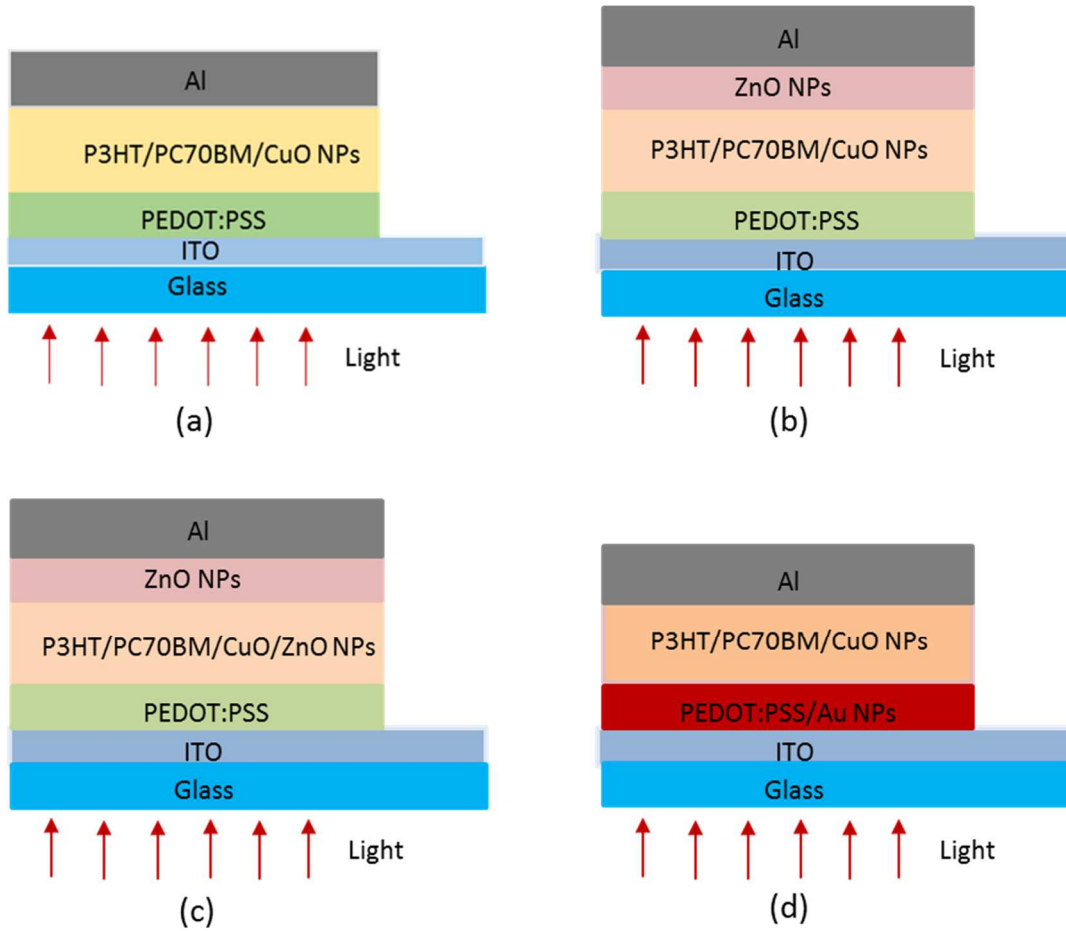


Figure 3.2: Schematic illustration of the structure of polymer solar cells

#### 3.2.1 CuO NPs incorporated P3HT/PC70BM solar cells

PSCs containing CuO NPs were fabricated inside a glove box in an inert atmosphere using nitrogen gas. The P3HT/PCBM/CuO NPs hybrid solution was prepared in a two-step process. The first step was to obtain the P3HT/ PC70BM blend by dissolving 10 mg of regioregular P3HT and 10 mg of PC70BM in 2ml chlorobenzene. The mixture was stirred at 50 °C for 12 hours. The second step is the incorporation of CuO NPs into the blend by dispersing CuO NPs in 2ml of chlorobenzene and adding it to the P3HT/PCBM blend in weights leading to



the final weight ratios (P3HT/PCBM/CuO-NPs) of 10:10:0.2, 10:10:0.4, 10:10:0.6, 10:10:0.8, and 10:10:1 mg, respectively.

A schematic illustration of the structure of the photovoltaic devices which are fabricated for this study is shown in Figure 3.2 (a). The devices were fabricated in a glove box in nitrogen atmosphere by depositing layers of the materials on a 1mm glass substrate. The transparent electrode ITO (Merck) was ultrasonically cleaned using a series of solvents like ammonia/hydrogen peroxide/ deionized water mixture, methanol, and isopropyl alcohol. The PEDOT/PSS layer with a thickness of 40 nm was spin coated at 4000 rpm on the substrate and then baked at 120 °C for 15 min. This serves as a thin hole-transport layer. Once the sample cooled to room temperature, the hybrid solution containing P3HT/ PC70BM/CuO NPs was deposited by spin-coating at 800 rpm for 1 min, which leads to a film thickness of about 100–150 nm. The purpose of this layer is to serve as the active layer. The upper cathode layer with a thickness of approximately 100 nm was formed by thermally evaporating aluminum under high vacuum. The final device had an area of 0.15 cm<sup>2</sup>.

To study the annealing effect on the CuO NPs incorporated P3HT/PC70BM thin film, all the devices were annealed at 150° C for 30 minutes inside a vacuum furnace immediately after Al electrode deposition.

### **3.2.2 CuO and ZnO NPs incorporated P3HT/PC70BM solar cells**

In order to fabricate and characterize the devices, similar materials and procedures, explained in section 3.2.1 will be used. Additionally, Different amounts of ZnO nanoparticles (12 nm diameter) were dispersed in pure ethanol leading to four solutions with concentrations of 10, 20, 30, and 40 mg ml<sup>-1</sup> of NPs.

Fabrication of the P3HT/PCBM/CuO/ZnO NPs hybrid device is a two-step process. In the first step, a thin film of ZnO NPs was assembled as a buffer layer on the CuO NPs incorporated P3HT/PC70BM active layer as shown in Figure 3.2(b). A 40 nm-thick PEDOT/PSS layer, which serves as a thin hole-transport layer, was spun coated at a rotational velocity of 4000 rpm, followed by heating at 120°C for 20 minutes in air. When the temperature of the samples reached the ambient temperature, the blends with P3HT:PC70BM: CuO NPs and ZnO solution were spun coated for two minutes at 1000 rpm and 2000 rpm; respectively. In this study, five different devices (reference cell, 10, 20, 30 and 40 mg ml<sup>-1</sup> ZnO NPs in the buffer layer) were fabricated. These samples are denoted as A, B, C, D and E; respectively. The active layers measured 120 nm in average thickness and 0.12 cm<sup>2</sup> in surface area. The ZnO film thickness obtained was approximately 60 nm. Annealing was performed on all devices, after Al electrode deposition, inside an inert oven at 150°C, 200°C and 250°C for 30 minutes. After fabricating the device, to investigate the electrical properties current density- voltage (J–V) characteristics and EQE measurements will be obtained.

In the second step, the ZnO NPs along with CuO NPs were incorporated in the P3HT/PC70BM active layer while remaining ZnO NPs buffer layer in the device as shown in figure 3.2 (c). By this experiment, it is expected to understand the effect of ZnO NPs on PCE as electron acceptors in the CuO NPs incorporated P3HT/PC70BM active layer. Similar to the first step, the effect of CuO and ZnO NPs in the active layer will be studied by current voltage (J–V) characteristics, EQE measurements, UV–visible analysis and EDX mapping. The surface roughness measurements of the CuO and ZnO NPs incorporated active layer will be obtained by Atomic Force Microscope (AFM).

### 3.2.3 Au/PEDOT: PSS-P3HT/PCBM/CuO solar cells

In this experiment, Au Nanoparticles (18 nm diameter) will be purchased from online (nanocs.com). Different amounts of Au NPs will be added to 10 ml of PEDOT: PSS aqueous solution, leading to six PEDOT: PSS solutions with 0, 0.02, 0.06, 0.10, 0.14, and 0.18 mg of NPs; respectively. The device fabrication procedure and other materials will be the same as in section 3.2.2. The schematic illustration of the expected device is shown in Figure 3.5.

### 3.3 Characterization

The electrical properties of devices in each composition were characterized under ambient conditions without any encapsulation. The samples were placed under a UV solar simulator lamp (xenon lamp, Oriel Instruments) that was equipped with AM 1.5G filter. The output intensity of the lamp was adjusted to  $100 \text{ mW/cm}^2$  using a silicon photodiode (LI-200 pyranometer). The current density–voltage (J–V) measurements were carried out using a source meter (Keithley 2400). The PV parameters, open circuit voltage ( $V_{oc}$ ), short circuit current ( $J_{sc}$ ), fill factor (FF), EQE, and PCE, were measured in devices with and without CuO NPs that were made under the same conditions.

The EQE was measured by placing a quantum efficiency measurement kit (New port, serial number 425) inside the solar simulator. A 300W Xenon arc lamp was used as a light source with a Merlin monochromator to provide throughput to the cells under test. The software supplied with the kit generates an EQE spectrum against a broad wavelength, the peak value of the spectrum is considered in the discussion. The optical properties of the cells with and without CuO NPs were determined using a UV–Vis spectrophotometer (PerkinElmer LAMBDA 650

spectrophotometer). The surface structures of the CuO NPs layers were analyzed using a scanning electron microscope (FEG-SEM Hitachi S-4800).

The crystallinity of the films was studied by XRD (Cu K-source) under 40 kV and 40mA tube current. The X-ray profile was recorded from 4deg to 7deg with a rate of 0.2 deg/min. DSC measurements were collected using TA instruments Q2000 with heating rate of 5 °C/min and a sample weight of 5–10 mg. Surface topographical analysis was conducted using Agilent 5420 Atomic Force Microscope (AFM), and surface roughness was measured using “Pico Image Basics” and GWYDDION softwares in ACAFM noncontact mode with an I-gain of 8, set point of 1.84, and a scan size of 2x2  $\mu\text{m}$ .

## References

- [1] Roncali, J., 1992. Conjugated poly (thiophenes): synthesis, functionalization, and applications. *Chem. Rev.*, 92 (4): 711–738.
- [2] Viney, S., Zhongrui, L., Shawn, B., Enkeleda, D., Yang, X., Xiaodong, M., Vasyl, P. K., Gregory, J. S., Tito, V., Alexandru, R. B., Divey, S., and Alexandru, S. B., 2009. Electrical, Optical, and Morphological Properties of P3HT-MWNT Nanocomposites Prepared by in Situ Polymerization. *J. Phys. Chem. C*. 113: 8023–8029.
- [3] Gan, Q., Bartoli, F. J., and Kafafi, Z. H., 2013 Plasmonic-Enhanced Organic Photovoltaics: Breaking the 10% Efficiency Barrier. *Adv. Mater.* 25: 2385–2396.
- [4] Kim, T., and Sabine, L., 2014. Morphology of P3HT in Thin Films in Relation to Optical and Electrical Properties, *Adv Polym Sci.* 265: 39–82.
- [5] Brown, M. D., Suteewong, T., Kumar, R. S. S., 2011. Plasmonic dye-sensitized solar cells using core-shell metal-insulator nanoparticles. *Nano Letters*. 11: 438–445.
- [6] Zhang, C.R., Han, L.H., Zhe, J.W., Jin, N.Z., 2013. Electronic Structures and Optical Properties of Phenyl C71 Butyric Acid Methyl Esters, 2013. *Journal of Nanomaterials*. 2013: 612153-612161.
- [7] Cheung, D. L., and Troisi, A., 2010. Theoretical Study of the Organic Photovoltaic Electron Acceptor PCBM: Morphology, Electronic Structure, and Charge Localization. *J. Phys. Chem. C*. 114: 20479–20488.
- [8] Krebs, F.C., Thomann, Y., Thomann, R., and Andreasen, J.W., 2008. A simple nanostructured polymer/ZnO hybrid solar cell-preparation and operation in air. *Nanotechnology*. 19: 424013.
- [9] Kim, K., and Carroll D. L., 2005. Roles of Au and Ag nanoparticles in efficiency enhancement of poly (3-octylthiophene)/C60 bulk heterojunction photovoltaic devices. *Appl. Phys. Lett.*, 87: 203113.

## CHAPTER 4

### Objective 1: Enhancement of Exciton Generation and Morphology of Polymer Solar Cells by CuO NPs

#### 4.1 Introduction

Copper oxide is one of the earliest semiconductor materials investigated for solar cells and it is environmentally friendly, nontoxic and highly abundant. Copper oxide has two stable forms, which are Cu<sub>2</sub>O (Cuprous Oxide) and CuO (Cupric Oxide). In the 1970<sup>th</sup> decade, Cu<sub>2</sub>O attracted huge attention and the interest on Cu<sub>2</sub>O decreased within ten years. Rai [1, 2] reported the developments achieved during that period. According to his conclusions and suggestions, the reasons for the decline in the interest in copper oxide based solar cells are linked to a few essential issues:

1. Poor performance associated with using bulk copper oxide thin films. Higher performances could have been obtained if nanostructured thin films were feasible.
2. Control of the conductivity of the p-type layer by doping. Nowadays, this has been solved by nitrogen doping.
3. Schottky barrier solar cells have copper-rich or oxygen deficient surfaces that limit the performance and will always suffer from this problem.

Overall, all previous efforts were attempted using bulk copper oxide thin films. To fabricate organic/inorganic hybrid solar cells, CuO nanomaterials are added in the polymer blends. This is an emerging field in which different research groups are using different nanomaterials.

CuO form in the tenorite mineral and it has monoclinic crystal structure with lattice parameters as the following:  $a = 4.6837 \text{ \AA}$ ,  $b = 3.4226 \text{ \AA}$ ,  $c = 5.1288 \text{ \AA}$ ,  $\beta = 99.548^\circ$ ,  $\alpha$  and  $\gamma = 90^\circ$ . Crystallographic properties and crystal structure of CuO are shown in Figure 4.1 [2].

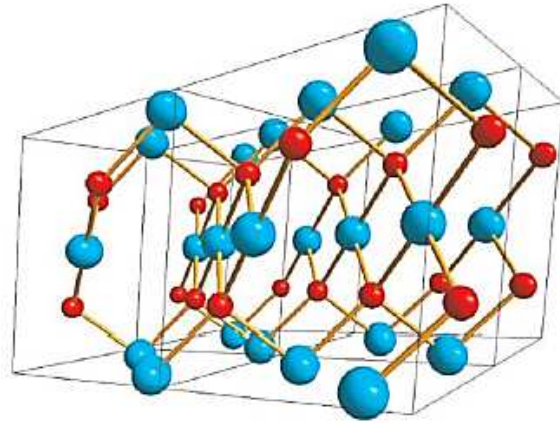


Figure 4.1: Structure of CuO crystal shown by four unit cells [2]

CuO is also considered to be an intrinsically p-type semiconductor due to copper vacancies acting as acceptors for the hole conduction. The band gap energy of CuO is 1.5 eV, which is close to the ideal energy gap of 1.4 eV required for solar cells to allow good solar spectral absorption [3]. Using density functional theory (DFT) calculations, B. K. Meyer *et al* [2] reported the values of the electronic bands of CuO. Figures 4.2 (a) and 4.2 (b) 5 show the band structure and density of states of the CuO compound; respectively. The calculated band gap ( $E_g = 1.25$  eV) is in accord with experimentally reported band gap value in the range from 1.0 to 1.9 eV. The energy bands calculation was based on a strong hybridization between Cu 3d and O 2p states and the conduction band proximity of the Fermi level is formed mainly by the Cu 3d (Cu  $3d_{x^2-y^2}$  ↓ states) [4].

Semiconductor materials can contain some amount of impurities which affect the lattice parameter of the crystal. A change in lattice parameter creates a strain on the crystal structure. However, the changes in the lattice parameters are generally negligible. The impurity level of

the CuO NPs is shown in Table 3.1 (a). On the other hand, incorporation of dopant impurities affects the lattice parameters in two distinct ways.

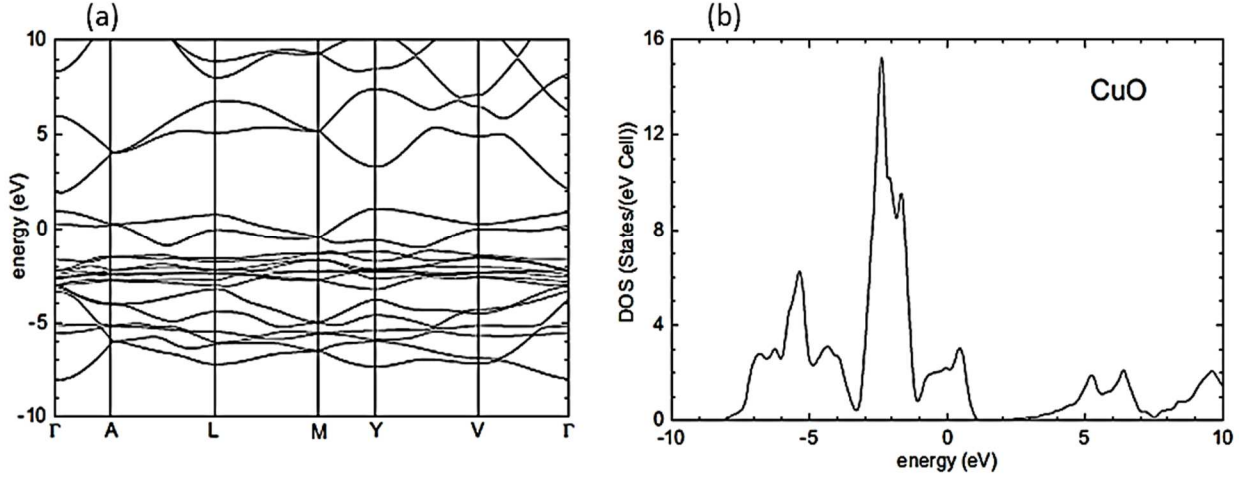


Figure 4.2: Calculated band structures and density of states (DOS) of CuO [2]

First effect occurs with a size effect when an impurity atom with different size replaces an atom within the crystal structure. The second is an electronic effect which can change the potentials. As an example, donors inject the electrons to the conduction band by n-type doping. The energy of the system can be reduced due to a decrease of the conduction-band minimum. This type of position shift of the conduction band occurs with volume change of the crystal. The deformation potential effect can be calculated by minimization of the sum of the elastic energy. Using bulk modulus of material B and a hydrostatic deformation  $\epsilon = \Delta a/a$ , the elastic energy can be written by [5];

$$E_e = \frac{9}{2} B \epsilon^2 \quad (4.1)$$

The corresponding volume change ( $\Delta V/V = 3\epsilon$ ) leads to a shift in the conduction band and the conduction band shift can be written as [5]:



$$\Delta E_c = a_c 3\epsilon \quad (4.2)$$

Where,  $a_c$  is the “absolute” deformation potential for the conduction - band minimum. Substituting  $n$  (electron concentration), the energy in the conduction band is:

$$E_d = n a_c 3\epsilon \quad (4.3)$$

Using equations 4.1 and 4.2;

$$\epsilon = \frac{\Delta a}{a} = -\frac{a_c}{3B} n = \beta_e n \quad (4.4)$$

where  $\beta_e$  indicates the deformation-potential effect for electrons.

$$\beta_e = -\frac{a_c}{3B} \quad (4.5)$$

A similar effect can be observed for holes in the valence band.

Therefore,  $\beta_h$  (deformation-potential effect for holes) can be obtained as:

$$\beta_h = \frac{a_v}{3B} \quad (4.6)$$

where  $p$  is the hole concentration and  $a_v$  is the absolute deformation potential for the valence-band maximum. The positive sign of  $\beta_e$  indicates that adding electrons in the conduction band results in an expansion of the lattice. Similarly, the positive sign of  $\beta_h$  indicates that adding holes in the valence band results in an expansion of the lattice [5].

The P3HT and PC70BM are considered as an ideal donor-acceptor pair for organic solar cells due to their unique properties such as; ease of processing, possible recyclability, low cost, scalability, and applicability as sustainable materials. However, many critical issues in these materials remain unresolved, such as a viable PCE due to limited optical absorption. On the other hand, inorganic semiconductors such as CuO possess better electronic properties, such as extremely high optical absorption, high charge mobility, and better thermal stability. The nanoparticles of these inorganic semiconductors exhibit even better electronic, optical, photoconducting, and luminescent properties [6]. In order to take advantages of both materials,

nanoparticles of inorganic semiconductors (CuO NPs) are combined with conducting polymers (P3HT/PC70BM) in hybrid photovoltaic-cell materials, where the combined absorption bands of both materials can yield better sun energy harvest [7]. A schematic illustration of the structure of the photovoltaic devices which are fabricated for this study is shown in Figure 3.2 (a). The fabrication and characterization methods are described in sections 3.2.1 and 3.3 respectively.

## 4.2 Results and Discussion

### 4.2.1 Performance Characteristics

The performance of the devices containing CuO NPs improved in comparison to the reference devices; this can be attributed to the enhanced light absorption of the polymer films with CuO NPs. The short-circuit current density ( $J_{sc}$ ), open-circuit voltage ( $V_{oc}$ ), fill factor (FF), and PCE, which is defined as the ratio of the products of  $V_{oc}$ ,  $J_{sc}$ , and FF to the total incident power density of all the cells are listed in Table 4.1.

Table 4.1: Performance parameters of P3HT/PCBM/CuO-NPs hybrid solar cells

CuO NPs(mg)	$J_{sc}$ (mA/cm <sup>2</sup> )	$V_{oc}$ (V)	FF (%)	PCE (%)
0.0	5.234	0.658	61.15	2.106
0.2	5.726	0.675	66.52	2.571
0.4	5.993	0.670	66.21	2.632
0.6	6.484	0.673	68.00	2.963
0.8	6.320	0.668	68.50	2.895
1.0	6.122	0.674	66.84	2.758

After incorporating CuO NPs into P3HT:PC70BM layer,  $V_{oc}$  did not seem to change significantly, however,  $J_{sc}$  increased from 5.234 to 6.484 mA/cm<sup>2</sup> and the FF increased from

61.15% to 68.0% which is 11.2% improvement in comparison to the cells without CuO NPs. Though the FF increases steadily in all the cells, the  $V_{oc}$  and  $J_{sc}$  show a sinusoidal behavior, increasing with the weight of CuO NPs upto a maximum and then decreasing beyond a certain (0.6 mg) composition. As a result, the PCE follows the same trend, increasing from 2.10% to 2.96% and then decreasing with subsequent increase in the amounts of CuO in the solar cell. In spite of this behavior, the increase in PCE translates to a 40.7% enhancement in the cell containing 0.6 mg of CuO NPs in comparison to the reference cell.

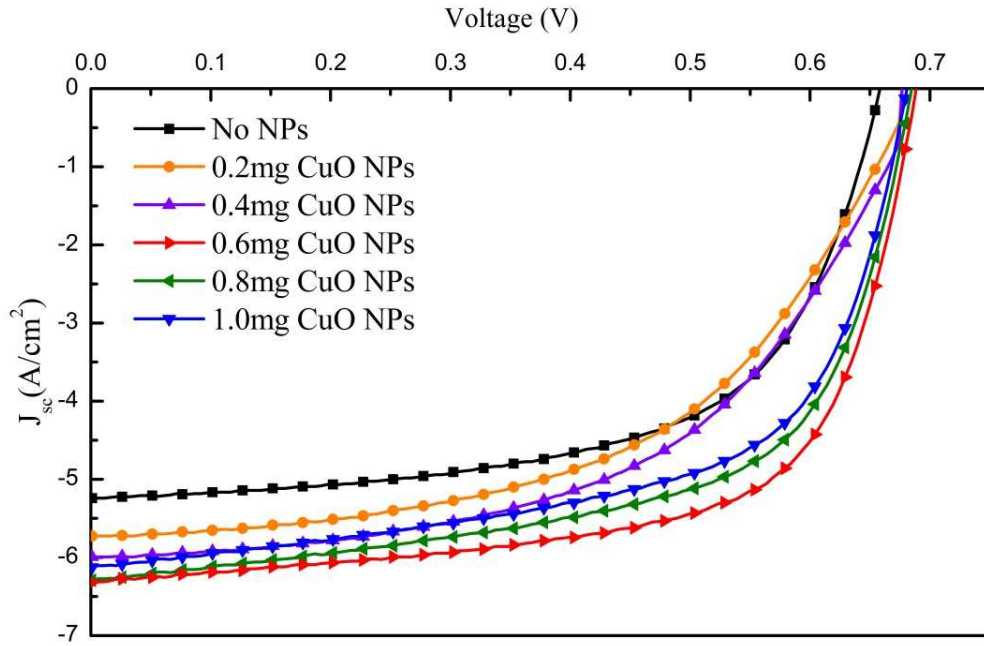


Figure 4.3: Current Density-Voltage characteristics of P3HT/PCBM/CuO-NPs hybrid solar cells

The PCE of the PSCs containing CuO NPs shows a higher PCE compared to some of organic hybrid solar cells reported in the literature. For instance, the SiNW-19 nm Ag NPs based hybrid solar cells had a PCE of 2.81% and the cells based on ZnO had a PCE of 2.37%, this translates to an increase in the PCE of the CuO based solar cells by 5.3% and 24.9%, respectively. The

current density–voltage (J–V) characteristics of the hybrid solar cells containing CuO NPs are compared to the reference cell in Figure 4.3.

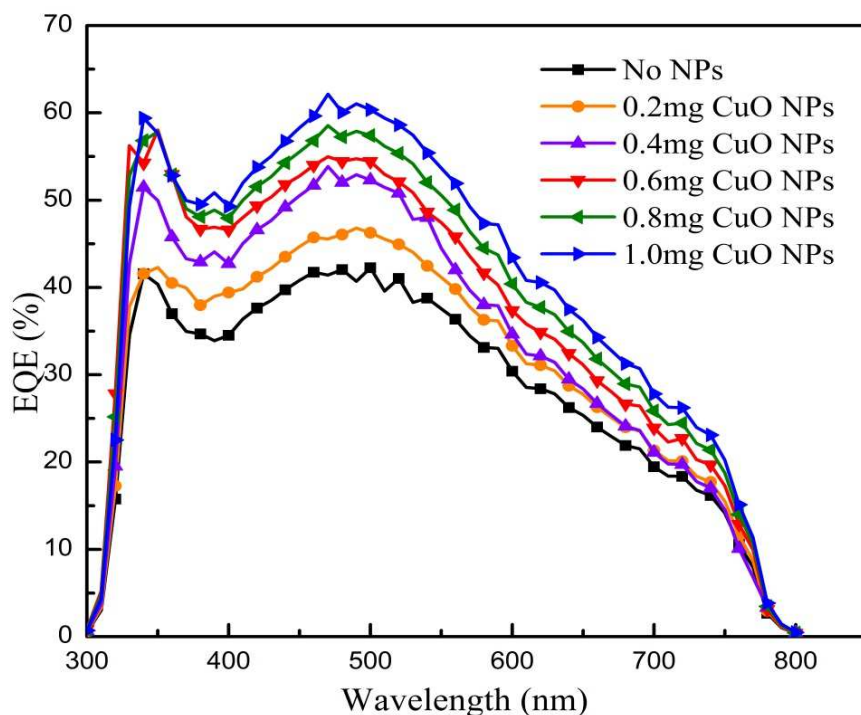


Figure 4.4: External quantum efficiency of P3HT/PCBM/CuO-NPs hybrid solar cells

According to Equation 2.51, the  $J_{sc}$  is linearly correlated to the EQE. Both EQE and UV–Vis absorption measurements of the solar cells show that the  $J_{sc}$  increases with increasing the amount of CuO NPs. It is clear from the UV–Vis absorption spectra that the absorption of P3HT:PC70BM cell in the region of 420–600 nm is enhanced after the incorporation of CuO NPs. The EQE is defined as the ratio of the number of charge carriers collected by the solar cell to the number of photons shining on the solar cell from outside sources. EQE measurements for solar cells with various amounts of CuO NPs are shown in Figure 4.4. The EQE increased over a broad wavelength ranging from 300 to 600 nm and the maximum EQE values for CuO NPs, with

1.0 mg, 0.8 mg, 0.6 mg, 0.4 mg, and 0.2 mg devices were 62, 58, 54, 53, and 46%, respectively, while that of the reference cell (no CuO NPs) was 42%.

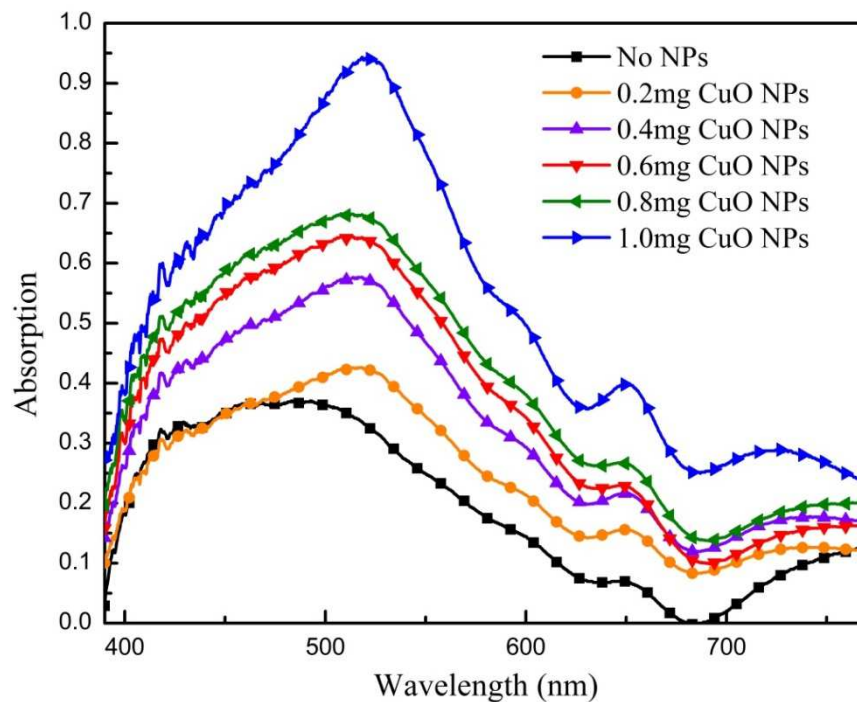


Figure 4.5: Optical absorption spectra of P3HT/PCBM/CuO-NPs hybrid solar cell

As described in the chapter 2, the EQE depends on five major efficiency steps which govern by associated efficiencies as shown in Equation 2.52. The photon absorption ( $\mu_A$ ) efficiency describes the photon absorption capacity of the thin layers. The optical absorption coefficient, band gap, and the thickness of the photoactive layer are the major determinants of photon absorption yield. This serves as the most desired approach for increasing the  $J_{sc}$  of a hybrid device [8]. In hybrid solar cells, absorption may be enhanced by incorporating inorganic semiconductor nanoparticles. This implies that the electronic composition of the inorganic material will influence the  $J_{sc}$  of the device as well.

Figure 4.5 shows the spectral diagram for optical absorption of CuO nanoparticle incorporated P3HT/PCBM photovoltaic cells. Absorption of a photon with energy greater than the  $E_g$  value (1.99 eV) for P3HT generates an exciton which is diffused to the P3HT/PCBM interface. To investigate the optical absorption in CuO NPs, the absorption spectrum of the CuO NPs sample was obtained as shown in Figure 4.6. The figure depicts absorption peaks intensity at 2.9 over the wavelength range of 300nm - 400nm for the pure CuO NPs samples. The  $E_g$  value of the CuO NPs is calculated using Tuac formula [9];

$$(\alpha h\nu)^m = B(h\nu - E_g) \quad (4.7)$$

where  $h\nu$  is the energy of incident photons in eV and  $m = 1/2$  for indirect and 2 for direct allowed transitions,  $B$  is a constant related to the material,  $h$  is Plank's constant,  $\nu$  is the frequency of the photon,  $E_g$  is the optical band gap in eV. Assuming direct transitions between the valence band and the conduction band of CuO NPs, the  $E_g$  can be determined by a plot of  $(\alpha h\nu)^2$  versus  $(h\nu)$  at  $\alpha = 0$ . The estimated  $E_g$  value for CuO NPs is approximately 2.14 eV. Also, the  $E_g$  value of the P3HT/PCBM blend was estimated using the same method and it was found to be 2.71 eV. After incorporating CuO NPs into the P3HT/PCBM blend, the  $E_g$  value was 2.64 eV. However, the  $E_g$  value did not change significantly with changing concentrations of CuO NPs in the blend.

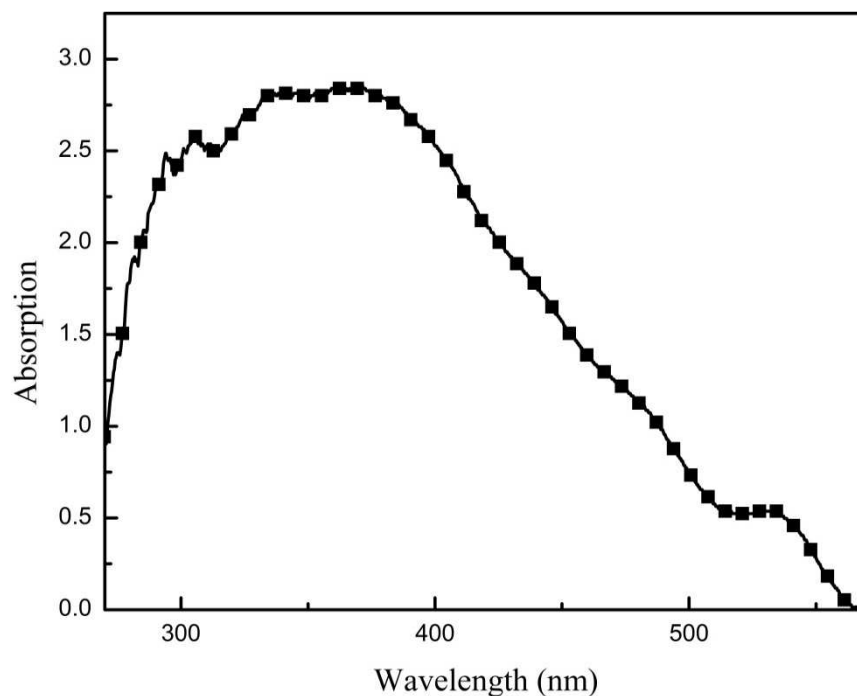


Figure 4.6: The absorption spectra of these CuO NPs

The parameter  $\mu_{diff}$  represents the ability of an exciton to diffuse to a donor/acceptor (D/A) interface through the polymer without recombination. The exciton diffusion length in conjugated polymers generally should be around 10–20 nm [10]. Diffusion of excitons to the D/A interface is a prerequisite for generation of separated negative and positive charges. Since excitons are neutral species, electric fields have no influence on their motion and they diffuse by way of random hops steered by the concentration gradient. Excitons which fail to reach the D/A interface are lost for the energy conversion and do not contribute to the photocurrent [11].

The improvement in efficiency of this CuO NPs incorporated system can be attributed to the enhanced charge collection efficiency which results from the availability of better pathways for charge transport and reducing the need of inter-particle hops for charge carriers. Existence of a continuous percolated nanomorphology in this system with optimum amount of CuO NPs provides a better interconnected network, in which the donor and acceptor materials are



interdigitated at the nanometer scale. This structure facilitates efficient, direct transport pathways for both electrons and holes thereby averting the need for inter-nanoparticle hops.

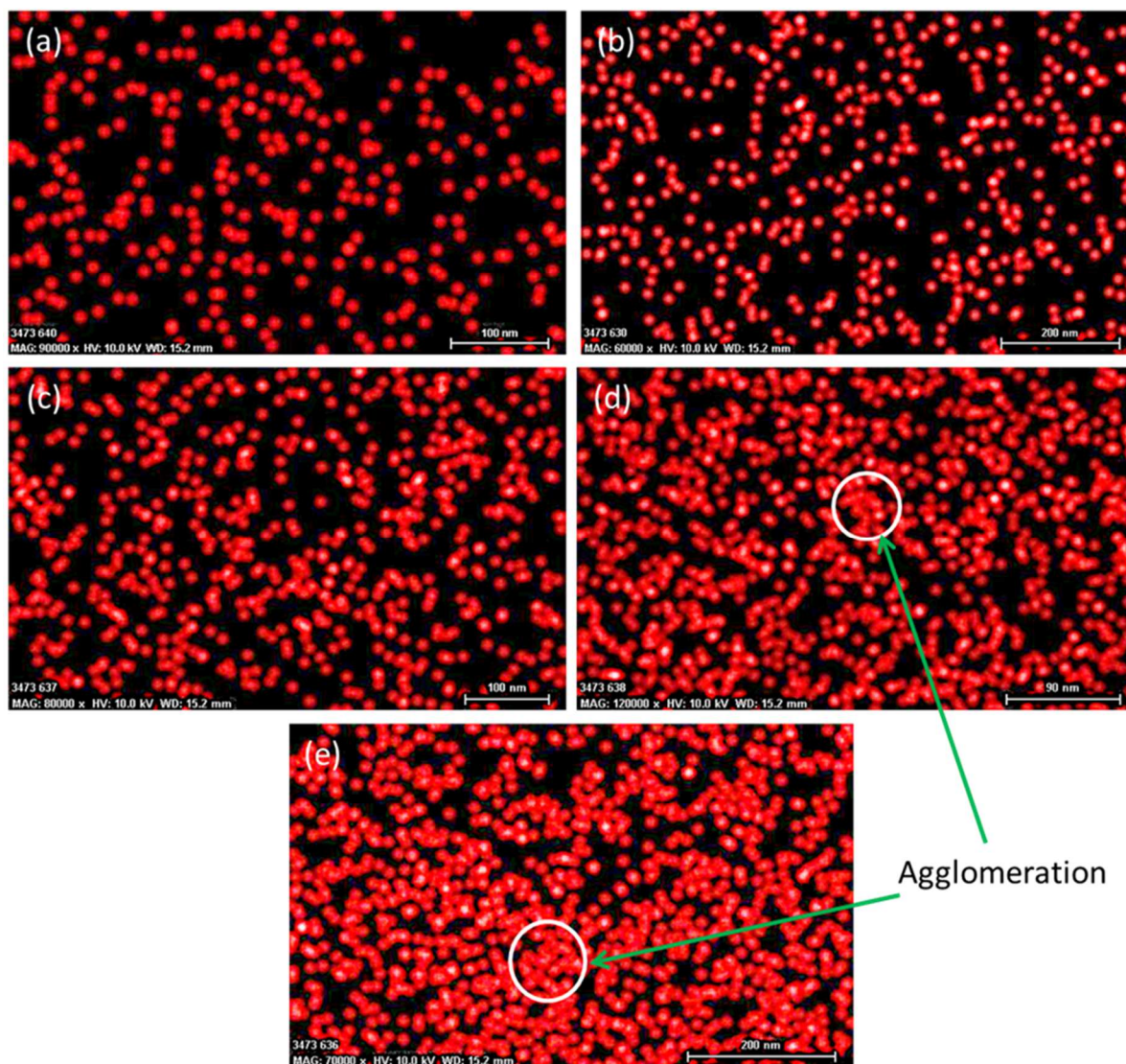


Figure 4.7: EDX mapping showing the distribution of elemental copper in the P3HT/PCBM active layer of PSCs containing: (a) 0.2 mg, (b) 0.4 mg, (c) 0.6 mg, (d) 0.8 mg and (e) 1 mg CuO NPs



Further, it permits the photo-induced charges to be in separated state for an extended lifetime and diminishes the possibility of recombination of charges. As a result, this hybrid system improves both the quantum efficiency and the FF, leading to a higher PCE.

However, the PCE of the solar cells seem to increase drastically as the amount of CuO NPs are increased in the active layer up to 0.6 mg and then drop slightly as the amount of CuO NPs are increased further. This may indicate some hindrance to the optical absorption in the active layer either due to the increasing thickness as the amount of CuO NPs are increased further or due to agglomeration of the CuO NPs in the active layer at higher concentrations. Figure 4.7 shows the EDX mapping of elemental copper in the active layer of the solar cells. This can be used to indicate the distribution of CuO NPs in the active layer. Higher agglomeration can be seen in Figures 4.7d and 4.7e, which correspond to the cells containing 0.8 and 1 mg of CuO NPs; respectively.

The volume fraction of the CuO NPs in the EDX mapping was calculated using IMAGEJ software. IMAGEJ is a JAVA-based image processing program which can be used to solve many image processing and analysis problems. The converted images with the optimized threshold for particle detection are shown in Figure 4.8. The calculated volume fractions of the CuO NPs in the EDX mappings are 29.99, 36.04, 43.81, 53.7, and 66.52 for the thin films with 0.2, 0.4, 0.6, 0.8, and 1.0mg of NPs; respectively.

The next parameter is the charge transport efficiency ( $\mu_{tr}$ ), which describes the efficiency of charge carrier transport throughout the device. Charge transportation along the device determines the current density and hence affects the final performance [12]. Charge transport progresses through hopping of charges between energy states in organic materials and recombination spots and traps in the photoactive layer can impede this process. The continuous network provided by

the CuO NPs can greatly reduce the need for charge carriers to hop during their transportation to the electrodes, so this hybrid system shows a better performance.

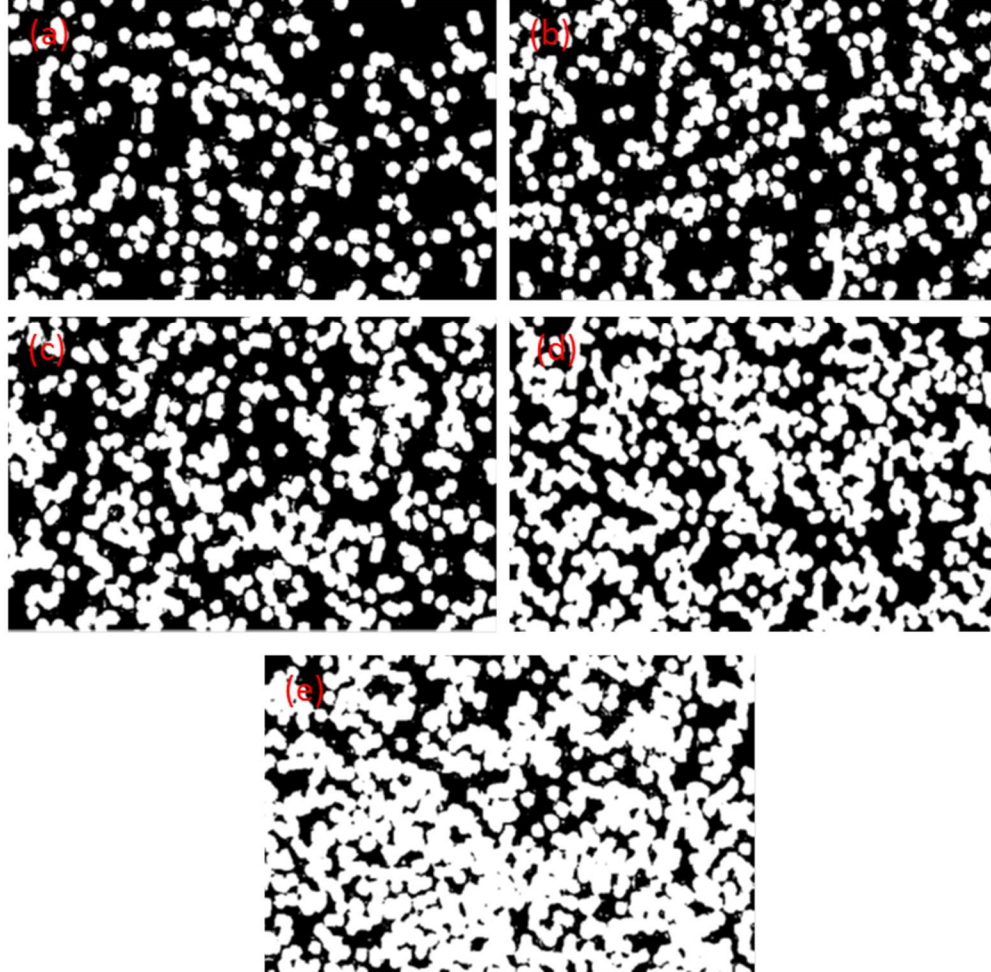


Figure 4.8: Converted EDX images with the optimized threshold

The charge collection efficiency ( $\mu_{cc}$ ) at electrodes indicates the potential of charge carriers to be injected into the electrodes from the photoactive layer. Electronic composition of the device plays a key role in accomplishing this step. Successful injection of electrons into the cathode depends on the magnitude of the conduction band energy level of the acceptor material, compared to the vacuum level, being lower than the work function of the donor material [13].

Similarly, for successful injection of holes into the anode, the magnitude of the conduction band energy level of the acceptor material, compared to the vacuum level, should be higher than the work function of the transparent anode. In this study, we used PEDOT:PSS layer as the anode and aluminum as the cathode material. Both these materials satisfied the above requirements.

A schematic energy level diagram of the P3HT/CuO/PCBM active layer is shown in Figure 4.9(a). The band structure of P3HT and PCBM [14] makes them an ideal donor and acceptor pair. In comparison to P3HT, the energy levels of the conduction and valence bands of CuO and the lowest unoccupied molecular orbital and highest occupied molecular orbital (HOMO) of PCBM are such that CuO and PCBM can form a semiconductor heterojunction; this makes them a suitable donor and acceptor pair. The electrons thus generated can transfer from the conduction band of the CuO to the PCBM and the separated holes can in turn transfer from the valence band of the CuO to the ITO through the structure.

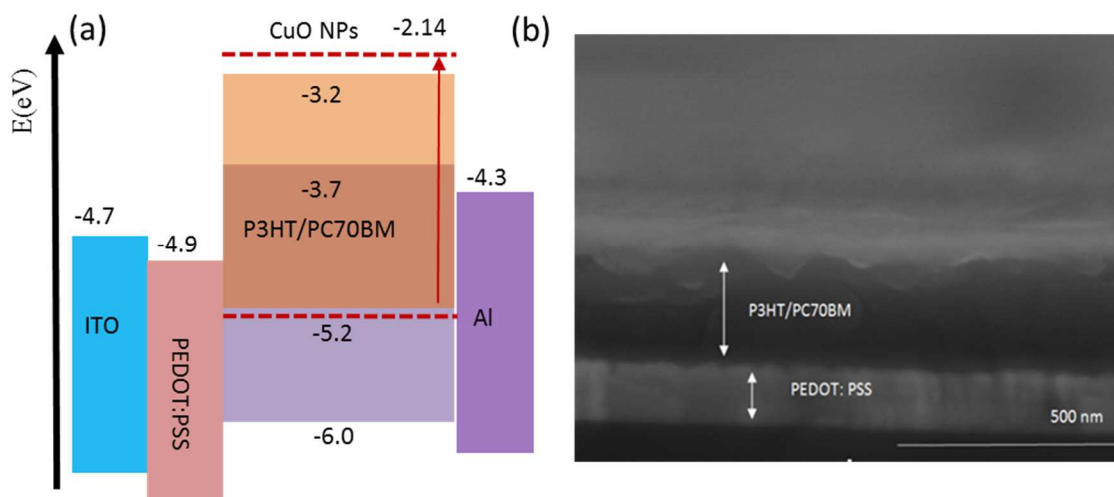


Figure 4.9: (a) Schematic band structure of the P3HT/PCBM/CuO NP active layer, (b) SEM image of the polymer solar cell

A SEM micrograph of the fabricated solar cell showing the spin coated PEDOT:PSS and the CuO NPs/P3HT:PCBM layers is shown in Figure 4.9(b). A thin layer (40 nm) of PEDOT:PSS layer is required to facilitate the transfer of the carriers to the ITO anode. The thickness of the P3HT/PCBM active layer was restricted to 100–150 nm to avoid the recombination of charges.

#### 4.2.2 Morphology and Surface Characteristics

The XRD patterns of CuO NPs are shown in Figure 4.10. Different peaks were observed at  $(2\theta) = 32.49^\circ$  (110),  $35.52^\circ$  (002),  $38.72^\circ$  ( $\bar{1}11$ ),  $48.76^\circ$  ( $\bar{2}02$ ),  $53.46^\circ$  (020),  $58.32^\circ$  (202),  $61.51^\circ$  ( $\bar{1}13$ ),  $66.23^\circ$  (022) and  $68.07^\circ$  (220) corresponding to different planes of monoclinic phase of CuO.

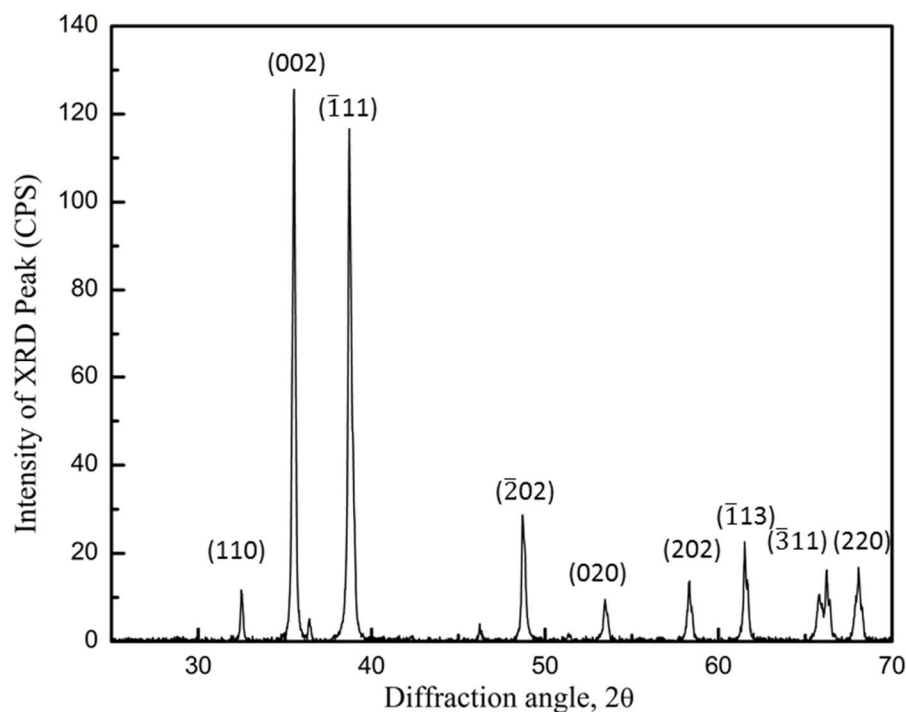


Figure 4.10: XRD pattern of CuO NPs sample

It is clear that the major peaks located at  $2\theta = 35.52^\circ$  and  $38.72^\circ$  are the characteristic peaks for the pure monoclinic phase of CuO NPs. The sharp and narrow diffraction peaks indicate that the material has good crystallinity and no other impurities were detected [15].

The effect of the CuO NPs on the crystallinity of P3HT was studied by XRD and DSC. Figure 4.11 shows the XRD spectrum which indicates an improvement in the crystallinity (peak intensity and width) of the hybrid solar cells containing CuO NPs. This may be due to the fact that a small amount of the P3HT chains escape from the amorphous region and self-organize forming crystalline phases in the blend. The heterogeneous nucleation occurs on insoluble impurity particles. Considering Equation 2.48, a reduction in the  $\gamma^*$  (specific surface free energy factor) would facilitate nucleation at lower temperature values. Therefore, the impurities improve the nucleation rate in the blend. In the P3HT/PCBM blend, CuO NPs act as impurities, thus improving the nucleation rate of the P3HT molecules. The percent crystallinity was determined by the ratio of the intensities of the observed and the background peaks [16].

$$\begin{aligned} \% \text{ Crystallinity} &= \frac{\text{Observed}}{\text{Background}} \\ &= \frac{(\text{Max.} - \text{Min.}) \text{intensity of the peak}}{(\text{Max.} - \text{Min.}) \text{intensity of the background}} \end{aligned} \quad (4.8)$$

The sample without any CuO NPs was considered as the background, and the minimum and maximum peak intensity values in Equation 4.8 represent the peak minima and the maxima values.

The effect of CuO NPs on the crystallinity of P3HT:PC70BM thin films were further analyzed by DSC to corroborate the XRD results.

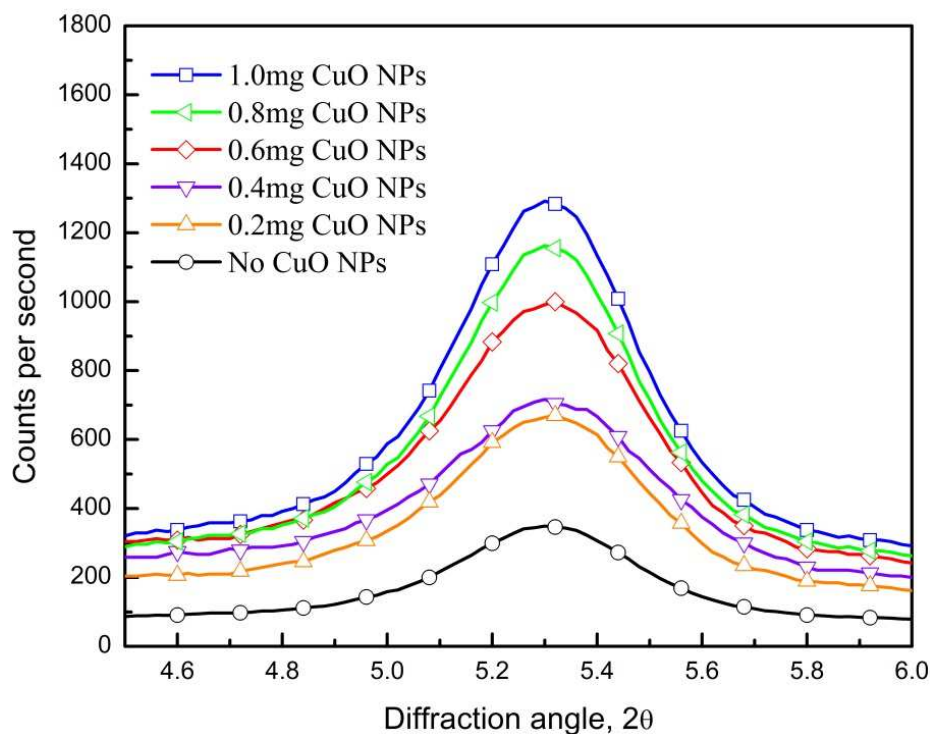


Figure 4.11: XRD spectra for CuO NPs incorporated P3HT/PCBM thin films

The percentage crystallinity ( $X_c$ ) of P3HT in a blend of P3HT:PC70BM:CuO NPs was calculated using the DSC melting and crystallization enthalpies using the following equation:

$$\%Crystallinity (X_c) = \left( \frac{\Delta H_m - \Delta H_c}{\Delta H} \right) \cdot 100 \quad (4.9)$$

where  $\Delta H_m$  is the enthalpy of melting (in J/g of sample) of semicrystalline polymer in a blend,  $\Delta H_c$  is the enthalpy of crystallization, and  $\Delta H$  is the enthalpy of melting of 100% crystalline polymer ( $\Delta H$  of P3HT = 99 J/g) [17].

The crystallinity values determined by both XRD and DSC (Figure 4.12) show that the percent crystallinity, in general, increases gradually as the amount of CuO NPs increases in the P3HT:PC70BM polymer blend. However, the crystallinity values determined by XRD were higher and ranged from 1 to 3.7% in comparison to the values obtained from DSC using

Equation 4.9 and ranged from 0.56 to 1.29% in PSCs containing 0–1 mg of CuO NPs, respectively.

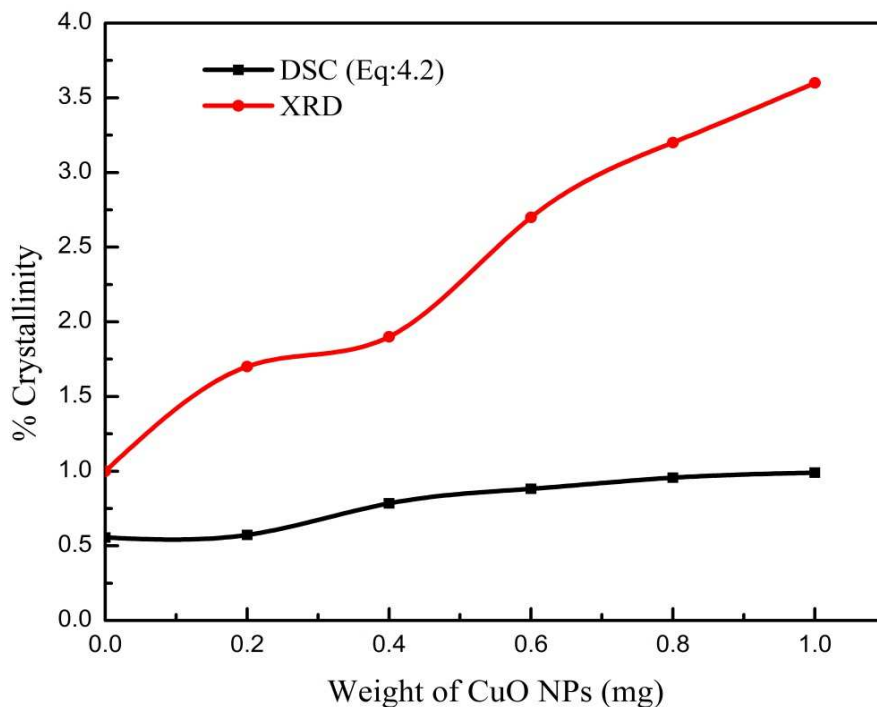


Figure 4.12: Crystallinity of PSC's determined by XRD and DSC-Eq: (4.9)

The difference in the values observed may be attributed to the difference in the amount of sample analyzed. For example, in XRD, a larger portion of the sample or the entire P3HT/PC70BM layer containing CuO NPs can be analyzed where as in DSC, the total sample size is restricted to 10 mg and this sample size may not contain an ample amount of the polymer active layer and the CuO NPs to give a better resolution in comparison to XRD.

On the other hand, instead of using Equation 4.9, if one was to use another commonly used method, Equation 4.10 to determine the percent crystallinity of a polymer, which is defined as the ratio of the enthalpy of fusion ( $\Delta H_m$ ) of the polymer sample to the enthalpy of fusion of the

100% crystalline phase of the polymer ( $\Delta H_m^o$ ), the percent crystallinity values will change as this equation does not consider the heat required for crystallization of the samples [18].

$$\%Crystallinity(X_c) = \left( \frac{\Delta H_m}{\Delta H_m^o} \right) \cdot 100 \quad (4.10)$$

From Figure 4.13, it is clearly evident that the crystallinity values determined by DSC, using Equation 4.10 are now higher and are in the range of 5.81–6.06% as they represent only the heat required to melt the crystalline domains formed by self-organization [19] in the P3HT:PC70BM blend as the CuO NPs are added. One can also observe that the crystallinity values now show a sinusoidal behavior instead of a steady increase as the amount of CuO NPs increase in the polymer active layers. The former argument on the sample size does not seem to support this new trend as the change in crystallinity now seems to be independent of the sample size and seems to depend on other parameters which may be related to the ability of the CuO NPs to support or hinder the formation of crystalline domains. One can speculate that this may be due to the dispersion of CuO NPs in the polymer blend.

A sudden drop in the initial crystallinity followed by a steep increase, as the CuO NPs are increased, may be attributed to the dispersion of the particles within the active layer. However, increasing the amounts of NPs beyond a certain composition seems to lower the crystallinity; this may be due to agglomeration of the CuO NPs hindering the crystalline phase formation.

Though this behavior is different from the one observed by XRD, it seems to resemble the performance parameters shown in Table 4.1. The highest PCE and crystallinity values are observed in samples containing 0.6 mg CuO NPs (Figure 4.14). From this observation, one can say that the optimum composition is 0.6 mg of CuO NPs in the active layer of the PSC. In general, the increase in crystallinity observed by XRD or DSC may be attributed to an improvement in nanoscale phase-separation of the P3HT/PCBM [20].



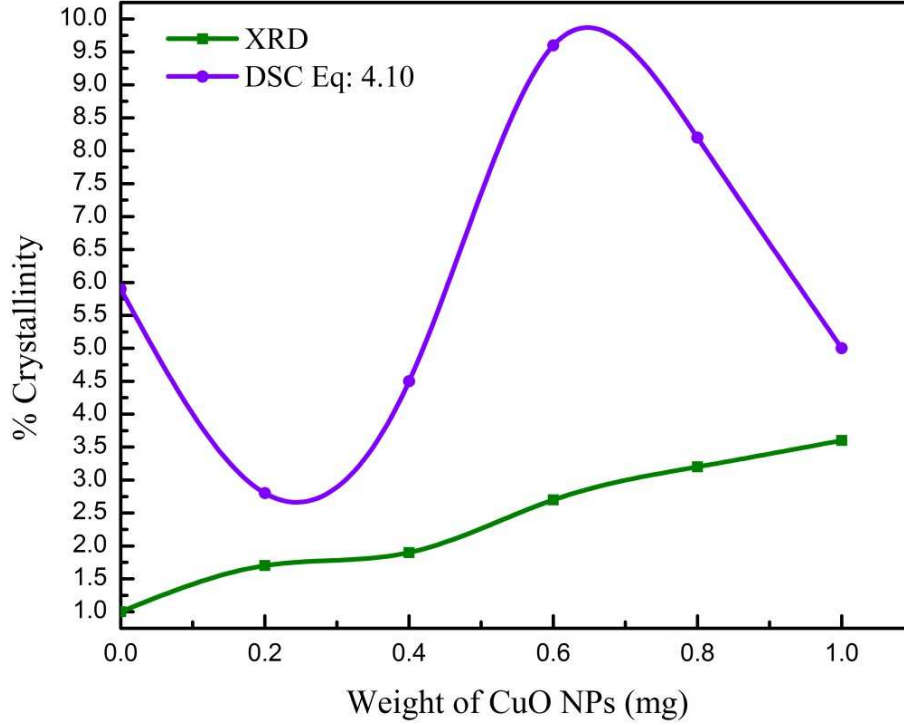


Figure 4.13: Crystallinity of PSC's determined by XRD and DSC-Eq: (4.10)

The P3HT crystallite domains adjust the degree of phase separation leading to a decrease in exciton diffusion length. Also there could be a decrease in the spaces between P3HT chains, thus improving the charge transport inside P3HT domains [21] causing the PCE to decrease beyond the optimum amount of NPs in the blend. This could be the main reason that the PCE does not follow the same trend of EQE and optical absorption after 0.6 mg of CuO NPs in the active layer.

The exciton dissociation ( $\mu_{diss}$ ) is a process in which the electron and hole bound within the exciton are released by a driving force generated with the energy offset formed at the D–A interfaces. This energy offset must be larger than the excitonic binding energy in the material to facilitate charge transfer [22]. Exciton dissociation takes place only at the boundaries between the inorganic semiconductor and the conjugated polymer hence, broader distribution of the

interface throughout the active layer plays a major role in improving efficiency of the solar cell [23]. Incorporation of CuO NPs could enhance the interfacial distribution by increasing the surface area which can lead to efficient dissociation of excitons into holes and electrons. Surface analysis by AFM is thus useful to understand this phenomenon.

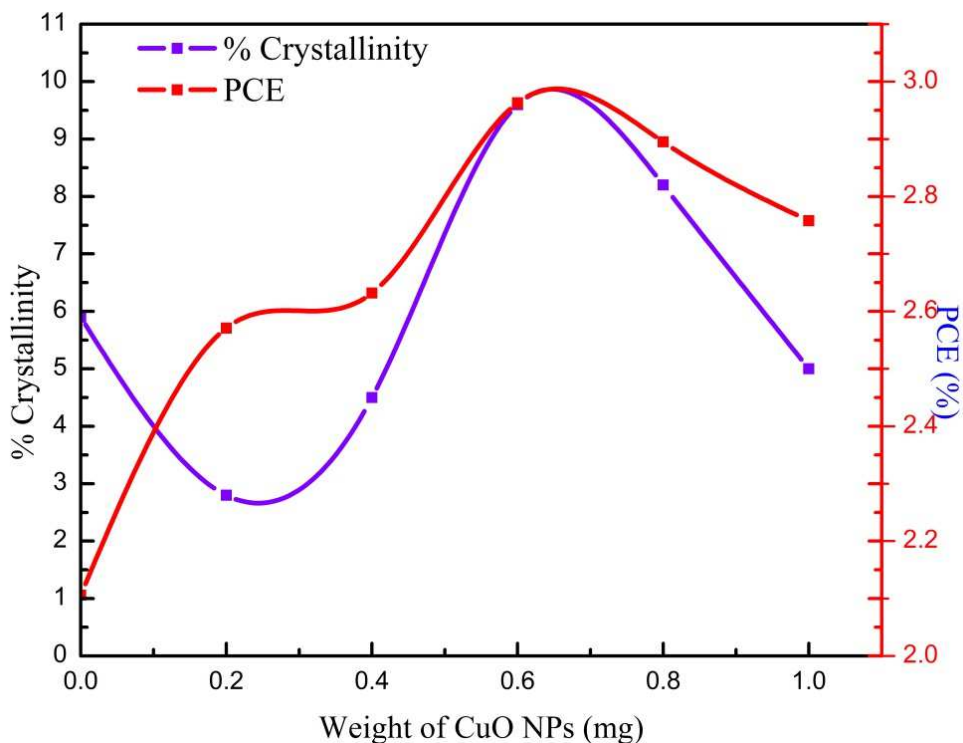


Figure 4.14: Effect of CuO NPs on the crystallinity and PCE of the PSCs

AFM surface images of P3HT:PC70BM films with different amounts of CuO NPs are shown in Figure 4.15. The surface morphology of the P3HT/PCBM-CuO NPs layers shows higher surface peaks and an obvious increase in surface roughness. The root-mean-square roughness ( $\sigma_{rms}$ ) value increased from 0.11 nm in the thin film without CuO NPs up to 0.47 nm

in the thin film with 1mg of CuO NPs. The optimum cell with 0.6mg of CuO NPs shows a surface roughness value of 0.31 nm.

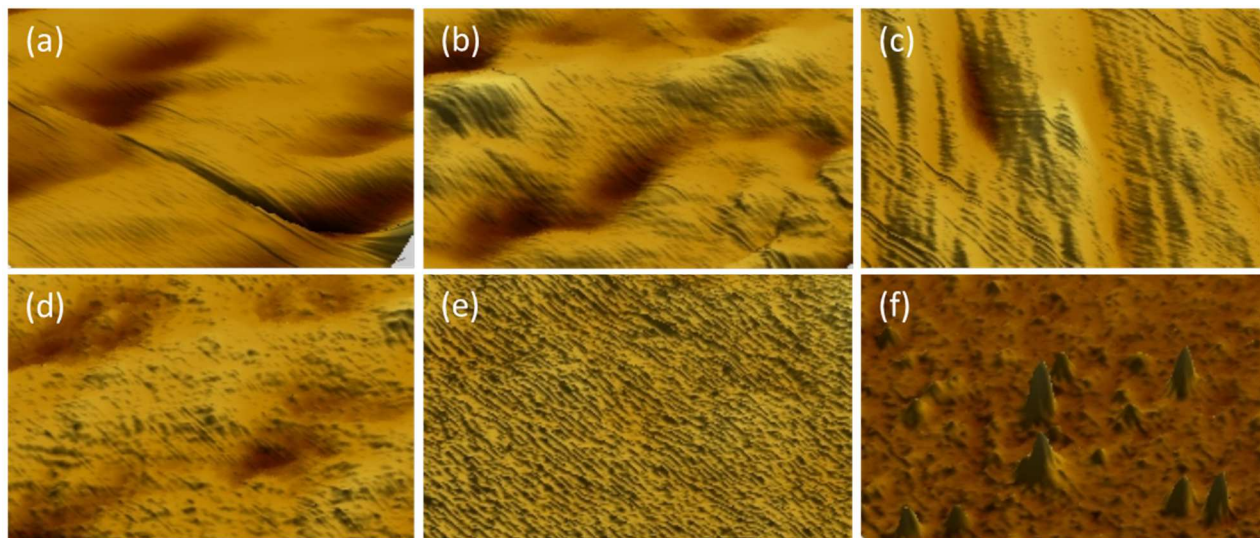


Figure 4.15: AFM images for P3HT/PCBM layers with (a) No CuO NPs, (b) 0.2mg CuO NPs, (c) 0.4mg CuO NPs, (d) 0.6mg CuO NPs, (e) 0.8mg CuO NPs, (f) 1mg CuO NPs

This can be the result of increased nanoscaled phase separation between the crystalline P3HT and the PC70BM acceptor. However, the surface roughness values of the cells are very small indicating highly homogeneous films. Increase in surface roughness allows more space for P3HT crystallites to form, thereby increasing crystallinity. Furthermore, increased surface roughness leads to an increase in interfacial contact area between the PEDOT:PSS and P3HT/PCBM-CuO NPs layer, allowing more efficient hole collection at the anode and thereby improving  $J_{sc}$  and FF.

The driving force required for exciton dissociation is determined by the energy gap between the ionization potential of the donor and the electronic affinity of the acceptor which have a linear relationship with the  $V_{oc}$  [24]. Therefore, we find a direct correlation between the driving force and  $V_{oc}$ . Since the addition of CuO NPs has not significantly changed the value of

$V_{oc}$  for the PSC, the CuO NPs may not change the active layer P3HT conjugation length. As a result, the HOMO energy level of P3HT remains unchanged therefore; CuO NPs do not seem to contribute to enhance the driving force required to increase the exciton dissociation.

### 4.3 Conclusions

CuO NPs were added to P3HT/PC70BM polymer blends in order to improve the PCE. It was shown that the incorporation of CuO nanoparticles at an optimum level of 0.6 mg yields 40.7% improvement in PCE due to enhancement of the five factors affecting the EQE: (i) photo-absorption increased with elevated exciton generation rate; (ii) the amplification of exciton diffusion coefficient due to enhanced hole and electron mobility; (iii) exciton dissociation ability increased by enhancement of interfacial distribution; (iv) the charge transport process was facilitated by providing better pathways in a continuous internal structure, and (v) the carrier collection which depends on electronic properties of electrode materials did not change to a significant extent with the addition of CuO NPs.

## References

- [1] Rai, B.P., 1988. Cu<sub>2</sub>O solar cells: A review, *Solar Cells*. 25: 265-272.
- [2] Meyer, B. K.*et al*, 2012. Binary copper oxide semiconductors: From materials towards devices, *Phys. Status Solidi B*. 249(8): 1487–1509.
- [3] Kidowaki, H., Oku, T., and Akiyama, T., 2012. Fabrication and characterization of CuO/ZnO solar cells. *Journal of Physics: Conference Series*. 352:1.
- [4] Ekuma, C. E., Anisimov, V. I., Moreno, J., and Jarrell, M., 2014. Electronic Structure and Spectra of CuO, *arXiv: 1305.6283v3 [cond-mat.str-el]*. 17 Feb 2014.
- [5] Chris, G., Walle, V., 2003. Effects of impurities on the lattice parameters of GaN. *Physical review B*. 68: 165209.
- [6] Kim, C. H., Cha, S. H., Kim, S. C., Song, M., Lee, J., Shin, W. S., Moon, S. J., Bahng, J. H., Kotov, N. A., and Jin, S. H., 2011. Silver Nanowire Embedded in P3HT: PCBM for High-Efficiency Hybrid Photovoltaic Device Applications. *ACS Nano*. 5(4): 3319–3325.
- [7] Misra, R., Fu, B. X., Plagge, A., and Morgan, S. E., 2009. POSS-Nylon 6 Nanocomposites: Influence of POSS Structure on Surface and Bulk Properties. *J. Polym. Sci., Part B*. 47(11):1088–1102.
- [8] Bundgaard, E., and Krebs, F. C., 2007. Low Band Gap Polymers for Organic Photovoltaics. *Sol. Energy Mater. Sol. Cells*. 91(11): 954–985.
- [9] El Sayed, A. M., El-Gamal, S., Morsi, W. M., Mohammed, g., 2015. Effect of PVA and copper oxide nanoparticles on the structural, optical, and electrical properties of carboxymethyl cellulose films. *J Mater Sci*. 50:4717–4728.
- [10] De Freitas, J. N., Korala, L., Reynolds, L. X., Haque, S. A., Brock, S. L., and Nogueira, A. F., 2012. Connecting the (Quantum) Dots: Towards Hybrid Photovoltaic Devices Based on Chalcogenide Gels. *Phys. Chem. Chem. Phys*. 14(43):15180–15184.
- [11] Brabec, C. J., Gowrisanker, S., Halls, J. J. M., Laird, D., Jia, S., and Williams, S. P., 2010. Polymer–Fullerene Bulk-Heterojunction Solar Cells. *Adv. Mater*. 22(34): 3839–3856.
- [12] Baeten, L., Conings, B., Boyen, H. G., D’Haen, J., Hardy, A., D’Olieslaeger, M., Manca, J. V., and Van Bael, M. K., 2011. Towards Efficient Hybrid Solar Cells Based on Fully Polymer Infiltrated ZnO Nanorod Arrays. *Adv. Mater*. 23(25):2802–2805.
- [13] George, F. A. D., Muth, M. A., Kirchartz, T., Engmann, S., Hoppe, H., Gobsch, G., Thelakkat, M., Blouin, N., Tierney, S., Carrasco-Orozco, M., Durrant, J. R., and Nelson, J., 2013. Influence of Doping on Charge Carrier Collection in Normal and Inverted Geometry Polymer:Fullerene Solar Cells. *Sci. Rep*. 3: 3335.

- [14] Yoshida, K., Oku, T., Suzuki, A., Akiyama, T., and Yamasaki, Y., 2013. Fabrication and Characterization of PCBM:P3HT Bulk Heterojunction Solar Cells Doped With Germanium Phthalocyanine or Germanium Naphthalocyanine. *Mater. Sci. Appl.* 4(4A):1–15.
- [15] Ganga R. C., Pratibha, B., Navneet K., and Mehta, S. K., 2014. Recyclable CuO nanoparticles as heterogeneous catalysts for the synthesis of xanthenes under solvent free conditions, *RSC Adv.* 4: 49462-49470.
- [16] Cullity, B. D., and Stock, S. R., 2001. Elements of X-Ray Diffraction, 3rd ed. Prentice Hall, London, UK.
- [17] Abu-Zahra, N., and Algazzar, M., 2013. Effect of Crystallinity on the Performance of P3HT/PC70BM/n-Dodecylthiol Polymer Solar Cells. *ASME J. Sol. Energy Eng.* 136(2): 021023.
- [18] Groves, I., Lever, T., and Hawkins, N., 2014. Determination of Polymer Crystallinity by DSC,” Thermal Analysis Application Brief, Thermal Analysis and Rheology, TA-123, Accessed Sept. 2014. Available at: [http://www.tainstruments.com/library\\_download.aspx?file¼TA123.PDF](http://www.tainstruments.com/library_download.aspx?file¼TA123.PDF).
- [19] Pascui, O. F., Lohwasser, R., Sommer, M., Thelakkat, M., Thurn-Albrecht, T., and Saalwächter, K., 2010. High Crystallinity and Nature of Crystal–Crystal Phase Transformations in Regioregular Poly(3-hexylthiophene). *Macromolecules.* 43(22): 9401–9410.
- [20] Sun, Y., Cui, C., Wang, H., and Li, Y., 2011. Efficiency Enhancement of Polymer Solar Cells Based on Poly(3-hexylthiophene)/Indene-C70 Bisadduct via Methylthiophene Additive. *Adv. Energy Mater.* 1(6):1058–1061.
- [21] Chang, Y. M., and Wang, L., 2008. Efficient Poly(3-hexylthiophene)-Based Bulk Heterojunction Solar Cells Fabricated by an Annealing-Free Approach. *J. Phys. Chem. C.* 112(45):17716–17720.
- [22] Gregg, B. A., and Hanna, M. C., 2003. Comparing Organic to Inorganic Photovoltaic Cells: Theory, Experiment, and Simulation. *J. Appl. Phys.* 93(6):3605–3614.
- [23] Wang, D. H., Moon, J. S., Seifert, J., Jo, J., Park, J. H., Park, O., and Heeger, A. J., 2011. Sequential Processing: Control of Nanomorphology in Bulk Heterojunction Solar Cells. *Nano Lett.* 11(8):3163–3168.
- [24] Gadisa, A., Svensson, M., Andersson, M. R., and Inganäs, O., 2004. Correlation Between Oxidation Potential and Open-Circuit Voltage of Composite Solar Cells Based on Blends of Polythiophenes/Fullerene Derivative. *Appl. Phys. Lett.* 84(9):1609–1611.

## CHAPTER 5

### Objective 2: Enhancement of Exciton Transportation and Carrier Diffusion in CuO Incorporated Polymer Solar Cells by Thermal Annealing

#### 5.1 Introduction

Bulk heterojunction (BHJ) PSCs benefit from a homogeneous donor-acceptor (D-A) contact interface compared to their inorganic counterpart. A homogenous D-A interface offers a longer free path for charge carriers, resulting in a longer diffusional pathway and a larger coulomb interaction between electrons and holes. This is triggered by the low dielectric constant of organic semiconductors. Among various conventional donor-acceptor structures, poly(3-hexylthiophene)/[6,6]-phenyl-C70-butyric acid methyl ester (P3HT/PCBM) mixture is highly encouraging due to the unique properties of P3HT [1-3]. P3HT molecules possess superior charge transport ability ( $1/10^4 - 1/10 \text{ cm}^2/\text{V s}$ ) and crystallinity in bulk state as well as expanded photo-absorption and environmental stability. Several researchers have attempted enhancing the PCE in polymer based solar cells by various approaches.

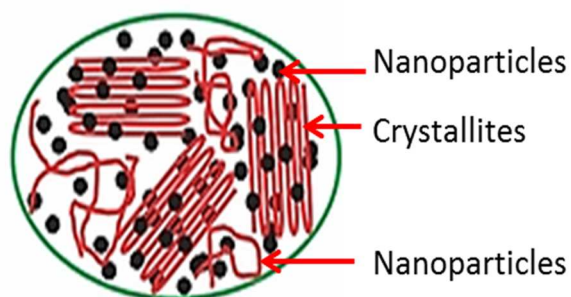


Figure 5.1: Schematic illustration of internal structure of thin films

These include the design of novel device structures, producing materials with short energy gap, morphological refining of polymer thin films, upgrading photo generation ability, and creation of higher electron-hole mobility by adjusting D-A contact surface [4–7]. To enhance the crystallinity and surface morphology in spun-casted polymer films, several strategies such as thermal/ solvent annealing [8–10] and using additives [11] have been used successfully.

The  $V_{oc}$  and  $J_{sc}$  mainly depend on the optimum morphology of the polymer film as it describes the energy level, band gap and the hole mobility of the conjugated polymer. The optimum morphology of P3HT/PCBM films describes two main features: 1) the molecular ordering within the donor or acceptor phase, which affects the photon absorption and carrier mobility; and 2) scale of phase separation between the donor and the acceptor, which can directly influence the exciton dissociation and charge transport and/or collection processes[12, 13]. Compared to inorganic solar cells, PSCs usually have insufficient light absorption due to the thin active layer which is restricted by the short exciton diffusion length and low carrier mobility. Optimization of the morphology by various treatments, such as thermal annealing which can lead to molecular rearrangement of the spin-coated films, helps to overcome these drawbacks and improves the power conversion efficiency. This in turn will increase light harvesting of P3HT:PCBM film and improve PCE. Motaung *et al.* [14] obtained 1.03% maximum PCE for ZnO incorporated P3HT: PCBM devices which were heat treated up to 140° C. Kang *et al.* [15] reported 3.86% PCE, 0.68V open-circuit voltage ( $V_{oc}$ ) and 64% fill factor (FF) through post-annealing at 170 °C. To improve the photon harvesting in PSCs, the incorporation of inorganic nanoparticles (INPs) has been extensively investigated. Nanoparticles (NPs); such as ZnO, TiO<sub>x</sub>, and CdSe can be successfully incorporated into P3HT: PCBM layers as electron acceptors [16]; whereas Au and Ag NPs [17] have been used to enhance the photon absorbance.



However, no conclusive work has been conducted to optimize the morphology of both metal oxides such as CuO nanoparticles incorporated PCBM/ P3HT thin films through annealing treatment. In this work, X-ray diffraction (XRD) and ultraviolet–visible spectroscopy (UV–vis) are used to identify the evolution of the structure morphology and optical properties of CuO NPs/P3HT/PCBM with thermal annealing. A schematic illustration of the structure of the photovoltaic devices which are fabricated for this study is shown in Figure 3.2 (a). The fabrication and characterization methods are described in sections 3.2.1 and 3.3 respectively.

## 5.2 Results and Discussion

### 5.2.1 Morphological Analysis

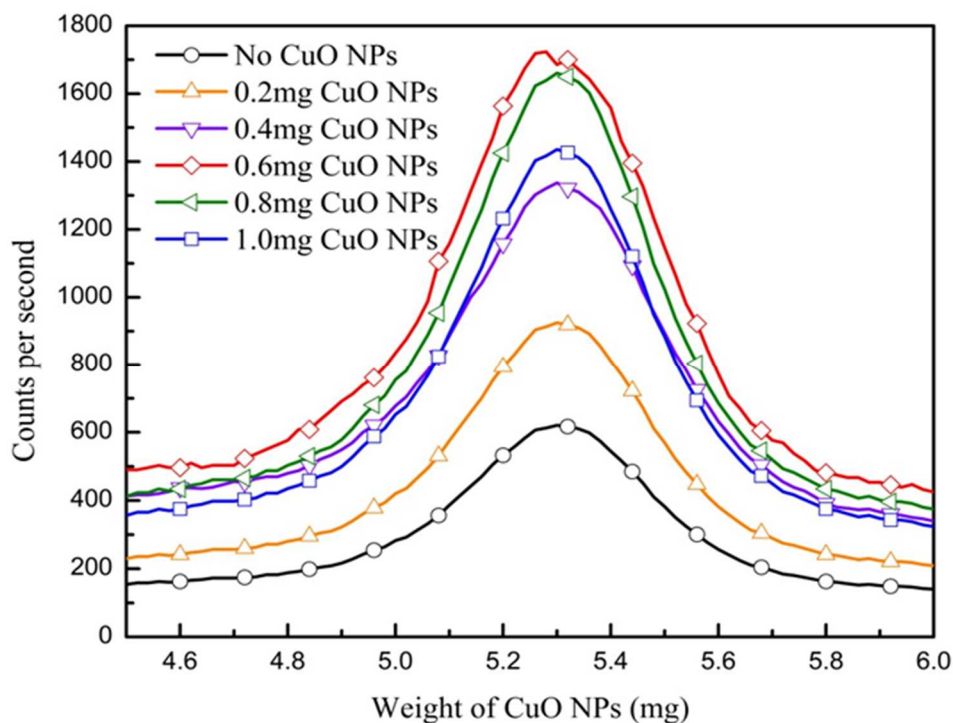


Figure 5.2: XRD spectra for CuO NPs incorporated P3HT/PCBM thin films after annealing

The XRD spectra were recorded from  $4^\circ$  to  $7^\circ$  at a rate of  $0.2^\circ$  per min by using automatic slits. Figure 5.2 shows the XRD spectra for PSC samples which were annealed for 30 min at  $150^\circ\text{C}$  in vacuum. The annealing temperature and time interval were chosen based on the results reported by Algazzar *et. al.* that correspond to the optimum PCE of P3HT:PC70BM [18].

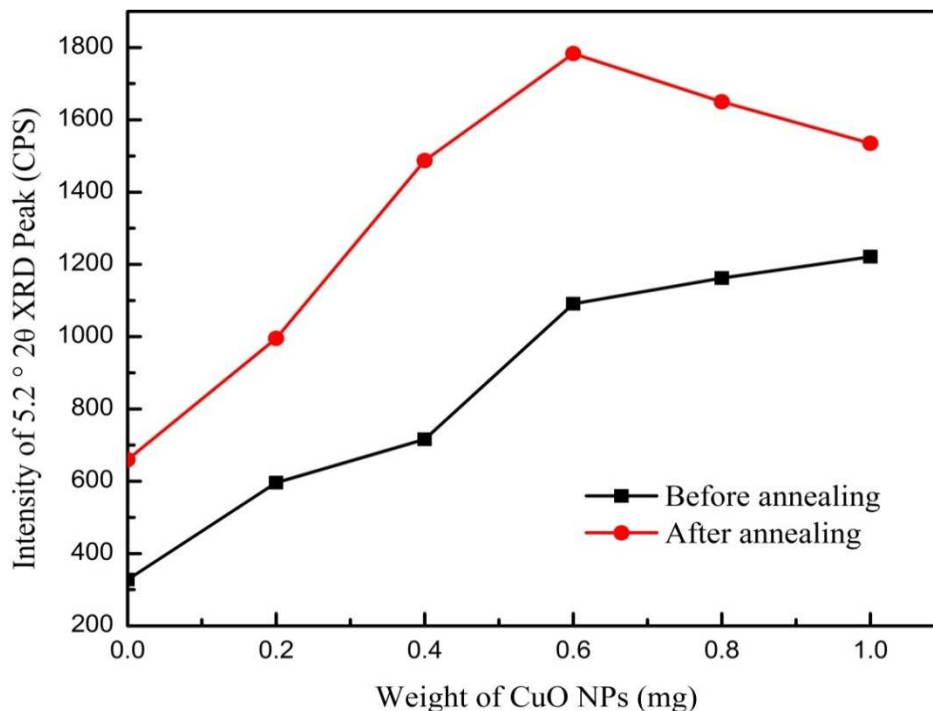


Figure 5.3: Diffraction peak intensity before and after annealing

Annealing treatment increases the intensity and width of the diffraction peaks of hybrid solar cells with different amounts of CuO NPs, as shown in Figure 5.3. The increase in crystallinity of P3HT may be attributed to its enhanced self-organization ability due to annealing in the presence of CuO NPs. However, diffraction peaks relevant to the PC70BM were not noticeable in the XRD spectra of P3HT:PC70BM films, both with and without CuO NPs. Therefore, it is predicted that the addition of CuO NPs and annealing only affect the

crystallization of P3HT with little or no influence on the crystallization of PC70BM. It is evident from previous research that PCBM is not a crystalline material [19]. The samples which contained 0.6mg of CuO NPs exhibited the highest crystallinity among the heat-treated samples. Further increase in the amount of CuO NPs above 0.6mg led to a decline in crystallinity which may be attributed to uncontrolled phase separation, interruption in P3HT crystallization and/or agglomeration and insufficient dissolving of CuO nanoparticles [20].

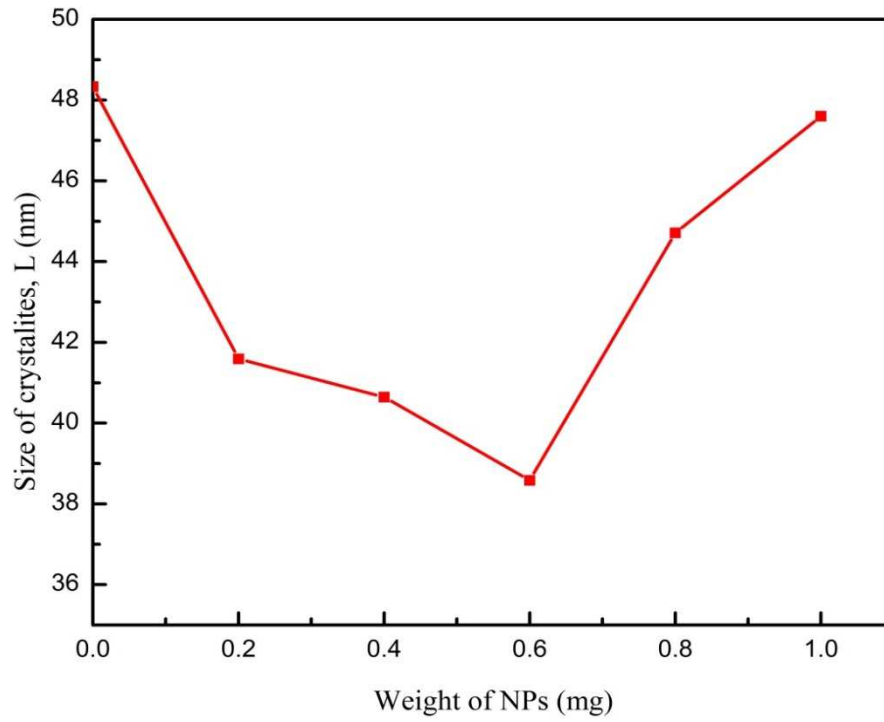


Figure 5.4: Effect of CuO NPs on crystallite size ( $L$ ) after thermal annealing

The crystallite size ( $L$ ) was calculated using the values obtained from XRD results using the Scherer's equation [21],

$$L \text{ (nm)} = \frac{0.9\lambda}{\Delta_{2\theta} \cdot \cos\theta} \quad (5.1)$$

Where  $\lambda$  is Cu K- $\alpha$  wavelength (0.154 nm),  $\Delta_{2\theta}$  is the full width half maximum of the peak, and  $\theta$  is half the angle at peak.

The higher XRD peaks indicate that more P3HT crystallites have been formed; i.e. higher crystallinity. However, these crystallites are higher in numbers but the crystallite size has decreased with increased amounts of CuO NPs as shown in Figure 5.4. Crystallite size calculations for annealed samples show that 0.6 mg of CuO NPs samples exhibit the smallest crystallite size of 38.58 nm. A smaller crystallite introduces a shorter exciton diffusion path between P3HT backbones which helps in obtaining a higher short circuit current ( $J_{sc}$ ) of the devices [22].

The effect of annealing treatment on the crystallinity of P3HT:PC70BM thin films were further analyzed by Differential Scanning Calorimetry (DSC) to corroborate the XRD results. The percentage crystallinity ( $X_c$ ) of P3HT in the P3HT:PC70BM: CuO NPs active layer was calculated using the DSC melting and crystallization enthalpies by the Equation 4.9.

The crystallinity values calculated by DSC show that the percent crystallinity, in general, increases gradually as the amount of CuO NPs increases in the P3HT:PC70BM polymer blend, before annealing. However, after annealing, the percent crystallinity has remarkably increased as comparatively shown in Figure 5.5. This behavior may be attributed to phase separation and recrystallization of P3HT as single molecules. The percent crystallinity values of the annealed samples began to decline when the amount of CuO NPs is higher than 0.6mg. This may be attributed to agglomeration and polymer entanglement with excess amounts of CuO NPs during the annealing process, or to uncontrolled phase separation and interruption in P3HT crystallization.

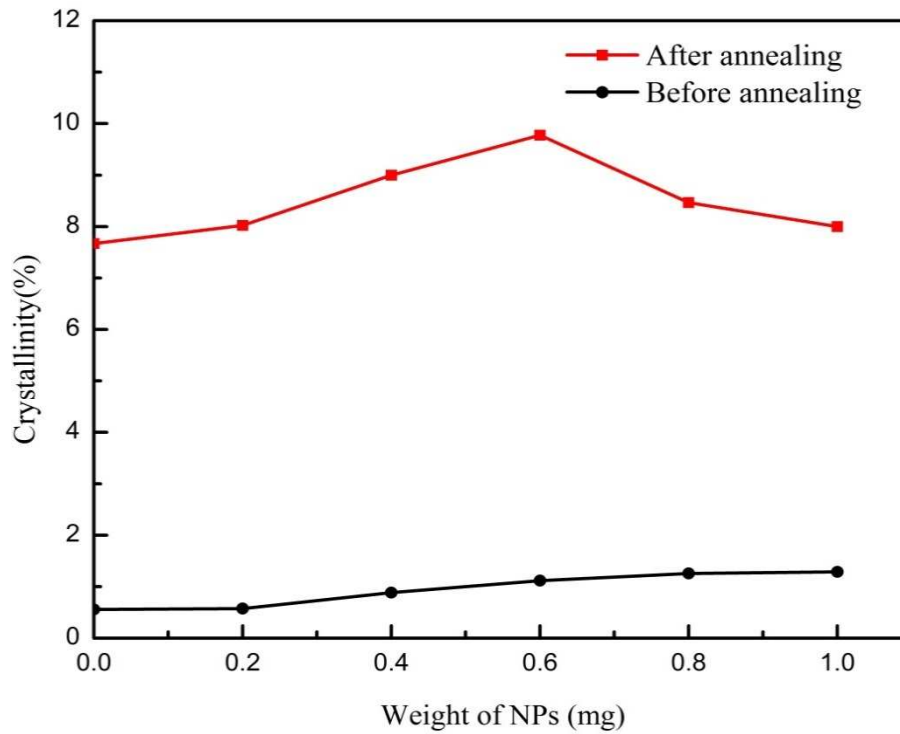


Figure 5.5: Percent crystallinity before and after annealing

The crystallization results obtained from DSC are in line with the ones obtained from XRD. Both of these methods showed a gradual and consistent increase in crystallinity before annealing as a function of CuO NPs addition. Similarly, an increase in crystallinity was observed in the samples after annealing; the crystallinity peaked in samples containing 0.6 mg CuO NPs.

The AFM surface images of P3HT:PC70BM films with different amounts of CuO NPs, after thermal annealing, are shown in Figures 5.6. Surface topographical analysis of the polymer films was carried out in AC-AFM non-contact mode with an I-gain of 10, set point of 1.24 and a scan size of 2x2  $\mu\text{m}$ . In comparison, the samples prepared with thermal annealing showed a relatively higher surface roughness than those without annealing as illustrated in Figure 4.15. The root-mean-square roughness ( $\sigma_{rms}$ ) of the annealed samples increased from 0.41 nm in the thin film without CuO NPs up to 0.99 nm in the thin film with 1mg of CuO NPs. The heat treated

cells with the optimum composition of 0.6mg of CuO NPs exhibited a surface roughness  $\sigma_{rms}$  of 0.82 nm. In low crystalline polymer blends, the roughness has been found to be linearly related to the crystallinity and the rate of cooling and roughness seem to influence the crystallite formation [23-25]. This indicates that the increase in roughness due to annealing influences the formation of crystallites and increases the crystallinity.

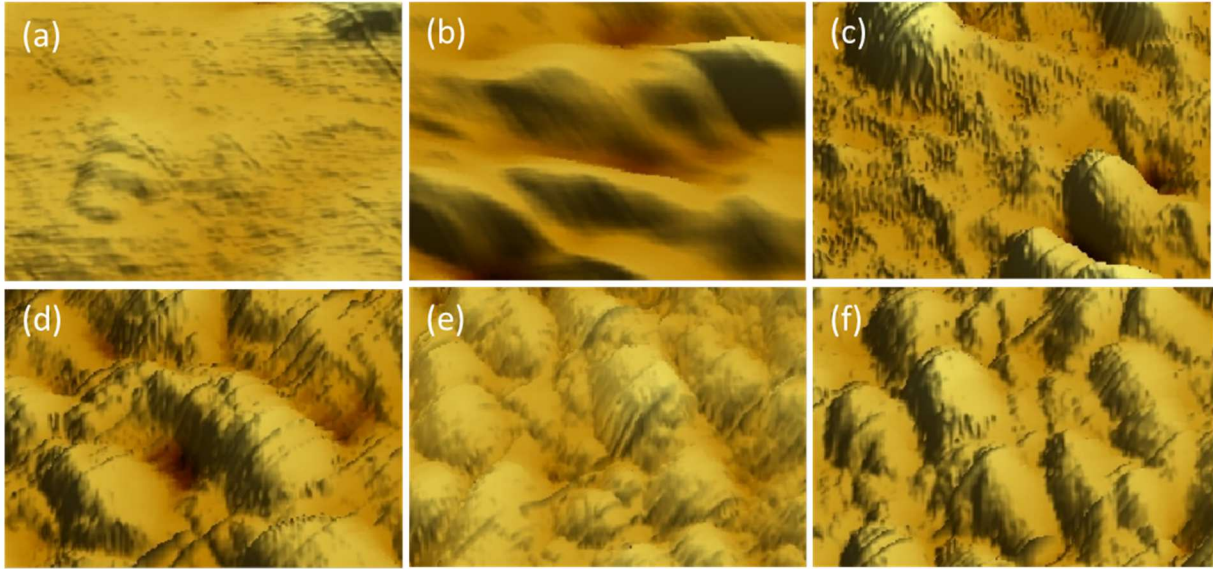


Figure 5.6: AFM images for annealed P3HT/PCBM layers with (a) No CuO NPs, (b) 0.2mg CuO NPs, (c) 0.4mg CuO NPs, (d) 0.6mg CuO NPs, (e) 0.8mg CuO NPs, (f) 1mg CuO NPs

Table 5.1 summarizes the roughness values of all the samples determined by AFM. The roughness of the heat treated cells in general has doubled. The increase in roughness can be attributed to increased nano-scale phase separation between the crystalline P3HT and the PC70BM acceptor with thermal annealing. Furthermore; the increase in surface roughness leads to an increase in interfacial contact area between the PEDOT: PSS and P3HT/PCBM/CuO NPs

layer, allowing more efficient hole collection at the anode and thereby improving  $J_{sc}$  and fill factor (FF) of the PSCs.

Table 5.1: Comparison of roughness values of the PSCs before and after annealing

CuO NPs (mg)	Roughness (nm)	
	Before Annealing	After Annealing
0	0.11	0.34
0.2	0.20	0.42
0.4	0.26	0.67
0.6	0.31	0.82
0.8	0.39	0.87
1.0	0.47	0.99

### 5.2.2 Optical and Electrical Properties

The UV–Vis absorption spectra of the P3HT/PC70BM/CuO NPs blend films before and after annealing were compared to determine the effect of annealing on the optical properties of the PSCs. The absorption intensities clearly improved in all the cells containing CuO NPs in the P3HT/PC70BM thin films after annealing, as shown in Figure 5.8.

The increase in absorption intensities is attributed to enhanced crystallinity of P3HT by annealing treatment, combined with improved optical absorption caused by CuO NPs in the polymer active layer, irrespective of thermal annealing. This was confirmed by recording the UV-Vis spectra of the CuO NPs thin films on a glass substrate.

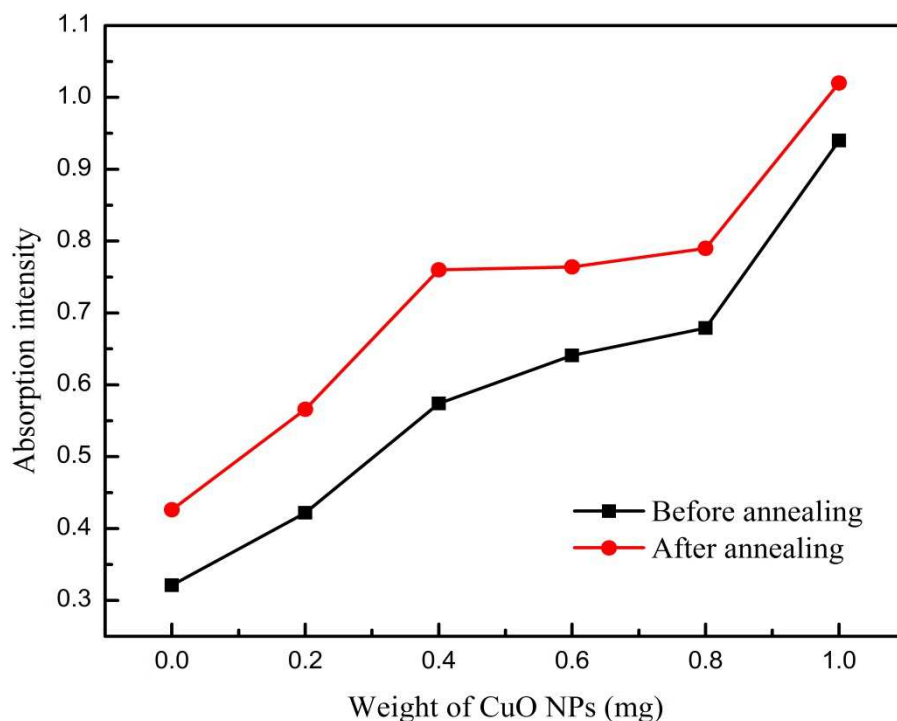


Figure 5.8: Optical absorption intensities from UV-vis spectroscopy before and after annealing

The maximum light absorption values of the CuO NPs thin films and the P3HT/PCBM/CuO NPs thin films before and after annealing are compared in Table 5.2. Based on the values shown in the table, it looks like annealing does not affect the light absorption of CuO NPs. However, increasing the amount of CuO NPs in the P3HT/PCBM films seems to improve the light absorption of the un-annealed polymer blend significantly. On the other hand, the light absorption of the P3HT/PCBM/CuO NPs films seems to improve significantly after annealing. This indicates that the increased crystallinity of the P3HT/PCBM blend after annealing also plays an important role in improving the light absorption in comparison to the CuO NPs in annealed samples. These results lead to the conclusion that both the CuO NPs and the morphology of the P3HT/PCBM blend play a significant role in enhancing the light absorption and the optical properties of the active layer before and after annealing respectively.



Table 5.2: Comparison of maximum light absorption intensities of the CuO NPs and the P3HT/PCBM/CuO NPs active layer before and after annealing

CuO NPs (mg)	CuO thin film	Annealed	P3HT/PCBM/CuO thin film	Annealed P3HT/PCBM/CuO thin film
0	n/a	n/a	0.36	0.42
0.2	0.36	0.37	0.42	0.56
0.4	0.49	0.48	0.57	0.76
0.6	0.54	0.54	0.64	0.76
0.8	0.65	0.66	0.68	0.79
1.0	0.77	0.79	0.94	1.02

The absorption spectra, shown in Figure 5.7, shows the main peaks at 450–500 nm and two shoulder peaks at 600 and 635 nm. According to literature, the main peak and the vibronic shoulders are generated by P3HT in the active layer [26].

However, the shoulder signal was distinguishably observed with increasing amounts of CuO NPs in the P3HT: PCBM blend. Other researchers have shown that the first shoulder signal at wavelengths higher than 500 nm and second shoulder signal at 650 nm correspond to the absorption of extended conjugation of solid state P3HT in the layer and the inter-chain stacking of P3HT, respectively [27]. The photon absorption coefficient describes the photon absorption capacity of the thin films. The optical absorption coefficient, band gap and the thickness of the photoactive layer are the major determinants of photon absorption yield. In hybrid solar cells, absorption was enhanced by incorporating CuO NPs and improving crystallinity of P3HT in the

thin film structure. This serves as the most promising approach for increasing the  $J_{sc}$  of a hybrid device [28, 29].

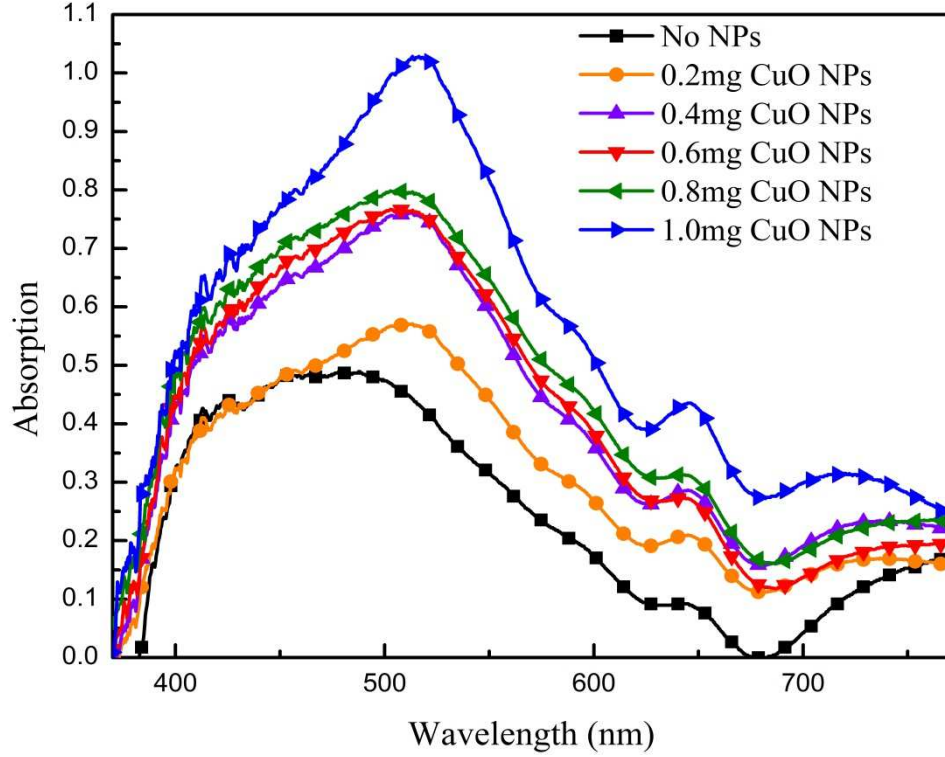


Figure 5.7: Optical absorption spectra after annealing

The highest EQE measurements for annealed and non-annealed solar cells with various amounts of CuO NPs are comparatively shown in Figure 5.9. The EQE increased over a broad wavelength ranging from 300 to 620 nm after incorporating CuO NPs in the active layer. However, after annealing maximum EQE values increased in all the devices to 70, 61, 61, 57, 52 and 49%; respectively.

The improvement of EQE can be attributed to the increased hole and electron polaron motilities, charge collection at the electrodes, and photon absorption. The results from EQE concur with the results obtained from UV-Vis absorption. It is clear that the absorption of

P3HT:PC70BM cells in the range of 420 nm to 550 nm is enhanced after annealing as well as by incorporating CuO NPs in the active layer. This indicates that higher amounts of CuO NPs lead to more absorption and higher EQE of the cell; i.e. higher electron mobility, photo generated carrier injections and better J-V characteristics. The EQE spectra and UV-vis absorption spectra clearly illustrate that the annealed P3HT:PC70BM thin films with CuO NPs show significant improvements in electrical performance compared to the reference cells.

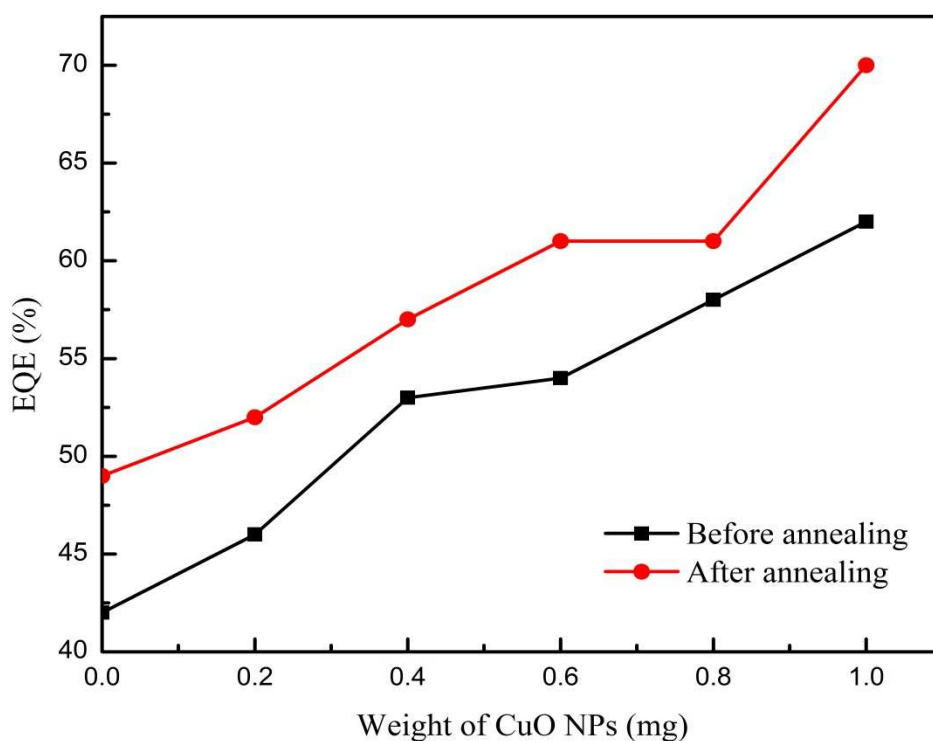


Figure 5.9: Effect of annealing on the EQE values of PSCs with CuO NPs

The short-circuit current density ( $J_{sc}$ ), open-circuit voltage ( $V_{oc}$ ), fill factor and power conversion efficiency (PCE) of all the cells before and after annealing are listed in Table 5.3. These parameters are slightly improved by annealing treatment at 150° C above the glass transition temperature. According to the J-V characteristics of the devices without annealing, the

short circuit current of the reference cell was found to be 5.234 mA/cm<sup>2</sup> and it seemed to increase to 6.484 mA/cm<sup>2</sup> in cells containing 0.6 mg of CuO NPs which accounts for a 24% increase. The current gain gives a rise to the power conversion efficiency (PCE) from 2.106% to 2.963%; in addition the fill factor increases from 61.15% to 68.0% with 11.2% enhancement.

Table 5.3: Performance parameters of P3HT/PCBM/CuO-NPs hybrid solar cells before and after annealing (B/A: before annealing, A/A: after annealing)

CuO NPs (mg)	J <sub>sc</sub> (mA/cm <sup>2</sup> )		V <sub>oc</sub> (V)		FF (%)		PCE (%)	
	B/A	A/A	B/A	A/A	B/A	A/A	B/A	A/A
0	5.234	6.252	0.658	0.678	61.15	66.14	2.106	2.804
0.2	5.726	6.907	0.675	0.659	66.52	66.52	2.571	3.028
0.4	5.993	7.948	0.670	0.651	66.21	66.21	2.632	3.426
0.6	6.484	9.149	0.673	0.610	68.00	66.31	2.963	3.701
0.8	6.320	8.776	0.668	0.602	68.50	67.10	2.895	3.545
1.0	6.122	8.264	0.674	0.597	66.84	66.84	2.758	3.298

However, after the annealing process,  $V_{oc}$  decreased with increasing the amount of CuO NPs; whereas  $J_{sc}$  increased from 6.252 to 9.149 mA/cm<sup>2</sup> with 46.3% enhancement, and FF remained almost the same. As a result, PCE increased from 2.804% to 3.701%, leading to a 32% enhancement in the cells containing 0.6 mg of CuO nanoparticles. This can be attributed to the increase in  $J_{sc}$ . Based on power conversion efficiency equation ( $PCE = V_{oc} * J_{sc} * FF / \text{total incident power density}$ ),  $V_{oc}$ ,  $J_{sc}$ , and FF are crucial factors in final PCE. Higher  $V_{oc}$ ,  $J_{sc}$ , and FF result in higher PCE. The PCE values obtained of the CuO NPs incorporated solar cells before and after annealing are shown in Figure 5.10.

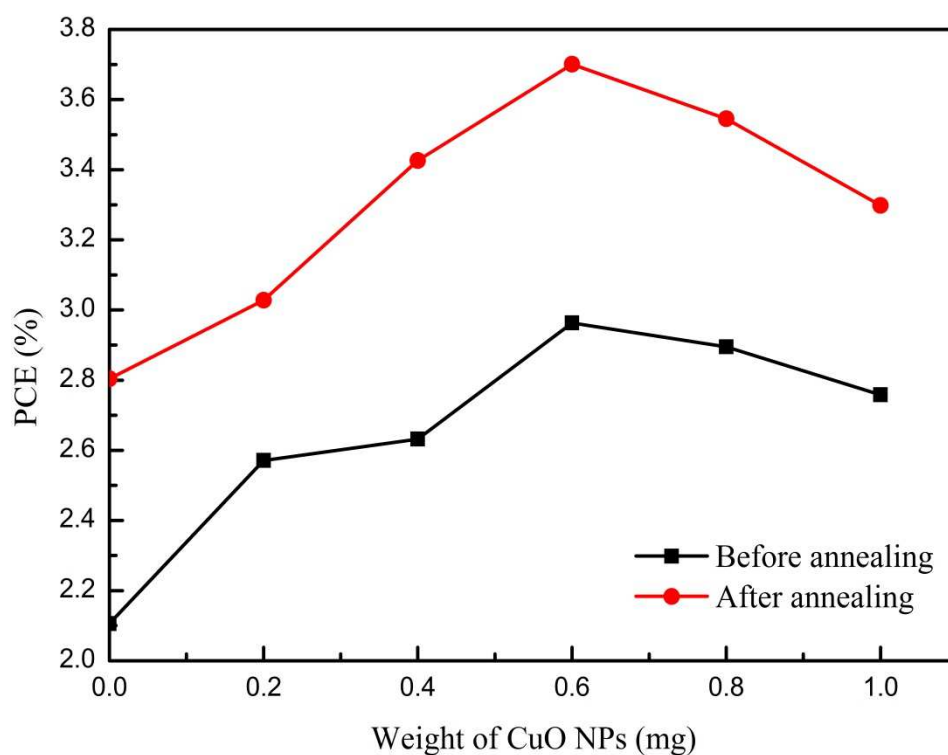


Figure 5.10: PCE of P3HT/PCBM/CuO-NPs hybrid solar cells before and after annealing

As illustrated in Figure 5.10, the maximum efficiency of 2.963% was observed in samples containing 0.6 mg CuO before annealing. The efficiency values increased after annealing to 3.702% in the optimum cell which contains 0.6mg of CuO NPs. The increase in PCE at weight fractions of CuO NPs up to 0.6mg indicates the lowering of the number of recombination charges before reaching the electrode and the increase in the optical absorption by the thin film. At higher amounts of CuO NPs ( $>0.6\text{mg}$ ), the efficiency starts to decline, which is an indication of charge recombining and less charge phase separation.

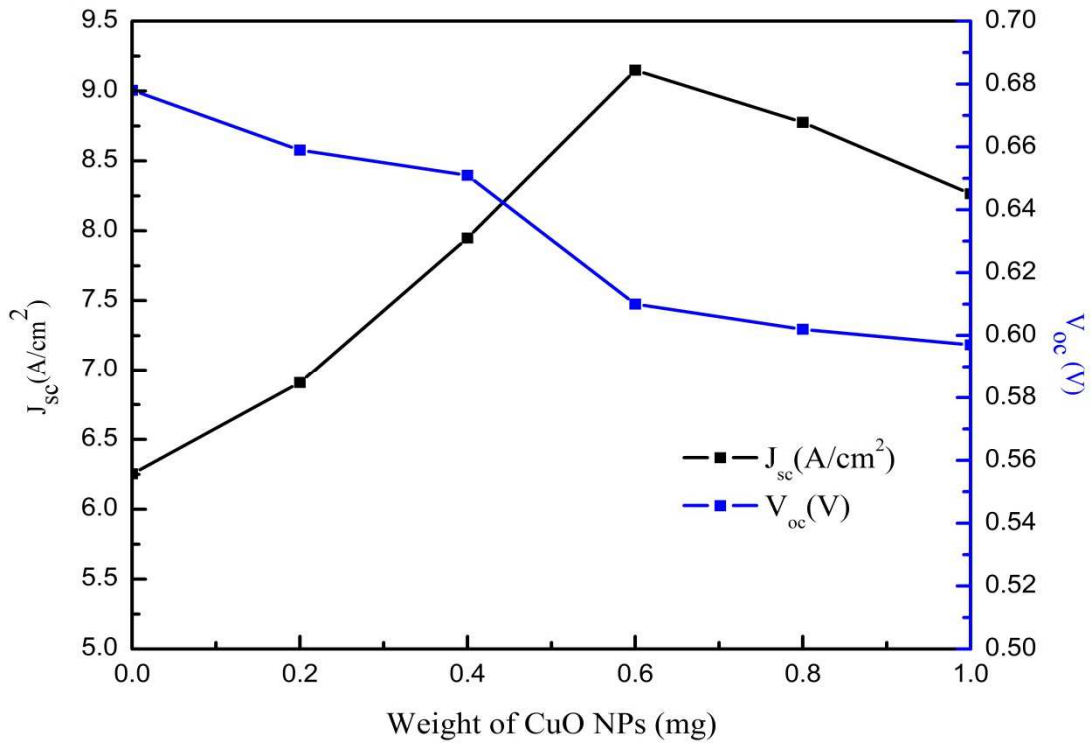


Figure 5.11:  $J_{sc}$  and  $V_{oc}$  of P3HT/PCBM/CuO-NPs hybrid solar cells after annealing

For the annealed devices,  $V_{oc}$  and  $J_{sc}$  were measured at the intersections of the J–V curve with the x-axis and the y-axis; respectively, as shown in Figure 5.11. The open circuit voltage ( $V_{oc}$ ) is controlled by the energetic relationship between the donor and the acceptor. The energy difference between the highest occupied molecular orbit (HOMO) of the donor and the lowest unoccupied molecular orbit (LUMO) of the acceptor is known to most closely and linearly correlate with the  $V_{oc}$  [29]. Therefore, controlling the energy levels is important to increase the power conversion efficiency [29]. The linear correlation of the  $V_{oc}$  to the energetic gap between donor's HOMO level and acceptor's LUMO level can be shown as Equation 5.2 [30].

$$V_{oc} = E_{g,D/A} = E_{g,D} - (LUMO_D - LUMO_A) \quad (5.2)$$

The annealing treatment for the CuO NPs incorporated thin films has significantly decreased the value of  $V_{oc}$  for the PSCs possibly since the CuO NPs in the annealed thin films changed the active layer P3HT conjugation length. As a result, the HOMO energy level of P3HT has decreased.

The short circuit current ( $J_{sc}$ ) of the annealed samples has increased. This could be due to higher crystallinity and smaller crystallite size leading to better electron mobility. The annealing treatment of P3HT near the glass transition rearranges the molecular ordering of the internal microstructure. This leads to an increase in the extent of carrier diffusion of P3HT polymer across the PCBM phase, thus improving  $J_{sc}$  in the photovoltaic performance. The fill factor (FF) remained nearly the same after annealing, which indicates that the annealing treatment has a very small effect on FF, but it influences both the  $J_{sc}$  and  $V_{oc}$ .

### 5.3 Conclusions

In this work, CuO NPs was added to P3HT/PC70BM polymer blend to improve the crystallinity of P3HT and to enhance the P3HT/PC70BM phase separation. UV-Vis and EQE analysis showed enhancement of self-organization ability, which led to improved P3HT crystallinity and intensified phase separation of P3HT/PC70BM in polymer films. EQE of the solar cells increased due to increased hole and electron polaron mobilities in cells with CuO NPs. AFM analysis showed an increase in surface roughness of the cells with CuO NPs, which is an indication of larger space for P3HT crystallites to form. Higher P3HT crystallinity reduces the amount of PCBM dissolved in the amorphous regions of P3HT, thus promoting the aggregation of PC70BM, which contributes to PC70BM/P3HT phase separation. Adding 0.6 mg of CuO NPs to the active layer resulted in forming the smallest polymer crystallites, which was nearly 38.58

nm after annealing at 150°C for 30 min in vacuum. The smaller crystallite size suggests a shorter path of the charge carriers between P3HT backbones, which increased the short circuit current ( $J_{sc}$ ) and increased the open circuit voltage ( $V_{oc}$ ) in the solar cells. At the optimum annealing conditions of 150 °C for 30 minutes, CuO NPs incorporated P3HT/PC70BM solar cells yielded 32% improvement in PCE due to increased photo absorption with elevated exciton generation rate, enhanced hole electron mobility and charges transport due to improved crystallinity.



## References

- [1] Shen, W., Tang, J., Yang, R., Cong, H., Bao, X., Wang, Y., Wang, X., Huang, Z., Liu, J., Huang, L., Jiao, J., Xu, Q., Chenb, W., and Belfiore, L. A., 2014. Enhanced efficiency of polymer solar cells by incorporated Ag-SiO<sub>2</sub> core-shell nanoparticles in the active layer. *RSC Advances*. 4:4379-4386.
- [2] Konkin, A., Bounioux, C., Ritter, U., Scharff, P., Katz, E.A., Aganov, A., Gobsch, G., Hoppec, H., Ecke, G., Roth, H.K., 2011. ESR and LESR X-band study of morphology and charge carrier interaction in blended P3HT-SWCNT and P3HT-PCBM-SWCNT solid thin films. *Synthetic Metals*. 161:2241-2248.
- [3] Wanninayake, A., Gunashekar, S., Li S. et al., 2015. Performance enhancement of polymer solar cells using copper oxide nanoparticles. *Semicond. Sci. Technol.* 30: 064004.
- [4] Wicklein, A., Ghosh, S., Sommer, M., Wurthner, F., Thelakkat, M., Self-Assembly of Semiconductor Organogelator Nanowires for Photoinduced Charge Separation. *ACS Nano* 3 (5):1107-1114. Jorgensen, M., Norrman, K., Krebs, F.C., 2008. Stability/degradation of polymer solar cells. *Sol. Energ. Mat. Sol. Cells*. 92: 686-714.
- [5] Wu, Z., Song, T., Xia, Z., Wei, H., and Sun, B., 2013. Enhanced performance of polymer solar cell with ZnO nanoparticle electron transporting layer passivated by in situ cross-linked three-dimensional polymer network. *Nanotechnology*. 24: 484012.
- [6] Padinger, F., Rittberger, R.S., Sariciftci, N.S., 2003. Effects of Postproduction Treatment on Plastic Solar Cells. *Adv. Funct. Mater.* 13: 85-88.
- [7] Lee, W.H., Chuang, S.Y., Chen, H.L., Su, W.F., and Lin, C.H., 2010. Exploiting optical properties of P3HT: PCBM films for organic solar cells with semitransparent anode. *Thin Solid Films*. 518: 7450-7454.
- [8] Kim, Y., Choulis, S.A., Nelson, J., Bradley, D.D.C., Cook, S., Durrant, J.R., 2005. Composition and annealing effects in polythiophene/fullerene solar cells. *J. Mater. Sci.* 40: 1371-1376.
- [9] Li, G., Yao, Y., Yang, H., Shrotriya, V., Yang, G., Yang, Y., 2007. Solvent Annealing Effect in Polymer Solar Cells Based on Poly (3-hexylthiophene) and Methanofullerenes. *Adv. Funct. Mater.* 17: 1636-1644.
- [10] Salim, T., Wong, L.H., Brauer, B., Kukreja, R., Foo, Y. L., Bao, Z., Lam, Y. M., 2011. Solvent additives and their effects on blend morphologies of bulk heterojunctions. *J. Mater. Chem.* 21: 242-250.
- [11] Konkin, A., Bounioux, C., Ritter, U., Scharff, P., Katz, E. A., Aganov, A., Gobsch, G., Hoppec, H., Ecke, G., and Roth, H. K., 2011. ESR and LESR X-band study of morphology and charge carrier interaction in blended P3HT-SWCNT and P3HT-PCBM-SWCNT solid thin films. *Synthetic Met.* 161: 2241-8.

- [12] Jin, S., Naidu, B. V. K., Jeon, H., Park, S., Park, J., Kim, S. C., Lee, J. W., and Gal, Y., 2007. Optimization of process parameters for high-efficiency polymer photovoltaic devices based on P3HT: PCBM system. *Sol. Energy Mater. Sol. Cells*. 91: 1187–1193.
- [13] Motaung, D. E., Malgas, G. F., Ray, S. S., Arendse, C. J., 2013. Annealing effect of hybrid solar cells based on poly (3-hexylthiophene) and zinc-oxide nanostructures. *Thin Solid Films*. 537: 90-96.
- [14] Kang, R., Oh, S., Na, S., Kim, T. S., Kim, D. Y., 2014. Investigation into the effect of post-annealing on inverted polymer solar cells. *Sol. Energ. Mat. Sol. Cells*. 120; 131-135.
- [15] Beek, W. J. E., Wienk, M. M., and Janssen R. A. J., 2004. Efficient hybrid solar cells from zinc oxide nanoparticles and a conjugated polymer. *Adv. Mater.* 16: 1009–1013.
- [16] Liao, H., et al. 2012. Nanoparticle-tuned self-organization of a bulk heterojunction hybrid solar cell with enhanced performance. *ACS Nano*. 6: 1657–1666.
- [17] Abu-Zahra, N., and Algazzar, M., 2013. Effect of Crystallinity on the Performance of P3HT/PC70BM/n-Dodecylthiol Polymer Solar Cells. *J. Sol. Energy Eng.* 136(2):021023.
- [18] Erb, T., Zhokhavets, U., Gobsch, G., Raleva, S., Stuhn, B., Schilinsky, P., 2005. Correlation between structural and optical properties of composite polymer/ fullerene films for organic solar cells. *Adv. Funct. Mater.* 15: 1193.
- [19] Heo, S.W., Song, K.W., Choi, M.H., Oh, H.S., and Moon, D.K., 2013. Influence of alkanediol series as processing additives in photo-active layer on the power conversion efficiency of polymer solar cells. *Sol. Energ. Mat. Sol. C*. 114: 82–88.
- [20] Cullity, B. D., and Stock, S. R., 2001. Elements of X-Ray Diffraction, 3rd ed. Prentice Hall, London, UK.
- [21] Bundgaard, E., and Krebs, F. C., 2007. Low Band Gap Polymers for Organic Photovoltaics. *Sol. Energy Mater. Sol. Cells*. 91(11): 954–985.
- [22] Kim, W., and Kang, H., 1998. The effects of transesterification on the properties of PEN/PET blend films, SPE/ANTEC 1998 proceedings, pp 1561–1564, CRC press, London, U.K.
- [23] Gomez, E.D., Barteau, K.P., Wang, H., Toney, M.F., and Loo, Y., 2005. Correlating the scattered intensities of P3HT and PCBM to the current densities of polymer solar cells. *Chem. Comm.* 47: 436–438.
- [24] Atwater, H. A., and Polman, A., 2010. Plasmonics for improved photovoltaic devices. *Nature Materials*. 9: 205-213.
- [25] Schuller, J. A., Barnard, E. S., et al. 2010. Plasmonics for extreme light concentration and manipulation. *Nature Materials* 9: 193-204.

- [26] Krebs F.C., Thomann, Y., Thomann, R., and Andreasen, J.W., 2008. A simple nanostructured polymer/ZnO hybrid solar cell-preparation and operation in air. *Nanotechnology* 19: 424013.
- [27] De Freitas, J.N. Korala, L. Reynolds, L.X. Haque, S.A. 2012. Connecting the (quantum) dots: Towards hybrid photovoltaic devices based on chalcogenide gels. *Phys. Chem. Chem. Phys.* 14:15180–15184.
- [28] Bundgaard, E., Shaheen, S.E., Krebs, F.C., Ginley, D.S., 2007. Bulk heterojunctions based on a low band gap copolymer of thiophene and benzothiadiazole. *Sol. Energ. Mat. Sol. C.* 91: 1631–1637.
- [29] Lu, L., Luo, Z., Xu, T., and Yu, L., 2013. Cooperative plasmonic effect of Ag and Au nanoparticles on enhancing performance of polymer solar cells. *Nano Letters*. 13(1): 59-64.

## CHAPTER 6

### Objective 3: Improvement of Exciton Dissociation and Electron Mobility in Polymer Solar Cells Using ZnO NPs

#### 6.1 Introduction

ZnO, as a semiconductor, has attracted much attention due to its unique properties; such as high electron mobility, wide and direct band gap and large exciton binding energy. Therefore, ZnO has been considered a promising material for optoelectronic device applications.

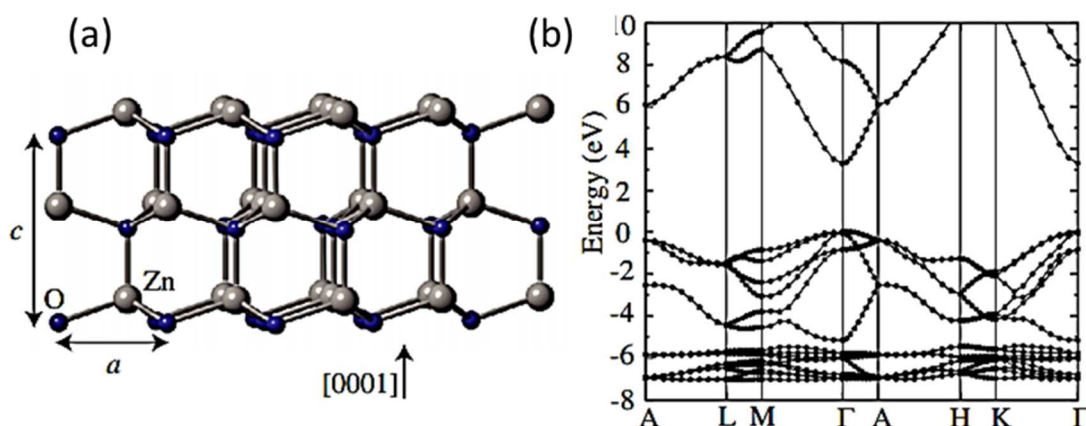


Figure 6.1: (a) The wurtzite crystal structure of ZnO with the lattice parameters  $a$  and  $c$  indicated and (b) the calculated band structure of ZnO using the HSE hybrid functional

ZnO is an n-type semiconductor which has wide band gap energy of 3.37 eV. It is well-known that the unintentional n-type conductivity in ZnO is caused by the presence of oxygen vacancies or zinc interstitials. Since the defects have huge effects on doping, minority carrier lifetime and luminescence efficiency, the control of defects and, therefore, the associated charge carriers are very important for the properties of ZnO materials. There are a number of intrinsic

defects in ZnO with different ionization energies: O vacancy ( $V_O$ ), Zn vacancy ( $V_{Zn}$ ), Zn interstitial ( $Zn_i$ ), O interstitial ( $O_i$ ) and antisite Zn ( $Zn_O$ ). Zn interstitials and oxygen vacancies are the predominant ionic defect types in ZnO [1, 2].

Recently, many different organic donor materials have been investigated [3-5] while electron acceptors remain the bottleneck in these studies. The power conversion efficiency (PCE) of PSCs with [6, 6]-phenyl-C61-butyric acid methyl ester (PCBM) electron acceptors has reached up to 9%. However, there are some critical drawbacks with complex processing methods and oxidation of the acceptors in ambient conditions [6, 7]. Considering their stability under ambient conditions and high electron mobility, inorganic nanomaterials such as ZnO, CdSe and  $TiO_2$  are among the most suitable electron acceptors to incorporate with the polymer donor in hybrid solar cells [8-10]. Among these nanomaterials ZnO, a low temperature crystalline material, is one of the most promising electron acceptors for solar cells. The power conversion efficiency (PCE) of OSCs has been investigated through multidisciplinary attempts including designing new device structures, applying low band gap materials, and carefully controlling the morphology of the donor-acceptor molecular structure [11]. Optimization of the nanomorphology of the inorganic thin films remarkably improves their optical and electronic properties. Thermal annealing techniques are widely used in organic, as well as inorganic, thin film solar cells to enhance their electrical and optical properties by enhancing crystallinity, reducing defects, and roughening the crystalline phases in the thin films [12-14].

Several studies were conducted to understand the role of ZnO as an electron transport layer embedded in PSCs. Sekine *et al.* [15] reported 4% PCE with 25% improvement for PSCs with ZnO electron accepting layer while Oh *et al.* [16] reported 3.39% PCE for ZnO nanoparticles (NPs) doped poly (3-hexylthiophene)/ [6, 6]-phenyl-C61-butyric acid methyl ester/

(P3HT/PCBM) PSCs. P3HT/PCBM devices with ZnO nanoparticles, as an electron transporting layer, exhibited an improved power conversion efficiencies up to 3.26% [17]. Zhu *et al.* [18] obtained a 3.5% maximum PCE for PSCs with 15 nm diameter ZnO NPs incorporated in a buffer layer. Gao *et al.* [19] improved the PCE of PSCs from 3.03% to 3.84% via hydrogen treatment of ZnO electron transport layers.

As discussed in chapter 4 and chapter 5, CuO NPs were successfully incorporated in the P3HT/PCBM active layer as a donor candidate. The combined effect of the P3HT and CuO NPs enhanced the optical absorption and exciton generation rate leading to better donor properties in the active layer. CuO is a p-type semiconductor with band gap energy of 1.5 eV, which is close to the ideal energy gap of 1.4 eV, and ZnO is an n-type semiconductor which has wide band gap energy of 3.37 eV. Kidowaki *et al.* revealed the suitability of CuO/ZnO hetero-structure for solar cells [20, 21].

The first part of this study demonstrates the enhancement of power conversion efficiency of PSCs containing CuO NPs incorporated in P3HT/ PC70BM film with a ZnO-NPs buffer layer. The second part is focused on the enhancement of power conversion efficiency of CuO NPs incorporated P3HT/PC70BM PSCs containing a ZnO-NPs buffer layer with thermal annealing treatment. The combined effect of CuO and ZnO-NPs was studied by UV–visible analysis, current voltage (J–V) characteristics, atomic force microscopy, and EQE measurements. In addition, the electrical performance of the hybrid solar devices is presented in this work.

## 6.2 Results and Discussion

### 6.2.1 Electrical and Optical Performance

The architecture of the energy levels and layer structure of hybrid solar cell devices is schematically shown in Figure 6.2(a) and Figure 6.2(b) respectively [22]. The highest occupied molecular orbital (HOMO) and lowest unoccupied molecular orbital (LUMO) energy bands of P3HT are formed at  $-5.2$  eV and  $-3.53$  eV; respectively. Similarly, in the PCBM molecules, the HOMO and LUMO levels are formed at  $-6.3$  eV and  $-3.9$  eV; respectively [23]. The conduction band (CB) of the ZnO NPs aligns at  $-4.1$  eV while the LUMO level of the PEDOT: PSS forms at  $-5.0$  eV [24]. The energy difference between valence band (VB) and conduction band (CB) of the CuO NPs is found to be  $2.14$  eV. Hence, the P3HT combined with CuO NPs forms a strong donor phase, which can produce more excitons (electron-hole pairs) into the structure. These donor materials and PC70BM acceptor molecules create a donor-acceptor (D/A) heterojunction, which can dissociate the excitons generated in the donor structure [25].

The energy gradient highest occupied molecular orbital (HOMO) of P3HT ( $-5.2$  eV) and conduction band edge of ZnO is close to  $1.1$  eV resulting in a better exciton dissociation through fast electron injection to ZnO layer. The conduction band edge of ZnO ( $1.1$  eV), when compared to the lowest unoccupied molecular orbital (LUMO) of P3HT ( $-3.53$  eV) can also help the excitons dissociation in P3HT via rapid electron transfer to ZnO. Similarly, the arrangement of the energy levels of CuO and ZnO forms D/A pairs for rapid electrons transfer from CuO NPs to ZnO NPs. This rapid electron transfer will also help to dissociate the excitons. The ZnO NPs create a high potential barrier for holes in the P3HT to travel to the ZnO buffer layer. With a small forward bias stimulation, the electrons are moved to conduction bands (CB) of P3HT and CuO, and transferred to the LUMO of PC70BM acceptor materials as well as ZnO NPs.

Whereas, holes move from the donor to the ITO anode. If holes move to the ZnO layer, electrons and holes can be recombined generating leakage current, which leads to lower power conversion efficiency. However, ZnO buffer layer provides an energy barrier to prevent hole penetration into the valence band (VB) of ZnO.

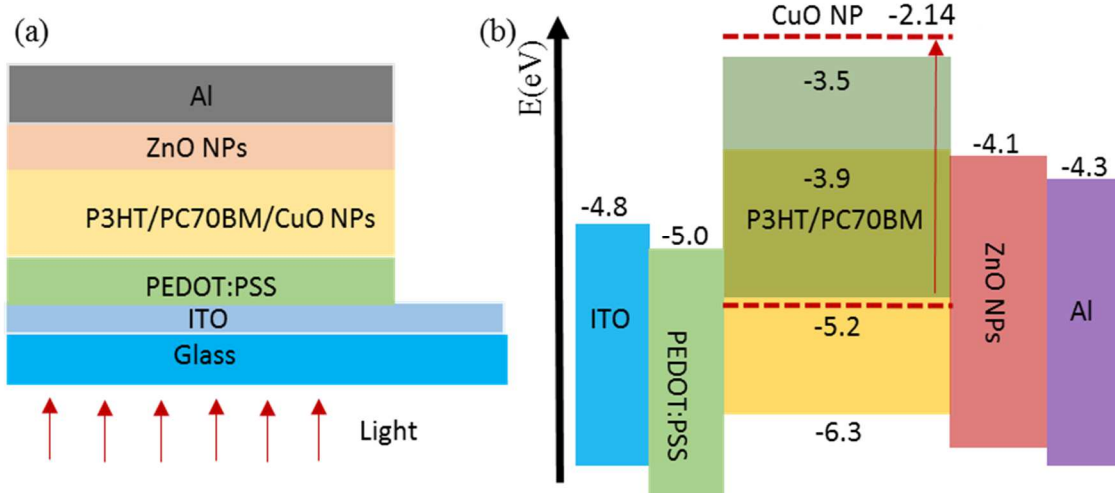


Figure 6.2: Graphical representation of the hybrid device architecture (a) Layer structure with ZnO buffer layer, (b) energy level diagram

The surface morphology of the active layers was studied by AFM as shown in Figure 6.3. AFM images show that the assembly of an electron transporting ZnO NPs layer on the active layer increases the roughness of the P3HT/PC70BM/CuO-NPs films. The measured root-mean-square roughness ( $\sigma_{rms}$ ) value of the P3HT/PC70BM/CuO layer was 0.33nm and after depositing the ZnO NPs layer on the active layer, the  $\sigma_{rms}$  value increased to 0.89nm. Sample E (P3HT/PCBM/CuO-0.6mg NPs with 40mg of ZnO NPs) exhibited a maximum surface roughness of 0.97nm. These roughened surfaces provide better interfacial contact with the Al layer and hence enhance the charge collection ability at the Al cathode. Also, enhanced



roughness can result in greater light absorption due to the diffuse reflection between the active layer and the cathode. In the ZnO NPs layers, the electrons mobility ( $6.6 \times 10^{-2} \text{ cm}^2 \text{ V}^{-1} \text{ s}^{-1}$ ) [26] is remarkably higher than that ( $1.7 \times 10^{-4} \text{ cm}^2 \text{ V}^{-1} \text{ s}^{-1}$ ) [27] of the amorphous  $\text{TiO}_x$  thin film. Hence, ZnO NPs layer can act as an effective electron transporting medium.

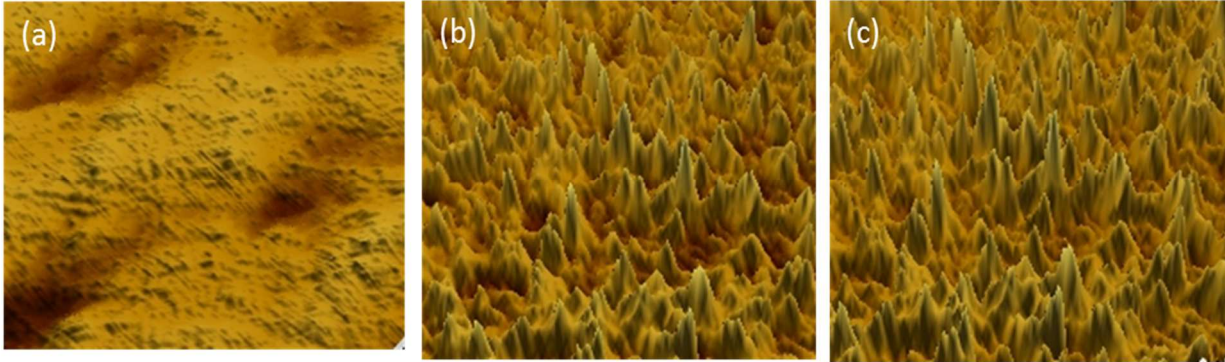


Figure 6.3: AFM images of active layer ( $2 \times 2 \mu\text{m}^2$  scans) with (a) P3HT/PCBM/CuO-0.6mg NPs (sample A), (b) P3HT/PCBM/CuO-0.6mg NPs with 20mg of ZnO NPs buffer layer (sample C), and (c) P3HT/PCBM/CuO-0.6mg NPs with 40mg of ZnO NPs buffer layer (sample E)

The UV–visible absorption spectra of the P3HT/PC70BM, P3HT/PC70BM/CuO, and P3HT/PC70BM/CuO/ZnO, are comparatively shown in Figure 6.4. The wavelength range of these absorption spectra is between 350 nm and 550 nm. The absorption intensities of the fabricated devices exhibited enhancements over the entire range. The optical absorption peak intensity of the P3HT/PC70BM thin layer is 0.31 and after incorporating CuO NPs in the blend, absorption intensity was improved to 0.63. Meanwhile, the ZnO NPs buffer layer assembled P3HT/PC70BM/ CuO NPs increased the absorption intensity to 0.76. Therefore, the CuO NPs and ZnO NPs led to higher optical absorption in the solar cells over the entire wavelength range.

A higher optical absorption yields more electrons-holes generation, higher carrier mobility, and more carrier injection to the electrodes resulting in better power conversion

efficiency of the solar device. As mentioned earlier, the roughness values of P3HT/PC70BM/CuO assembled with a ZnO NPs buffer layer were improved and this rougher surface can reflect more light between the ZnO layer and the Al cathode. In addition, an increase in the surface area, due to higher surface roughness, enhances the absorption spectra of the P3HT/PC70BM/CuO and ZnO NPs compared to the P3HT/PCBM reference film [28].

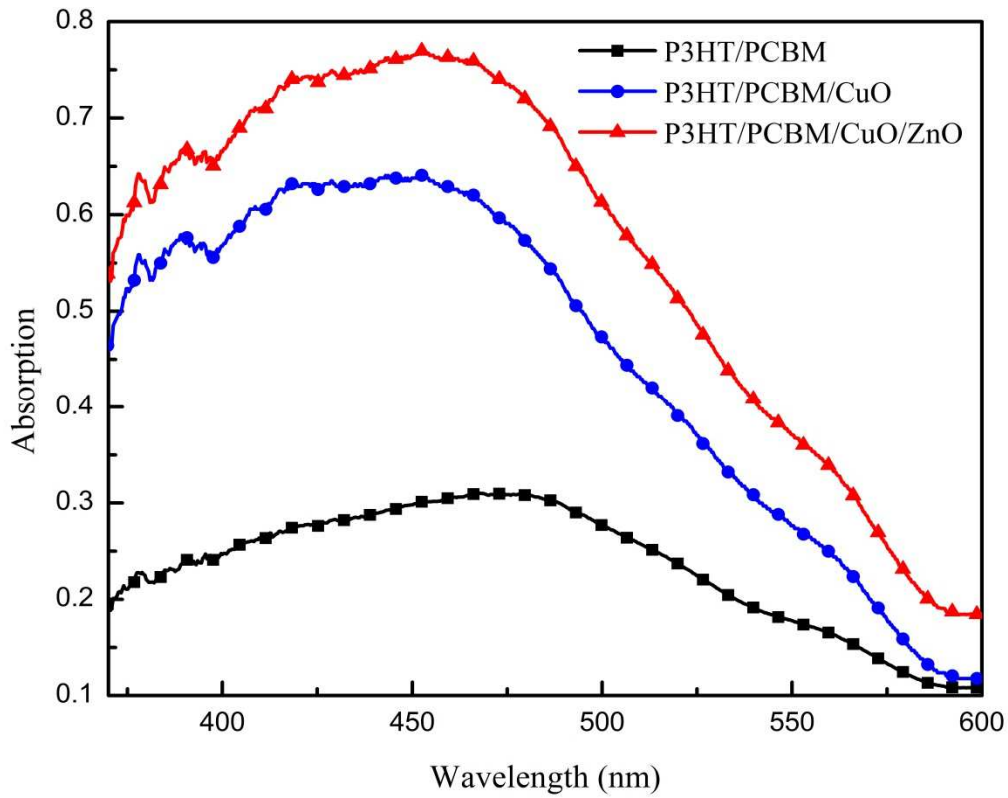


Figure 6.4: Optical absorption spectra of the hybrid solar cells with CuO and ZnO NPs

The EQE or the incident photon to current conversion efficiencies (IPCE) measurements describe the ratio between the incident photons on the solar cell, from the input source, and the generated free charges carriers by the solar cell. The enhanced light absorption, exciton dissociation rate, carrier collection at the electrodes and improved charge carrier mobility

strongly affect the EQE measurements. Figure 6.5 shows the corresponding EQE measurements. When the particle densities in the ZnO buffer layer were increased, relevant EQEs were proportionally increased in the wavelength range from 310nm to 650nm. The peak values of the EQE for samples A, B, C, D, and E are 54.6%, 56.8%, 61.8%, 60% and 57.7%; respectively.

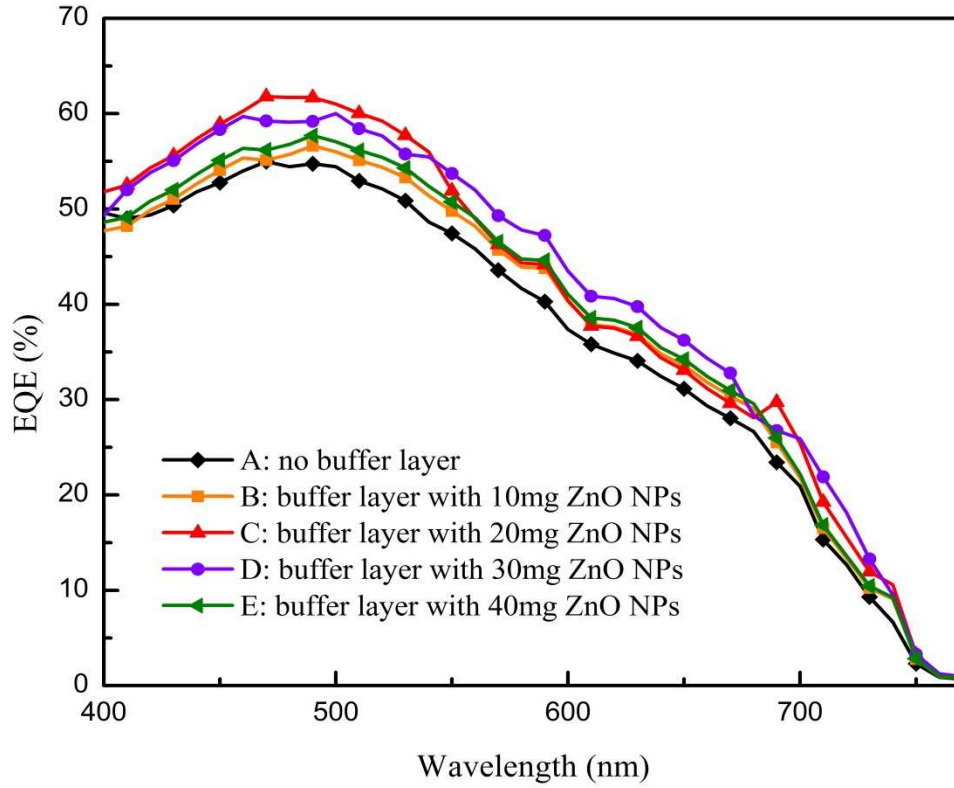


Figure 6.5: EQE of the hybrid solar cells with ZnO buffer layer

The EQE has a linear relationship with the  $J_{sc}$  of the solar cell devices. The  $J_{sc}$  is the major determinant of power conversion efficiency; where  $PCE = (J_{sc} * V_{oc} * FF) / P_{in}$ . The  $J_{sc}$  values obtained for each cell followed a similar trend to EQE, which shows that the cells with 0.06 mg of ZnO NPs in the electron transport buffer layer exhibit the highest  $J_{sc}$  values. Table 6.1 summarizes the photovoltaic performance parameters, such as  $J_{sc}$ ,  $V_{oc}$ , fill factor (FF), and PCE,

for all the fabricated devices. The corresponding current–voltage (J-V) characteristics with AM 1.5G irradiation ( $100 \text{ mW cm}^{-2}$ ) of solar cells using different ZnO NPs electron transporting buffer layers are shown in Figure 6.6.

Table 6.1: Electric parameters of ITO/PEDOT:PSS P3HT/PCBM/CuO-0.6mg NPs/ZnO NPs/ Al solar cells.

Sample	$J_{sc}(\text{A/cm}^2)$	$V_{oc}(\text{V})$	FF(%)	$R_s(\Omega/\text{cm}^2)$	PCE(%)
A	6.480	0.677	68.11	9.2	2.988
B	7.063	0.688	71.44	8.4	3.472
C	7.620	0.696	74.47	7.8	3.950
D	7.437	0.702	72.46	8.0	3.784
E	7.379	0.714	69.79	8.3	3.677

As shown in Table 6.1, the control device without ZnO electron transporting buffer layer shows  $J_{sc}$  of  $6.48 \text{ mA cm}^{-2}$ , FF of 68.11%,  $V_{oc}$  of 0.677 V and a power conversion efficiency (PCE) of 2.988%. However, PCE clearly increased after assembling the ZnO electron transport layer next to the P3HT/PC70BM/CuO layer. The optimum photovoltaic parameters were obtained by the devices with 20mg ZnO NPs (sample C) in the electron transport layer, which exhibit a  $J_{sc}$  of  $7.620 \text{ mA cm}^{-2}$ , a FF of 74.47%, a  $V_{oc}$  of 0.696 V and a PCE of 3.950%.

However, as the ZnO NPs content increased further, the PCE of the solar cells decreased. The PCE of the device with 40mg of ZnO in the buffer layer decreased by 6.9%, and the photovoltaic parameters also decreased correspondingly to  $J_{sc}$  of  $7.379 \text{ mA cm}^{-2}$  and a reduced FF of 69.79%, leading to a final PCE of 3.68%. The fill factor (FF) mainly depends on the structural morphology of the active layer and the series resistance of the devices [29, 30].

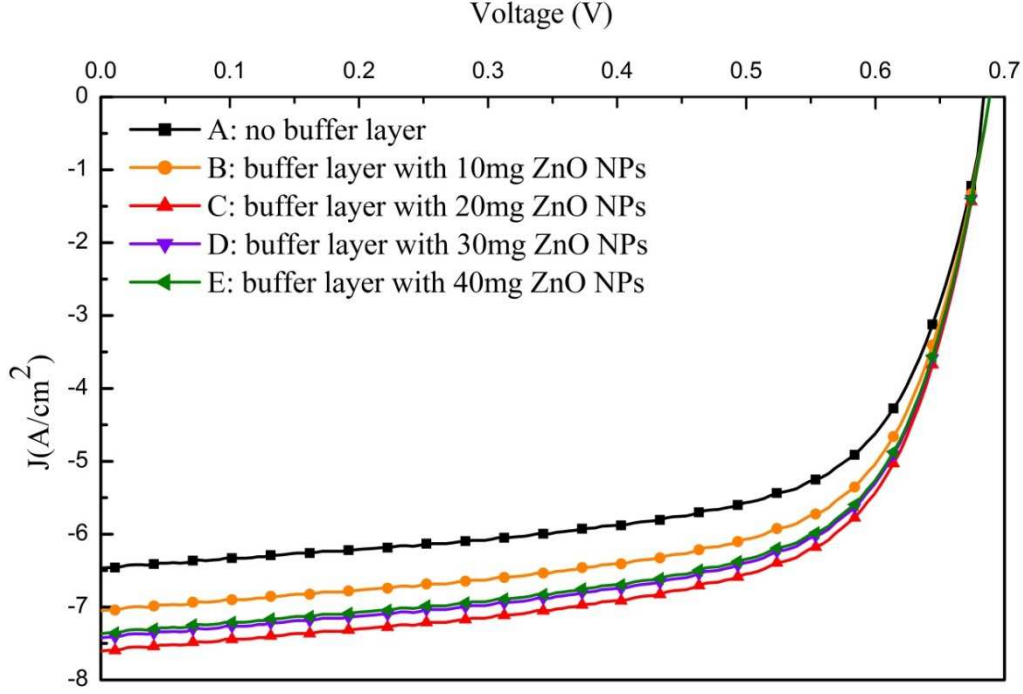


Figure 6.6:  $J$ - $V$  characteristics of hybrid polymer solar cells ZnO buffer layer

However, the fill factor decreased from 74.47% to 69.79% with increasing the amount of ZnO in the buffer layer. The series resistance of the device increases with increasing the amount of ZnO NPs in the electron transport buffer layer (Table 6.1). This may be the main reason that  $J_{sc}$  and FF tend to decrease beyond the optimum amount of ZnO NPs in the samples. Furthermore, increase of ZnO NPs in the buffer layer, exceeding the optimum amount of 20 mg, allows the ZnO NPs to penetrate to P3HT/PCBM/CuO film and changing nanoscale morphology within P3HT/PCBM /CuO blend. This morphology change causes a significant reduction of donor/acceptor contact surface, thus lowering the EQE and  $J_{sc}$  of the cells.

Open circuit voltage ( $V_{oc}$ ) has a linear relationship to the energized band levels within D-A phases. The  $V_{oc}$  of a hybrid solar cell can be increased by moving the polymer HOMO level

further away from the vacuum level [31]. However,  $V_{oc}$  did not change significantly, possibly since the LUMOs of P3HT and PC70BM were constant; thus suggesting that the reduced recombination due to increased carrier mobility did not improve  $V_{oc}$ . On the other hand, the HOMO energy level of P3HT in the active layer was not influenced by the ZnO buffer layer in the solar cell device. Therefore; ZnO-NPs did not enhance  $V_{oc}$  in the solar cells [32].

### 6.2.2 Annealing Effect

The performance characteristics of the devices which contain 0.6mg of CuO NPs and varying amounts of ZnO NPs in the buffer layer were measured after annealing at 200°C for 30 minutes. The photovoltaic parameters are shown in Table 6.2.

Table 6.2: Performance parameters of PEDOT:PSS/P3HT/PCBM/CuO-NPs/ZnO NPs hybrid solar cells before and after heat treatment 200°C for 30 minutes (B/A: before annealing, A/A: after annealing)

ZnO NPs (mg)	$J_{sc}$ (mA/cm <sup>2</sup> )		$V_{oc}$ (V)		FF (%)		PCE (%)	
	B/A	A/A	B/A	A/A	B/A	A/A	B/A	A/A
0	6.480	7.777	0.677	0.679	68.11	69.53	2.988	3.672
10	7.063	8.890	0.688	0.680	71.44	71.62	3.472	4.330
20	7.620	8.949	0.696	0.678	74.47	74.77	3.950	4.530
30	7.437	8.810	0.702	0.681	72.46	74.40	3.784	4.464
40	7.379	8.107	0.714	0.683	69.79	69.88	3.677	3.875

The J-V characteristic parameters of the reference devices (0mg ZnO-NPs) after annealing revealed a  $J_{sc}$  of 7.777 mA/cm<sup>2</sup>. It increased to 8.949 mA/cm<sup>2</sup> after assembling a

buffer layer containing 20 mg of ZnO NPs, an enhancement of 15%. This enhanced short circuit current density proportionally improved the PCE from 3.672% to 4.530%. Following a similar trend, the fill factor increased from 69.53 to 74.77% after annealing treatments. The devices before annealing exhibited a PCE of 2.988% in the reference device and it improved to 3.950% with ZnO nanostructured buffer layer. The thermal annealing treatment contributed for about 23% increase in PCE as a result of notably improved  $J_{sc}$  and FF. However, the open-circuit voltage ( $V_{oc}$ ) did not change significantly before and after annealing treatments.

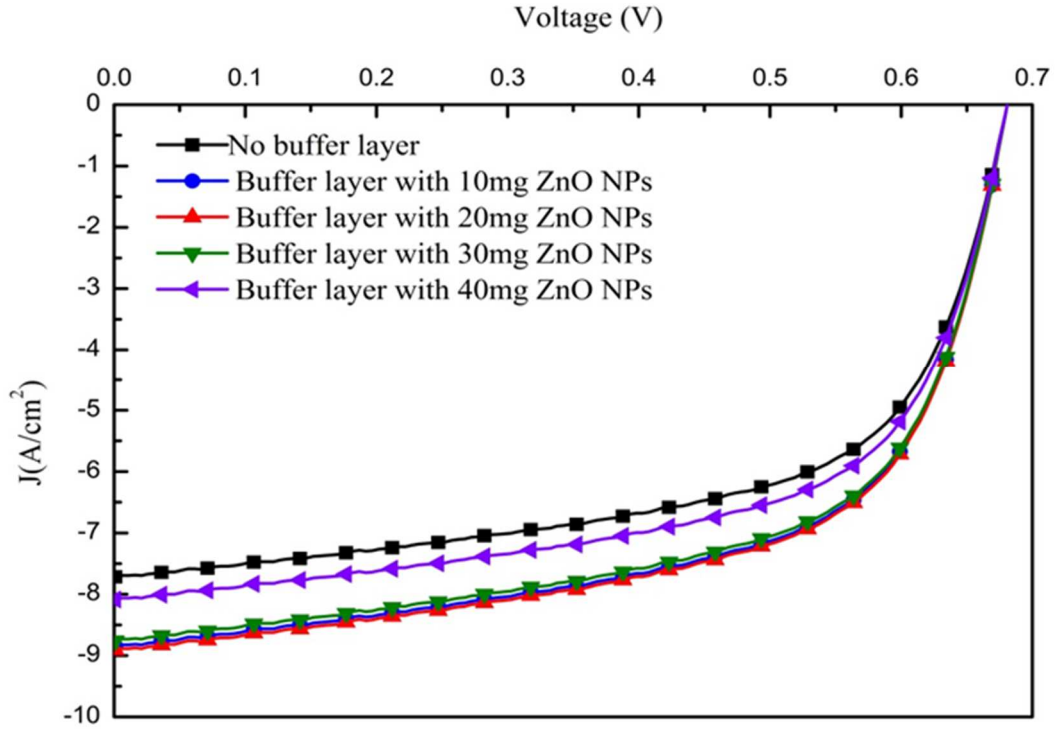


Figure 6.7:  $J$ - $V$  characteristics of hybrid polymer solar cells ZnO buffer layer after annealing

Based on power conversion efficiency equation ( $PCE = V_{oc} * J_{sc} * FF / \text{total incident power density}$ )  $V_{oc}$ ,  $J_{sc}$ , and FF are significant factors in determining the overall PCE. Higher  $V_{oc}$ ,  $J_{sc}$ ,



and FF result in higher PCE. The current density-voltage ( $J$ - $V$ ) characteristics of the solar cells before and after annealing are shown in Figure 6.7.

The solar cell devices assembled with a ZnO buffer layer (20mg of NPs) and 0.6mg of CuO NPs were annealed at three different temperatures: 150°C, 200°C and 250°C, for 30 minutes. The performance characteristics of these devices are summarized in Table 6.3. At all annealing temperatures, the devices show a significant improvement of PCEs compared to the devices without annealing treatment. The devices annealed at 200°C for 30 minutes, exhibit the optimum performance. However, the lowest short circuit current density ( $J_{sc}$ ) of 8.186 mA/cm<sup>2</sup>, open circuit voltage ( $V_{oc}$ ) of 0.674 V, filling factor (FF) of 69.05%, and PCE of 3.81% were obtained from the devices annealed at 250°C. The devices annealed at 150°C, exhibited a  $J_{sc}$ ,  $V_{oc}$ , FF and PCE of 8.870 mA/cm<sup>2</sup>, 0.675 V, 71.40% and 4.275%; respectively.

Table 6.3: Performance characteristics of polymer solar cells with different annealing temperatures

Temperature (°C)	$J_{sc}$ (A/cm <sup>2</sup> )	$V_{oc}$ (V)	FF (%)	PCE (%)
150	8.870	0.675	71.40	4.275
200	8.949	0.678	74.77	4.530
250	8.186	0.674	69.05	3.810

The  $J_{sc}$  improvement is closely related to the EQE trend. The corresponding EQE measurements (peak values) are shown in Figure 6.8. When the particle densities in the ZnO buffer layer were increased, the relevant EQEs proportionally increased in the wavelength range from 310nm to 650nm. Before annealing, the devices had highest EQEs of 54.6%, 56.8%,



61.8%, 60% and 57.7%; respectively. However, after annealing the peak values of the EQE for samples with 0 mg-ZnO, 10 mg-ZnO, 20 mg-ZnO, 30 mg-ZnO, and 40 mg-ZnO were 55.5%, 57.8%, 62.9%, 61.4% and 56.7%; respectively.

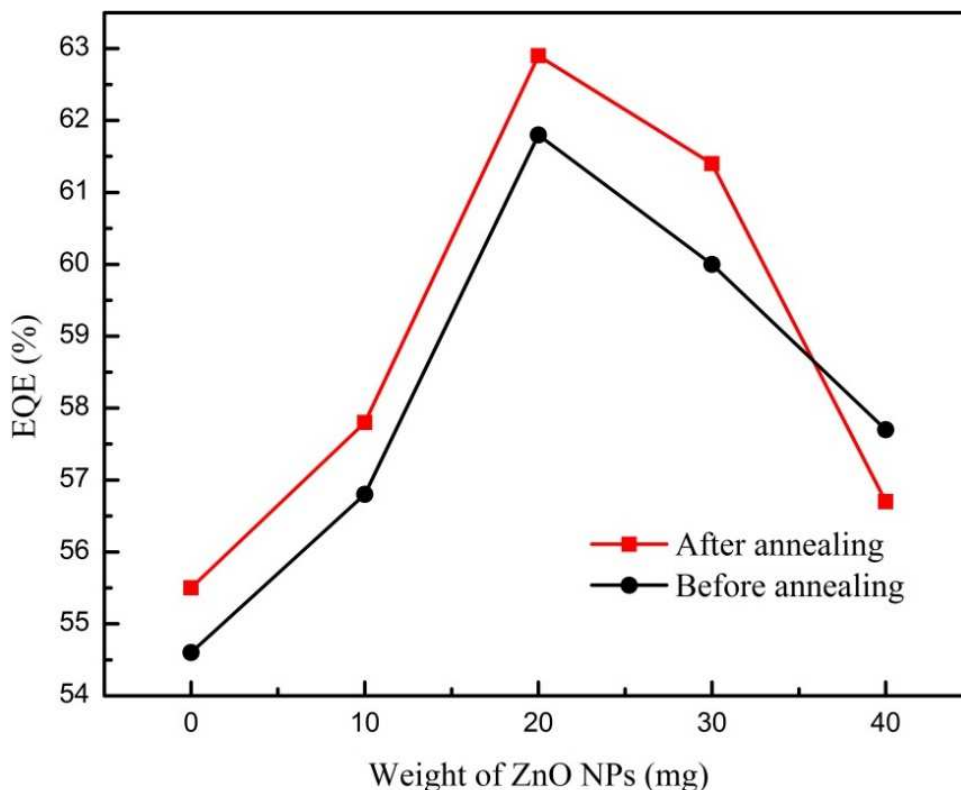


Figure 6.8: Effect of thermal annealing on the EQE values of PSCs with ZnO buffer layer

Here, the P3HT/PCBM/CuO NPs structure provides two main electron-transporting paths: a conventional path through the PCBM molecules and hopping sites created by CuO NPs. The CuO NPs produce dense PCBM clusters with hopping sites creating an efficient electron flow towards the ZnO electron transport layer. The enhancement of EQE measurements is generally attributed to improved PCBM molecules. The ZnO electron transport buffer layer provides extremely high electron transporting facility to the Al electrodes uplifting the EQE profile. Therefore, the separated free electrons from excitons, created in P3HT and CuO NPs

phases, can be transported through interconnected PCBM domains and CuO NPs hopping centers towards the ZnO buffer layer.

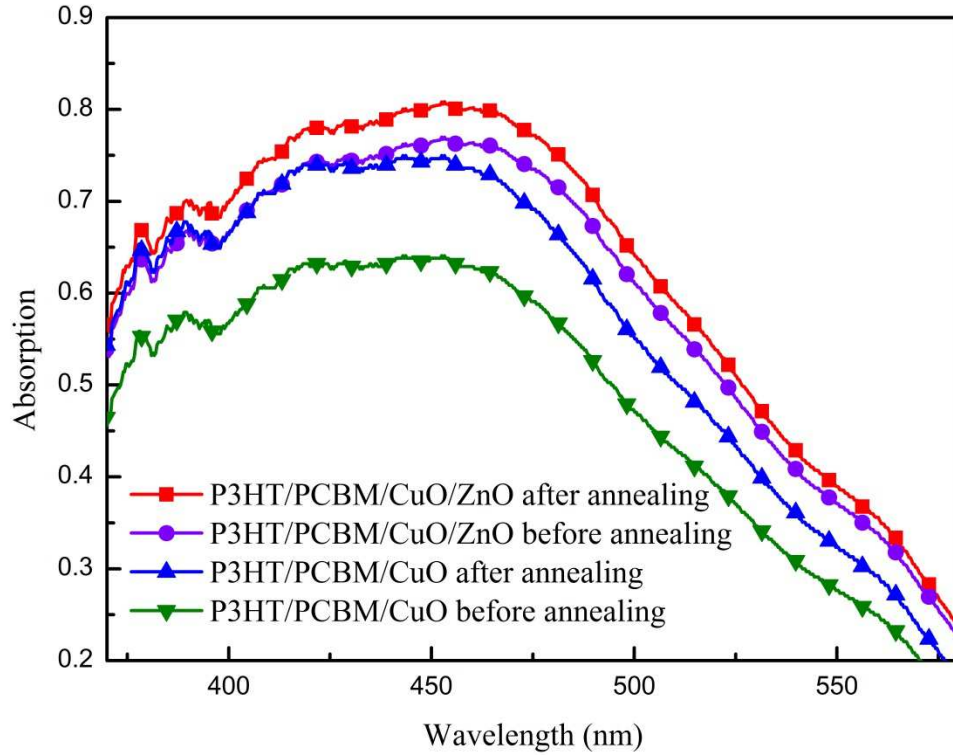


Figure 6.9: Optical absorption spectra of PSCs with CuO and ZnO NPs before and after annealing

To further study the effect of heat treatment on the optical properties of ZnO buffer layer assembled P3HT/PC70BM/0.6mg-CuO NPs PSCs, the UV visible absorption spectra were obtained, as shown in Figure 6.9. After thermal annealing, the absorption intensities of all devices were enhanced. The optical absorption peak intensity of the P3HT/PC70BM/CuO NPs thin layer is 0.64 and after ZnO NPs buffer layer assembling, the absorption intensity was improved to 0.76. However, the annealing treatment of the ZnO NPs buffer layer assembled P3HT/PC70BM/ CuO NPs devices increased the absorption intensity to 0.81. Consequently, the

CuO NPs, ZnO NPs as well as thermal annealing led to higher optical absorption in the solar cells over the entire wavelength range. The increased absorption intensities are attributed to the enhanced crystallinity of P3HT by thermal annealing combined with improved optical absorption caused by CuO/ZnO NPs incorporated in the solar cell devices. Improved optical absorption yields higher charge carrier generation rate, better carrier mobility, and higher carrier injection to the electrodes resulting in better power conversion efficiency of the solar devices [33, 34].

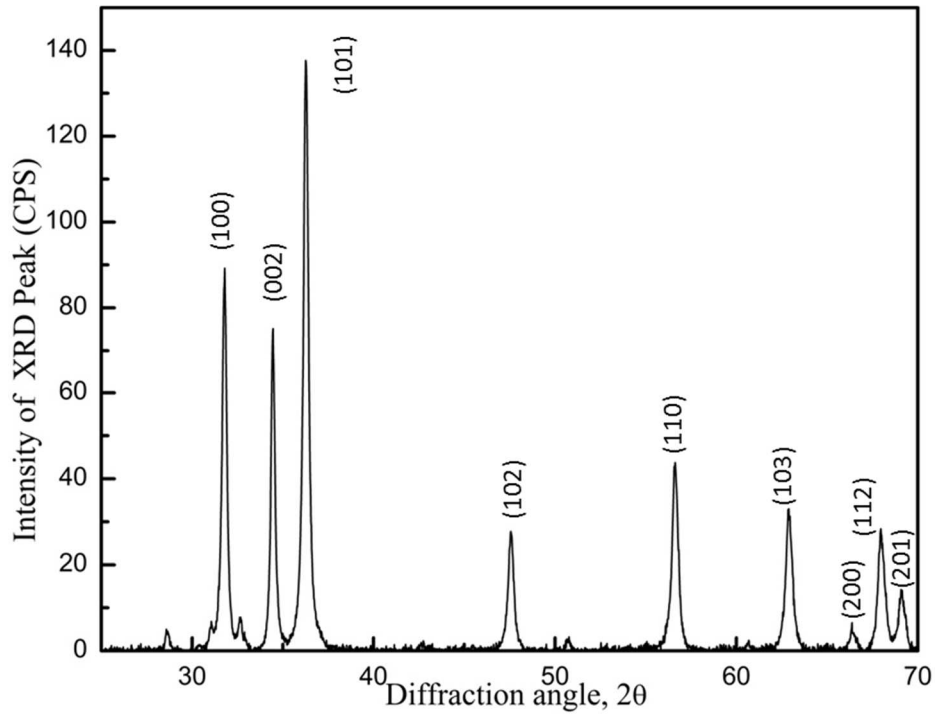


Figure 6.10: XRD pattern of ZnO NPs sample

Figure 6.10 shows the XRD patterns of ZnO NPs. Different peaks were observed at  $(2\theta) = 31.81^\circ, 34.31^\circ, 36.14^\circ, 47.40^\circ, 56.52^\circ, 62.73^\circ, 66.28^\circ, 67.91^\circ,$  and  $69.03^\circ$  were assigned to (100), (002), (101), (102), (110), (103), (200), (112), and (201) of ZnO NPs, indicating that the

sample has a polycrystalline wurtzite structure. There are no other characteristic impurities peaks observed which also confirm that the product obtained is in a high purity ZnO phase.

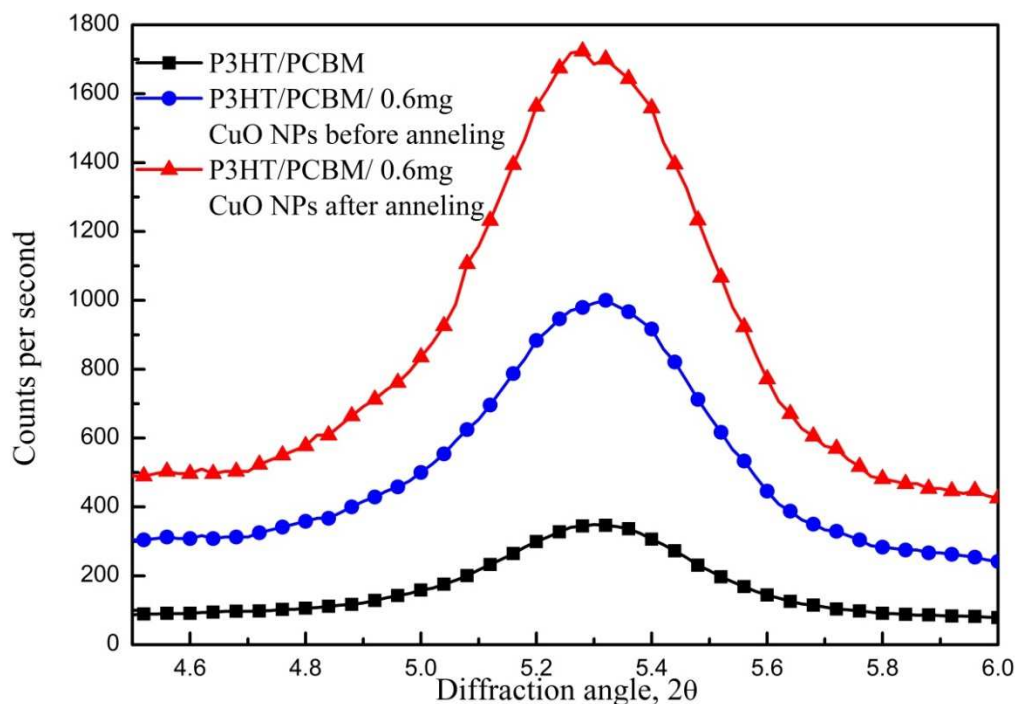


Figure 6.11: XRD spectra for 0.6 mg of CuO NPs incorporated P3HT/PCBM thin films

The XRD spectra of the P3HT/PC70BM/0.6mg-CuO NPs samples were obtained before and after thermal annealing. The XRD spectra, shown in Figure 6.11, illustrate improved peak intensities over the  $2\theta$  range from  $4.5^\circ$  to  $6^\circ$ . The increased diffraction peaks for P3HT:PC70BM: CuO NPs thin films are contributed to the improved self-organization of P3HT molecules leading to higher crystallinity. It is well known that P3HT and PC70BM are crystalline and amorphous materials; respectively. Therefore, P3HT/PC70BM and CuO NPs blend is a partially crystalline structure. The thermal annealing of 0.6mg-CuO NPs facilitate

P3HT chains to escape from the amorphous phase and rearrange as separate molecules within the polymer blend leading to P3HT/ PC70BM phase separation [35, 36].

Surface morphological studies of the active layers were carried out using AFM. AFM images, presented in Figure 6.12, show that the thermal annealing increases the surface roughness of the nanostructured ZnO films which is assembled on the P3HT/PC70BM/CuO NPs thin film. The measured root-mean-square roughness ( $\sigma_{rms}$ ) value of the P3HT/PC70BM/CuO layer was 0.33nm and after depositing the ZnO NPs layer on the active layer, the  $\sigma_{rms}$  value increased to 0.91nm. However, after annealing, the optimum sample (P3HT/PCBM/0.6mg-CuO NPs with 20mg of ZnO NPs) exhibited a maximum surface roughness of 1.12nm. The rougher surfaces increase the interfacial contact area with the Al layer leading to higher charge collection ability at the Al cathode. Also, enhanced roughness can result in greater light absorption due to the diffuse reflection between the active layer and the cathode. Therefore, annealing of nanostructured ZnO thin films at 200°C for 30 minutes optimizes the surface condition of the thin layers.

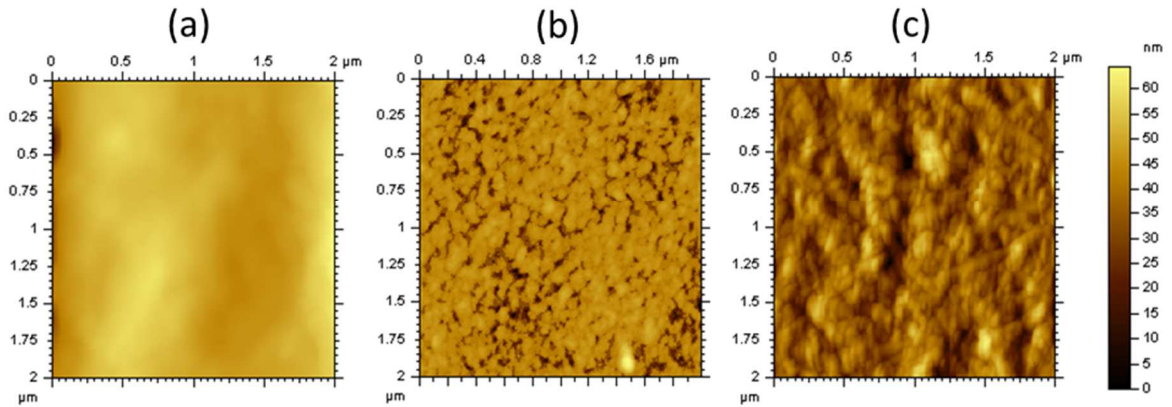


Figure 6.12: AFM images (2D) of active layer: (a) P3HT/PC70BM/0.6mg CuO NPs (b) P3HT/PCBM/CuO-0.6mg NPs with 20mg of ZnO NPs buffer layer (c) P3HT/PCBM/CuO-0.6mg NPs with 40mg of ZnO NPs buffer layer after annealing

### 6.3 Conclusion

In this study, ZnO nanoparticles are incorporated in an electron transport buffer layer assembled on top of the P3HT/PC70BM/CuO NPs active layer. After incorporating the electron transport layer, the PCE increased from 2.988% to 3.950% in the cells containing 20mg ZnO-NPs (sample C) in the buffer layer, which is equivalent to a 32.19% improvement in efficiency. The higher performance is attributed to enhanced EQE, electron mobility, exciton dissociation and optical absorption due to CuO and ZnO NPs in the device. The optical absorption spectrum exhibited significant improvement in the presence of ZnO-NPs buffer layer due to the elevated exciton generation rate. AFM analysis shows an increase in surface roughness of the active layer after depositing the ZnO nanoparticles incorporated electron transport buffer layer, which results in a larger contact area between ZnO and the Al cathode.

In order to investigate the annealing effect on the devices, all the devices were thermally annealed at three different temperatures which are 150°C, 200°C and 250°C, for 30 minutes. The devices which were annealed at 200°C for 30 minutes exhibited the optimum performance. The PCE for the cells containing 20mg of ZnO-NPs increased from 3.95% to 4.53% after heat treatment at 200°C for 30 minutes. The improved performance is attributed to enhanced EQE, electron mobility, surface roughness and optical absorption due to the presence of CuO and ZnO NPs in the devices. In addition, the optical absorption spectrum exhibited significant improvement after thermal annealing treatment due to the elevated exciton generation rate. AFM analysis shows an increase in surface roughness of the ZnO nanoparticles incorporated electron transport buffer layer after thermal annealing. The enhanced roughness results in greater light absorption due to the diffuse reflection between the active layer and the cathode which results in

a larger interfacial contact area between ZnO and the Al cathode leading to higher charge collection ability at the Al cathode.

## References

- [1] Frederik, C., Colin, L. , Neil, L. A., Ye, S., Michael, N. R. A., and John, H. H., 2005. Growth of ZnO thin films—experiment and theory, *J. Mater. Chem.* 15; 139–148.
- [2] Anderson, J. and Chris, G., Van, de W., 2009. Fundamentals of zinc oxide as a semiconductor, *Rep. Prog. Phys.* 72:126501.
- [3] Wang, E., Tao, L., Wang, Z., Hellström, S., Zhang, F., Inganäs, O., Andersson, M. R., 2010. An Easily Synthesized Blue Polymer for High-Performance Polymer Solar Cells. *Adv. Mater.* 22: 5240.
- [4] Zhang, F., Mammo, W., Andersson, L. M., Admassie, S., Andersson M. R., and Inganäs, O., 2006. Low-Bandgap Alternating Fluorene Copolymer/Methanofullerene Heterojunctions in Efficient Near-Infrared Polymer Solar Cells. *Adv. Mater.* 18: 2169.
- [5] Huang, Y., Guo, X., Liu, F., Huo, L., Chen, Y., Russell, T. P., Han, Li Y., and Hou, J., Improving the Ordering and Photovoltaic Properties by Extending–Conjugated Area of Electron-Donating Units in Polymers with D-A Structure. *Adv. Mater.* 24: 3383.
- [6] Wang, E., Tao, L., Wang, Z., Hellström, S. F., Zhang, F., Inganäs, O., Andersson, M. R., 2010. An Easily Synthesized Blue Polymer for High-Performance Polymer Solar Cells. *Adv. Mater.* 22: 5240.
- [7] Reese, M. O., Nardes, A. M., Rupert, B. L., Larsen, R. E., Olson, D. C., Lloyd, M. T., Shaheen, S. E., Ginley, D. S., Rumbles G., and Kopidakis, N., 2010. Photoinduced Degradation of Polymer and Polymer–Fullerene Active Layers: Experiment and Theory *Adv. Funct. Mater.* 20: 3476.
- [8] He, Z. Mei, Z. Su, S. Xu, M., 2012. Enhanced power-conversion efficiency in polymer solar cells using an inverted device structure. *Nature Photon.* 6: 591.
- [9] Shao, S., Liu, J., Zhang, B., Xie, Z., Wang, L., 2011. Enhanced stability of zinc oxide-based hybrid polymer solar cells by manipulating ultraviolet light distribution in the active layer. *Appl. Phys. Lett.* 98: 203304.
- [10] Huang, J., Yin, Z., Zheng, Q., 2011. Applications of ZnO in organic and hybrid solar cells *Energy Environ. Sci.*, 4:3861.
- [11] Lin, Y.-Y., Chu, T.-H., Li, S.-S., Chuang, C.-H., Chang, C.-H., Su, W.-F., 2009. Interfacial Nanostructuring on the Performance of Polymer/TiO<sub>2</sub> Nanorod Bulk Heterojunction Solar Cells. *J. Am. Chem. Soc.* 131: 3644.
- [12] Li, G., Zhu, R. and Yang, Y., 2012. Polymer solar cells. *Nature Photonics.* 6: 153.
- [13] Niki S., Contreras M., Repins I., Powalla M., Kushiya K., Ishizuka S. and Matsubara K., 2010. *Prog. Photovolt. Res. Appl.*, 18: 453.



- [14] Fung D.D.S., Qiao L.F., Choy W.C.H. et al. 2011 Optical and electrical properties of efficiency enhanced polymer solar cells with Au nanoparticles in a PEDOT–PSS layer. *J. Mater. Chem.* 21: 16349–16356.
- [15] Chris, G., Walle, V., 2003. Effects of impurities on the lattice parameters of GaN. *Physical review B.* 68: 165209.
- [16] Sekine, N., Chou, C.H., Kwan, W.L., Yang, Y., 2009. ZnO nano-ridge structure and its application in inverted polymer solar cell. *Org. Electron.* 10: 1473.
- [17] Oh, S.A., Heo, S.J., Yang, J.S., and Kim, H.J., 2013. Effects of ZnO Nanoparticles on P3HT: PCBM Organic Solar Cells with DMF-Modulated PEDOT: PSS Buffer Layers. *ACS Appl. Mater. Interfaces.* 5: 11530.
- [18] Wu, Z., Song, T., Xia, Z., Wei H., and Sun, B., 2013. Enhanced performance of polymer solar cell with ZnO nanoparticle electron transporting layer passivated by in situ cross-linked three-dimensional polymer network. *Nanotechnology* 24: 484012.
- [19] Zhu, F., Chen, X., Lu, Z., Yang, J., Huang, S., Sun, Z., 2014. Efficiency Enhancement of Inverted Polymer Solar Cells Using Ionic Liquid-functionalized Carbon Nanoparticles-modified ZnO as Electron Selective Layer. *Nano-Micro Lett.* 6(1): 24.
- [20] Gao, H.L. Zhang, X.G. Meng, J.H. Yin, Z.G. 2015. Enhanced efficiency in polymer solar cells via hydrogen plasma treatment of ZnO electron transport layers. *J. Mater. Chem. A*, 3: 3719.
- [21] Kidowaki, H., Oku, T., and Akiyama, T., 2012. Fabrication and characterization of CuO/ZnO solar cells. *Journal of Physics: Conference Series.* 352:1.
- [22] Ikram, M., Murrayc, R., Imran, M., Ali, S., Ismat Shah, S., 2007. Enhanced performance of P3HT/ (PCBM: ZnO: TiO<sub>2</sub>) blend based hybrid organic solar cells. *Materials Research Bulletin.* 75: 35–40.
- [23] Qian, L., Yang, J., Zhou, R., Tang, A., Zheng, Y., Tseng, T.K., Bera, D., 2011. Hybrid polymer-CdSe solar cells with a ZnO nanoparticle buffer layer for improved efficiency and lifetime. *J. Mater. Chem.*, 21: 3814.
- [24] Wang, M., Wang, X., 2008. P3HT-ZnO bulk-heterojunction solar cell sensitized by a perylene derivative. *Sol. Energy Mater. Sol. Cells*, 92: 766.
- [25] Beek, W. J. E., Wienk, M. M., and Janssen, R. A. J., 2004. Efficient hybrid solar cells from zinc oxide nanoparticles and a conjugated polymer. *Adv. Mater.* 16: 1009–1013.
- [26] Wang, D. H., Moon, J. S., Seifert, J., Jo, J., Park, J. H., Park, O., and Heeger, A. J., 2011. Sequential Processing: Control of Nanomorphology in Bulk Heterojunction Solar Cells. *Nano Lett.* 11(8):3163–3168.

- [27] Kim, J. Y., Kim, S. H., Lee, K., Lee, H. H., Ma, W., Gong X., and Heeger, A. J., 2006. New Architecture for High-Efficiency Polymer Photovoltaic Cells Using Solution-Based Titanium Oxide as an Optical Spacer. *Adv. Mater.* 18: 572.
- [28] Roest, L., Kelly, J. J., Vanmaekelbergh D., and Meulenkaamp, E. A., 2002. Staircase in the Electron Mobility of a ZnO Quantum Dot Assembly due to Shell Filling. *Phys. Rev. Lett.*, 89: 036801.
- [29] Ikram, M., Ali, S. Murray, R., Hussain, A., 2015. Influence of fullerene derivative replacement with TiO<sub>2</sub>nanoparticles in organic bulk heterojunction solar cells. *Current applied physics*. 15(1): 48–54.
- [30] Djara, V., and Bernède, J., 2005. Effect of the interface morphology on the fill factor of plastic solar cells. *Thin Solid Films*, 493: 273.
- [31] Oo, T., Mathews, N., Tam, T., Xing, G., Sum, T., Sellinger, A., Wong, L., Mhaisalkar, S., 2010. Investigation of photophysical, morphological and photovoltaic behavior of poly (p-phenylene vinylene) based polymer/oligomer blends. *Thin Solid Films*. 518: 5292.
- [32] Ji, C.H., Oh, I.S., Oh, S.Y., 2015. Improving the performance of organic solar cells using an electron transport layer of B4PyMPM self-assembled nanostructures *Electron. Mater.* 44(5): 795.
- [33] Bundgaard, E., and Krebs, F. C., 2007. Low Band Gap Polymers for Organic Photovoltaics. *Sol. Energy Mater. Sol. Cells*. 91(11):954–985.
- [34] Bundgaard, E., Shaheen, S. E., Krebs, F. C., and Ginley, D. S., 2007. Bulk Heterojunctions Based on a Low Band Gap Copolymer of Thiophene and Benzothiadiazole. *Sol. Energy Mater. Solar Cells*. 91(17):1631–1637.
- [35] Pascui, O. F., Lohwasser, R., Sommer, M., Thelakkat, M., Thurn-Albrecht, T., and Saalwachter, K., 2010. High Crystallinity and Nature of Crystal–Crystal Phase Transformations in Regioregular Poly(3-hexylthiophene). *Macromolecules*. 43 (22): 9401–9410.
- [36] Sun, Y., Cui, C., Wang, H., and Li, Y., 2011. Efficiency Enhancement of Polymer Solar Cells Based on Poly (3-hexylthiophene)/Indene-C70 Bisadduct via Methylthiophene Additive. *Adv. Energy Mater.* 1(6):1058–1061.

## CHAPTER 7

### **Objective 4: Improvement of Hole Collection Ability in Polymer Solar Cells Using Au NPs**

#### **7.1 Introduction**

The PSCs have several obstacles for further efficiency improvement due to the limited charge collection, the short exciton diffusion length and the low carrier mobility. Previous studies have revealed that the Au NPs improve the optical absorption and hole collection at the anode yielding better power conversion efficiency [1]. After incorporation of Au NPs in the PEDOT:PSS layer, the Au NPs contribute to the improvement of the PCE through enlarging the interfacial contact area between active layer and PEDOT:PSS buffer layer. Also Au NPs improve the PEDOT:PSS electrical conductivity. Therefore, the investigation of the performance changes of PSCs with Au NPs is highly important and desirable to better understand the physics within the ‘plasmonic’ PSCs [2].

Metal nanoparticles such as Au NPs, with diameters ranging from 1 to 100 nm, are natural links between molecules and extended solids. They are complex many-electron systems, potentially tunable with particle size and shape. Metal nanoparticles provide interesting and unique optical and electronic properties due to the localized surface plasmon resonance effect (LSPR). The LSPR can occur in illuminated metallic nanoparticles, like gold nanoparticles (Au-NPs), when oscillations of the incident electric field resonate with the surface electronic charges on those nanoparticles [3, 4]. This oscillation of the charges around the particle surface causes a positive and negative charge separation with respect to the ionic lattice, forming a dipole oscillation along the direction of the electric field of the light as shown in Figure 7.1(a) [5]. The maximum oscillation amplitude occurs at a specific frequency, called surface plasmon resonance

(SPR). This LSPR causes strong optical absorption which can be measured using a UV–Vis absorption spectrometer. Also, LS allows Au-NPs to absorb light in the visible region of the spectrum leading to intensification by a factor of 100 in the electromagnetic (EM) field surrounding them [6].

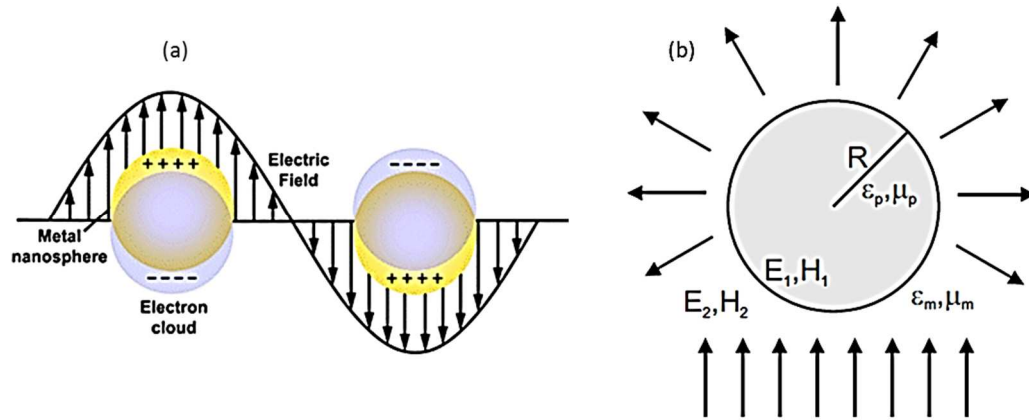


Figure 7.1: (a) Schematic indication of surface plasmon resonance on plasmonic nanoparticles [5] and (b) an illuminated nanoparticle

As theoretically explained by Mie theory, the LSPR band intensity and wavelength rely on the factors which affect the electron charge density on the particle surface; such as particle size, shape, structure, composition and the dielectric constant of the surrounding medium. The LSPR can be divided into two types which are: scattering and absorption. If a small particle is illuminated by light, its electrons are set in an oscillatory motion, which generates radiation at the same wavelength in all directions [7]. This process is called scattering. If the particle transfers the energy of the exciting light to another energy source, e.g. heat, the light is said to be absorbed (the energy is transferred into vibrations of the lattice known as phonons). The total extinction of the light beam by the sample contains contributions of both scattering and absorption, and the extinct energy is the sum of the absorbed and scattered energy. The

absorption and scattering of light by a small particle involves solving Maxwell's equations with relevant boundary conditions. Considering the harmonic time dependence of the light source, the Maxwell's equations can be rewritten in vector wave equation form;

$$\nabla^2 E + k^2 E = 0 \quad (7.1)$$

$$\nabla^2 H + k^2 H = 0 \quad (7.2)$$

where  $k$  is the wave number ( $k^2 = \omega^2 \epsilon \mu$ ),  $\epsilon$  is the dielectric function, and  $\mu$  is the magnetic permeability. The  $\epsilon$  and  $\mu$  are discontinuous at the boundary between the particle and the medium. Figure 7.1 (b) shows a particle with optical constants  $\epsilon_p$  and  $\mu_p$  embedded in a medium with optical constants  $\epsilon_m$  and  $\mu_m$ . The illuminated plane wave generates an electric field  $E_1$  and a magnetic field  $H_1$  inside the particle. The particle radiates a scattered field in all directions, leading to an electric field of  $E_2$  and a magnetic field of  $H_2$  outside of the particle. The tangential components of the fields are continuous based on Maxwell's equations. At the arbitrary point  $x$  on the particle surface;

$$[E_2(x) - E_1(x)] \times \hat{n} = 0 \quad (7.3)$$

$$[H_2(x) - H_1(x)] \times \hat{n} = 0 \quad (7.4)$$

Important parameters that can be calculated with Mie theory is the absorption, scattering, and extinction cross sections for an arbitrary spherical particle. Since extinction is the sum of the scattered and absorption, the absorption cross section can be written as;

$$\sigma_{abs.} = \sigma_{ext.} - \sigma_{sca.} \quad (7.5)$$

These scattering and extinction cross sections can be calculated as;

$$\sigma_{sca.} = \frac{2\pi}{k^2} \sum_{n=1}^{\infty} (2n+1) (|a_n|^2 + |b_n|^2) \quad (7.6)$$

$$\sigma_{ext.} = \frac{2\pi}{k^2} \text{Re}(a_n + b_n) \quad (7.7)$$

The coefficients  $a_n$  and  $b_n$  are constant which relate to Ricatti-Bessel functions of order  $n$ .

Consequently, Au-NPs are popular in thin film solar cells since they enhance the light absorption by employing far-field or near-field effects associated with the localized surface plasmon resonance (LSPR) in the thin film [8]. Tremendous research work has been carried out on tuning the polymer solar cells with Au-NPs as shown in Table 2.1. However, no conclusive work has been conducted to optimize the PCE of PSCs using both CuO NPs and Au NPs incorporated in the active layer and hole transport layer respectively. This research work shows the increment of PCE and  $J_{sc}$  of P3HT/PC70BM bulk heterojunction solar cells by addition of gold (Au) and copper oxide (CuO) NPs in the PEDOT:PSS and active layer respectively. The combine effect of Au NPs in the PEDOT:PSS and CuO NPs in the P3HT/PC70BM on the device efficiency were studied by External quantum efficiency (EQE), atomic force spectroscopy (AFM), UV absorption and their current density- voltage (J-V) characteristics.

## 7.2 Results and Discussion

### 7.2.1 Performance Characteristics

The composition and structure of the fabricated cells is represented as: ITO/PEDOT:PSS (with various amount of Au-NPs)/P3HT/PCBM (with 0.6 mg CuO-NPs)/Al. The Table 7.1 shows the summarized photovoltaic parameters, such as  $J_{sc}$ ,  $V_{oc}$ , fill factor (FF), and PCE [9], of all the fabricated devices. Summarized data indicates that the  $V_{oc}$  remained nearly the same after adding Au-NPs into PEDOT:PSS layer. The  $J_{sc}$  shows an increment from 6.484 to 7.491 mA/cm<sup>2</sup>. FF values enhanced from 68 to 69.21%. These improved  $J_{sc}$  and FF influenced on PCE and it was enhanced from 2.963 to 3.51%. The incorporation of Au-NPs in the PEDOT:PSS layer contributed to about 18% increase in PCE due to the notably enhanced  $J_{sc}$  and improved

*FF*. With increasing concentrations of Au-NPs in PEDOT:PSS layer up to 0.06 mg, the PCE of the solar cells increased proportionally and then started to decline significantly beyond that point.

Table 7.1: Device parameters of ITO/PEDOT:PSS (with Au-NPs)/P3HT/PCBM/ CuO-0.6 mg NPs/Al solar cells.

Au-NPs(mg)	$J_{sc}(A/cm^2)$	$V_{oc}(V)$	FF(%)	PCE(%)
0	6.484	0.673	68.00	2.963
0.02	7.006	0.678	68.52	3.255
0.06	7.491	0.677	69.21	3.510
0.10	6.901	0.685	67.02	3.168
0.14	5.984	0.671	67.54	2.712
0.18	4.195	0.673	65.91	1.861

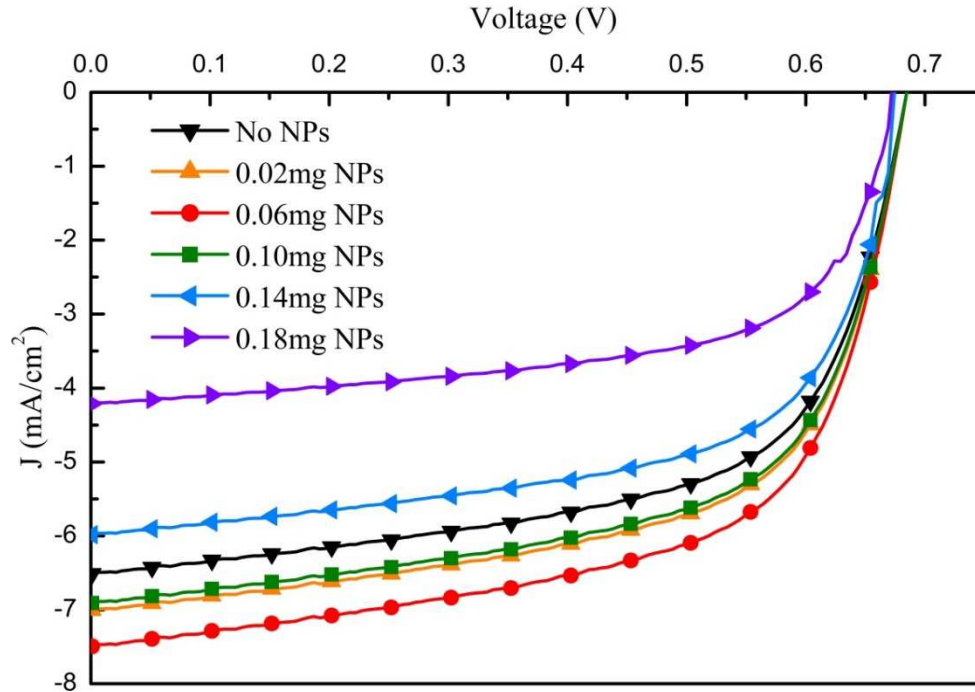


Figure 7.2:  $J$ - $V$  characteristics of hybrid polymer solar cells with different amount of Au NPs in PEDOT: PSS layer

The  $J-V$  characteristics of six PSC devices which contained different amounts of Au NPs in the PEDOT:PSS layer are shown in Figure 7.2. The performance of cells has improved with increasing Au-NPs in the PEDOT:PSS layer.

The  $J_{sc}$  has a linear relationship with the EQE of the solar cell devices (Equation 2.51). The EQE measures the ratio between the incident photons on the solar cell from the input source and the generated free charges carriers by the solar cell. EQE spectra of six different solar cells were first conducted to better elucidate improved  $J_{sc}$ . Corresponding EQE spectra for solar cells are presented in Figure 7.3. According to the Equation 2.51,  $\lambda_{min}$  and  $\lambda_{max}$  represent the starting wavelength (300 nm) and the ending wavelength (800 nm) in the EQE spectrum.

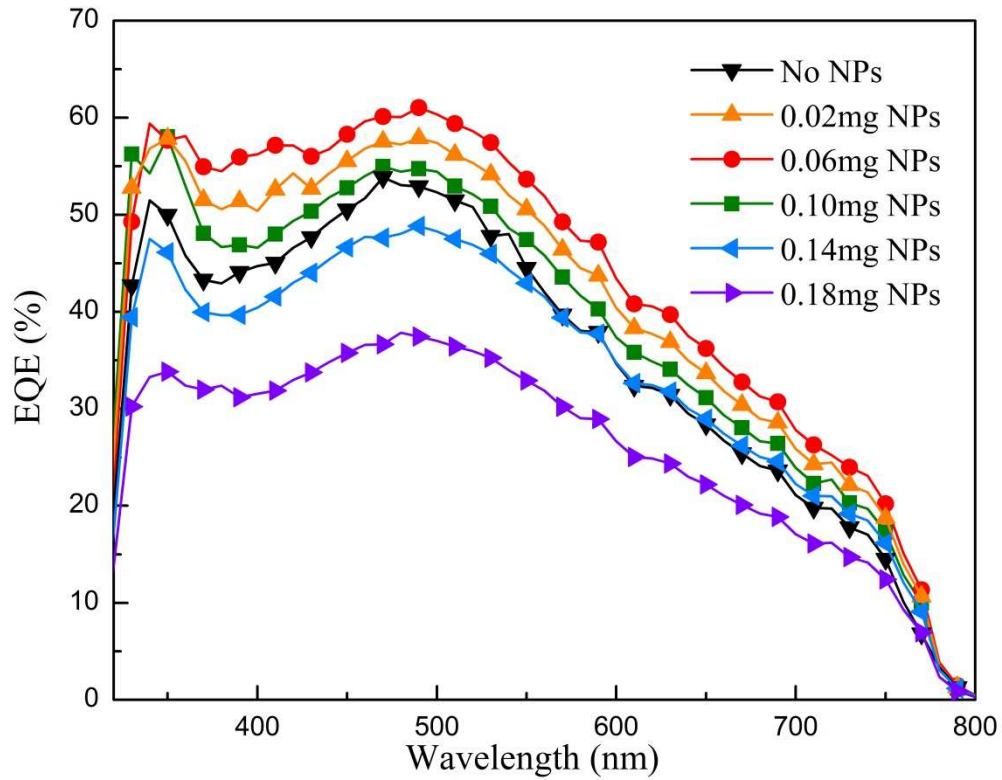


Figure 7.3: EQE of the hybrid solar cells with various Au NPs concentrations in PEDOT: PSS



The maximum EQE values were found to increase with the increasing amounts of Au-NPs in the PEDOT:PSS layer and then decreased as the amount of Au-NPs was increased beyond 0.06 mg. The  $J_{sc}$  values obtained for each cell followed a similar trend to EQE, which shows that the cells with 0.06 mg of Au NPs in the PEDOT:PSS layer exhibit the highest  $J_{sc}$  values. Figure 7.4 depicts the corresponding EQE and  $J_{sc}$  behaviour respectively. For successful photovoltaic operation, EQE can be determined by five major steps, these steps are composed with inherent efficiency components (equation 2.52) [10].

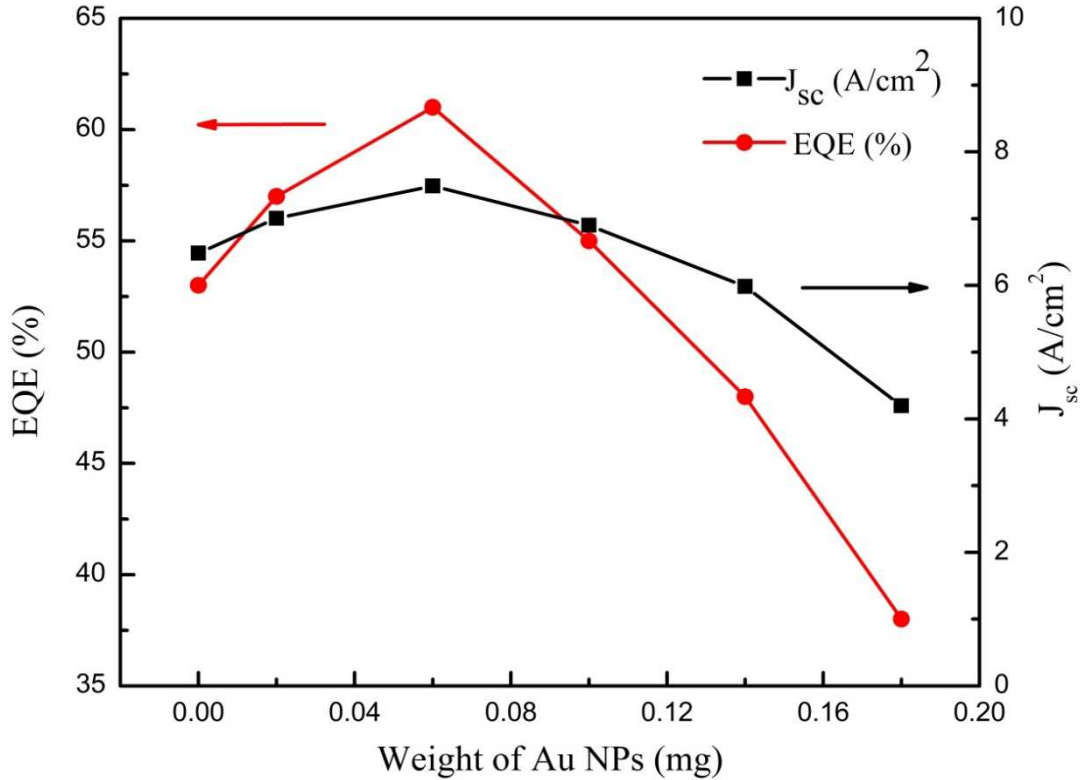


Figure 7.4: EQE and  $J_{sc}$  of the hybrid solar cells

Generally, photo absorption and carrier generating ability of a polymer thin film are represented by the photon absorption ( $\eta_A$ ) efficiency. The photo absorption of a semiconductor thin film is controlled by the energy band structure, light absorption coefficient and the

photoactive layer thickness of the device. The surface morphology of the thin film also will affect the absorbance of the bulk heterojunction photoactive layer. Free charge carriers, which are produced by the light absorption, contribute effectively to enhance the  $J_{sc}$  of a hybrid device [11]. In hybrid solar cell fabrication, metal and inorganic nanoparticles can be used to enhance the photon absorption yield and improve the surface morphology of the thin films. This indicates that generated free electron composition of the metal and inorganic nanoparticles can influence the  $J_{sc}$  of the polymer based devices as well.

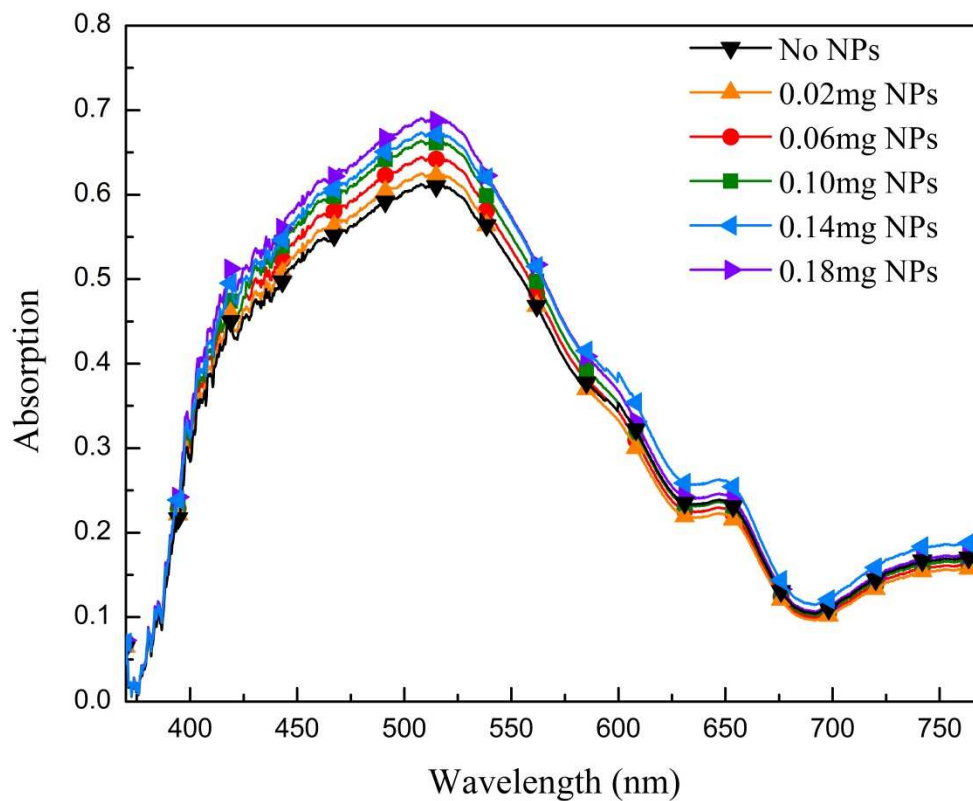


Figure 7.5: Optical absorption spectra of the hybrid solar cells with various Au NPs concentrations in PEDOT: PSS layer

To understand the  $J_{sc}$  enhancement, the UV-vis absorption measurements of the solar cells were obtained with and without Au-NPs in the PEDOT:PSS layer. The optical absorption spectra of Au nanoparticle incorporated PEDOT:PSS/ P3HT/PCBM/ CuO-NPs solar cells are shown in the Figure 7.5.

### 7.2.2 Plasmonic Effect of Au NPs in the PEDOT: PSS Layer

The physics of plasmonic effect of Au-NPs doped into the PEDOT:PSS layer, which has been studied previously by Fung et al. [12], is in good agreement with our data. The absorption spectra of the PEDOT:PSS/P3HT/PCBM/CuO-NPs devices did not show any significant improvement increase of Au NPs concentration in the PEDOT:PSS thin film, as shown in Figure 7.5.

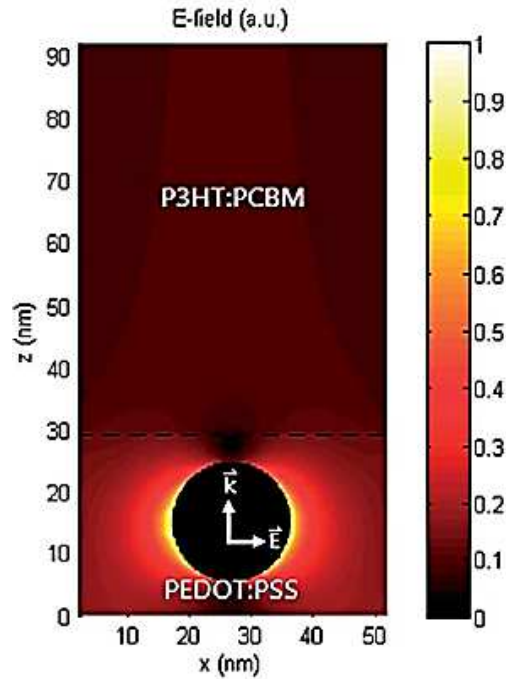


Figure 7.6: Electric field distribution in the PEDOT:PSS:Au NPs/ P3HT:PCBM PSCs [12]

This is caused by the strong near field surrounding the Au NPs due to the LSPR which is distributed horizontally through the PEDOT:PSS thin film, instead of penetrating upward into the P3HT/PC70BM layer, thus causing less optical absorption (Figure 7.6).

However, the EQE spectra of the PEDOT:PSS:Au NPs devices increased significantly with the Au-NPs. Addition of 0.06 mg Au-NPs exhibit the highest EQE of 61% at a wavelength of 500 nm, as shown in Figure 7.3. At higher concentrations of Au-NPs, the EQE started to decrease. This is in good agreement with the trend of  $J_{sc}$ . It appears that; there is a discrepancy between light absorption and EQE spectrum. According to Equation (2.52), in addition to the light absorption, factors such as exciton dissociation rates and charge collection efficiencies also contribute to the magnitude of EQE. Therefore, it can be concluded that electrical effects, instead of plasmonic effects, play a major role in the solar cell performance. Since PEDOT:PSS layer (with or without Au NPs) did not significantly contributed to the photon absorption, the light absorption measurements only represent the inherent light harvesting within the active layer composed of P3HT/PC70BM/CuO-NPs. The absorption spectra in Figure 7.5, which show insignificant difference, indicate that the light absorption in P3HT/PCBM is unaffected by the incorporation of Au-NPs.

The AFM surface morphology of the PEDOT:PSS:Au-NPs thin films with various concentrations of Au-NPs, is shown in Figure 7.7. The AFM images showed a clear enhancement in surface roughness with increasing the Au-NPs concentrations in PEDOT: PSS layers. The  $\sigma_{rms}$  of the control layers was 0.37 nm and it was enhanced to 1.26 nm in the samples containing 0.18 mg of gold NPs. The cell with 0.06 mg of Au-NPs exhibited a surface roughness value of 0.86 nm as the best performed solar cell (Table 7.2).

Table 7.2: The root-mean-square roughness  $\sigma_{rms}$ (nm) values of the Au NPs added PEDOT: PSS layers

Au-NPs(mg)	$\sigma_{rms}$ (nm)
0	0.37
0.02	0.55
0.06	0.86
0.10	1.02
0.14	1.11
0.18	1.26

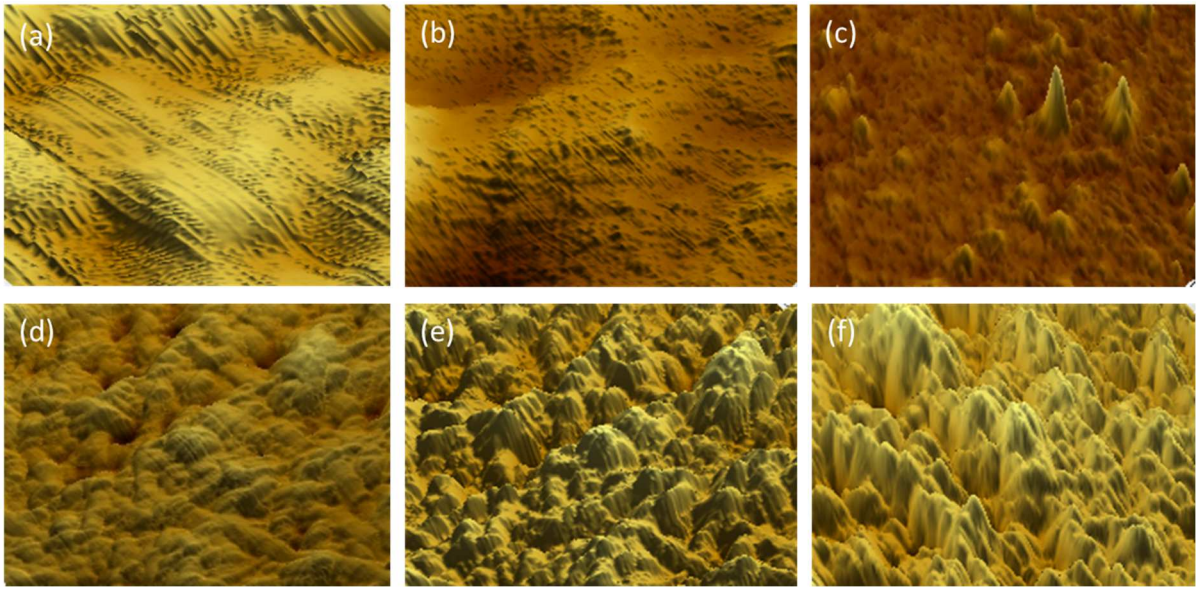


Figure 7.7: AFM images (non-contact mode) of PEDOT:PSS layers ( $2 \times 2 \mu\text{m}$  scans) with (a) No Au NPs, (b) 0.02 mg Au NPs, (c) 0.06 mg Au NPs, (d) 0.10 mg Au NPs, (e) 0.14 mg Au NPs, (f) 0.18 mg Au NPs

Fung et al. [12] as well as Hsu et al. [13] reported that a higher anode surface roughness leads to an increase in the interface contact area between the anode and the active layer in addition to shorter routes for holes to travel to the anode. This will cause to a higher efficiency of

hole collection; thus improving the  $J_{sc}$  of the devices. The holes collected at the anode can be independent from the external electric field by reducing the mean distance between the generated holes and the PEDOT:PSS which leads to higher fill factors ( $FF$ ). Li et al. [14] suggested that the excitonic dissociation is encouraged by the defects sites, generated from rough P3HT/PCBM surface. The increased  $\sigma_{rms}$  of the PEDOT:PSS layer with presence of Au-NPs increases the contacting area between PEDOT:PSS and P3HT/PCBM. Hence, it improves the hole collecting ability at the roughened interface between PEDOT:PSS and P3HT/PCBM molecules leading to enhanced device performance. The electron and hole movability in polymer films is an important factor which depends on the charge carrier hopping rate and it should be high enough to avoid the carrier recombination.

It was suggested by Kim et al. [15] that the Au NPs introduce dopant states in molecular structure which can produce hopping sites for the holes resulting in a higher hole mobility. However, further increase of Au NPs, exceeding the optimum amount of 0.06 mg, allows the Au NPs to penetrate to P3HT/PCBM film and changing nanoscale morphology within P3HT/PCBM blend. This morphology change causes a significant reduction of donor/acceptor contact surface. The modified donor/acceptor contact surface proportionally affects the excitonic dissociation, thus lowering the EQE and  $J_{sc}$  of the cells [16].

### **7.2.3 Effect of CuO NPs in the Active Layer**

The active layer of the device is composed of P3HT as the donor, PC70BM as the acceptor material and 0.6 mg of CuO-NPs. Even though the PEDOT:PSS layer did not exhibit absorption enhancement with or without Au-NPs, the P3HT/PC70BM active layer displayed a significant enhancement in absorption after incorporating CuO-NPs into the active layer. The absorption

spectrum of the reference cell, shown in Figure 7.5, is related to the absorption enhancement due to the CuO-NPs in the active layer. The P3HT molecules and CuO-NPs can generate excitons after absorbing the light photons with the energy than the  $E_g$  value (1.99 eV for P3HT and 2.14 eV for CuO-NPs) which reach to the P3HT/PC70BM and CuO-NPs/PC70BM interfaces respectively. Since there is no penetrated electric field to obstacle their motion through conjugated polymer, they diffuse by the force created with concentration gradient. This exciton diffusion to D/A interfaces is an essential phenomenon for exciton dissociation. The excitons which could not travel to D/A interface will not produce charge carriers (electrons or holes).

The PSCs with CuO NPs incorporated active layer can provide better routes for carrier transportation through inter-particle hopping sites in the structure which lead to an enhanced charge collection efficiency. It could be the possible reason behind the improved PCE of CuO-NPs incorporated PSCs. The optimum amount (0.6 mg) of CuO-NPs together with unbroken nanostructure creates an excellent interconnected network for the D/A nanoscale interlinking. Furthermore, the inter-nanoparticle hopping is encouraged by this system providing direct and efficient carrier transport routes for electrons and holes. Additionally, improved excitonic diffusion and carrier transport efficiencies imply that the life-time of the photo-generated carriers in detached state is enhanced, reducing the recombination probability. These factors will positively improve the  $EQE$  and  $FF$ , and thereby PCE.

The charge injecting possibility from the photo active layer to the electrodes is represented by the charge collection efficiency. The Au-NPs in the PEDOT:PSS also provide a better facility for hole collection at the anode. The magnitude of the conduction band energy level of the acceptor material is a critical parameter for better electron injection into the cathode. For possible electron injecting, this should be lower than the work function of donor. Correspondingly, the

magnitude of conduction band energy level should be greater than the work function of the anodic material for possible hole injection to anode. Figure 7.8 shows the energy level structure of the PEDOT:PSS/P3HT/CuO/PCBM device.

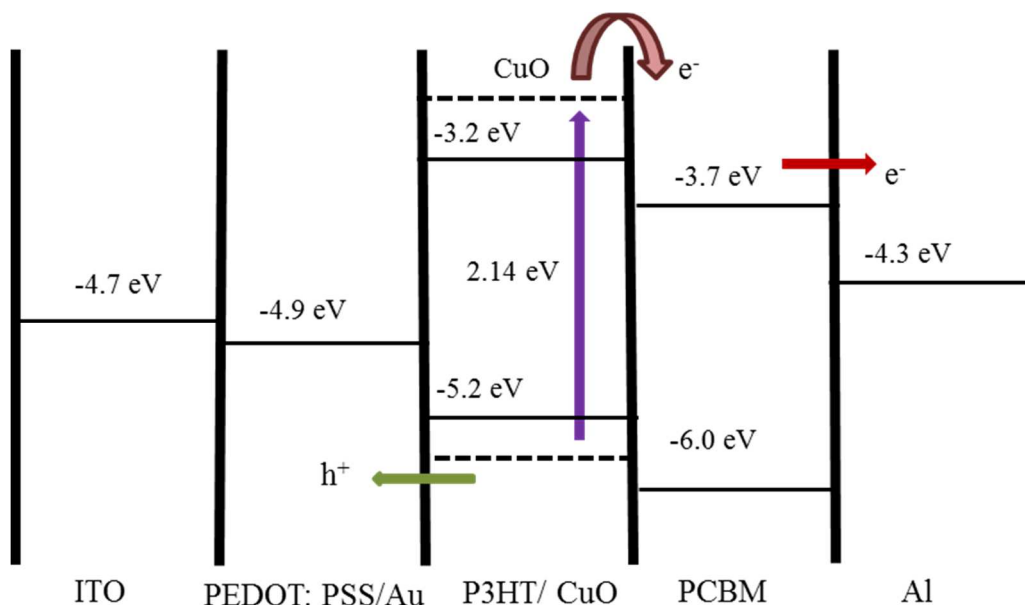


Figure 7.8: Energy band diagram of the P3HT/PCBM/CuO NPs device [17]

As illustrated in the diagram, conduction and valence bands of P3HT and PC70BM are most suitable for donor and acceptor pair. The energy levels of the conduction and valence bands of CuO NPs are comparable with the lowest unoccupied molecular orbital (LUMO) and highest occupied molecular orbital (HOMO) of PC70BM acceptor. Therefore, CuO-NPs/PC70BM are a suitable donor and acceptor pair and a semiconductor heterojunction can be formed between them. The energy band structures of the PEDOT:PSS and Au-NPs are compatible with the energy levels of P3HT providing a better route for holes. The created electrons in the active layer could be transferred from the conduction bands of the CuO and P3HT to PC70BM. Similarly the separated holes can be diffused from the valence bands of the CuO and P3HT to the ITO through



the Au-NPs and PEDOT:PSS. CuO is a p-type, direct transition band gap inorganic semiconductor providing a great photo absorption in the active layer. Hence, CuO-NPs can be used as an efficient electron injector in the active layer.

The Au and CuO-NPs incorporated nanostructures have excellent transport routes for free electrons and holes through different possible pathways: 1) the conventional interconnected PCBM molecules, 2) the incorporated Au and CuO NPs, 3) the partially crystalline PCBM/P3HT and PEDOT:PSS amorphous domains composed with CuO and Au-NPs respectively. These multiple routes increase the carrier mobility and thus significantly enhance the EQE and PCE.

#### **7.2.4 SEM and EDX Analysis**

The SEM image of layer structure of the fabricated Au-NPs/PEDOT:PSS/ CuO NPs/P3HT: PCBM device is shown in the Figure 7.9(b). The Au-NPs (18 nm diameter) added PEDOT: PSS layer has approximately 40 nm thickness. To eliminate the charge recombination losses, thickness of the P3HT/PCBM active layer was maintained at 100–150 nm. The EDX mappings of copper atoms in the active layer and Au in the PEDOT:PSS layer of the optimum solar cell with 0.06 mg of Au-NPs are shown in Figures 7.9(a) and 7.9(c). This can be used to indicate the distribution of CuO and Au NPs in the active layer and PEDOT:PSS layer respectively. It clearly illustrates that both NPs in the PEDOT: PSS and active layers are uniformly distributed avoiding agglomeration.

Open circuit voltage ( $V_{oc}$ ) has a linear relationship to energized band levels within D-A phases [17]. The  $V_{oc}$  of a hybrid solar cell can be increased by moving the polymer HOMO level further away from the vacuum level [18]. However,  $V_{oc}$  did not change significantly, possibly since the LUMOs of P3HT and PC70BM were constant; thus suggesting that the reduced

recombination due to increased carrier mobility did not improve  $V_{oc}$ . On the other hand, the HOMO energy level of P3HT in the active layer was not influenced by the Au-NPs in the PEDOT:PSS layer. Therefore, Au-NPs do not enhance  $V_{oc}$  in the solar cells, either.

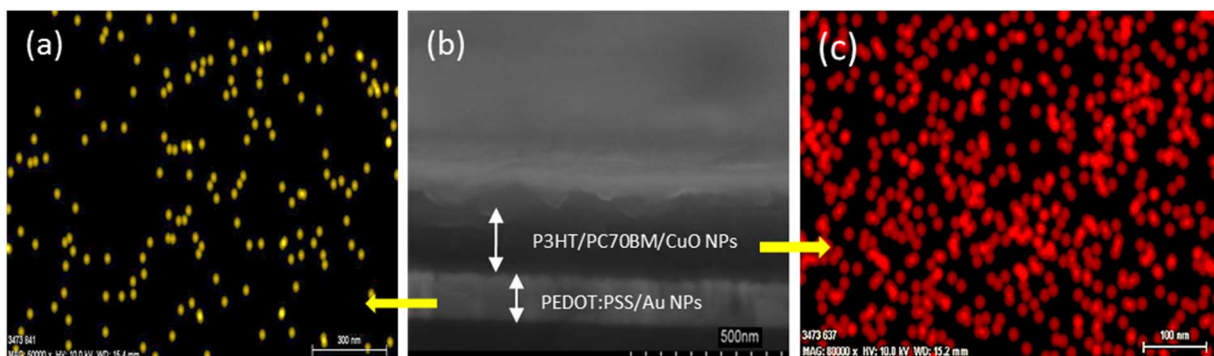


Figure 7.9: (a) EDX mapping showing the distribution of Au NPs in the PEDOT: PSS layer (b) SEM image of the hybrid polymer solar cell (c) EDX mapping showing the distribution of elemental copper in the P3HT/PCBM active layer

### 7.3 Conclusion

In this study, Au-NPs were added at different amounts to the PEDOT:PSS layer of solar cells containing 0.6 mg of CuO-NPs in the P3HT/PC70BM layer in order to increase the power conversion efficiency. The PCE increased from 2.96% to 3.51% in the cells containing 0.06 mg Au-NPs, which is equivalent to 18.5% improvement in efficiency. The higher performance is attributed to enhanced EQE, charge collection, exciton dissociation and interfacial distribution. The charge transport process was facilitated by providing better pathways in a continuous internal structure and hopping sites. The optical absorption spectrum did not change significantly in the presence of Au-NPs in the PEDOT:PSS layer due to the strong near field around Au-NPs. However, AFM analysis showed an increase in surface roughness of the PEDOT:PSS layer with Au-NPs, which indicates a larger contact area between PEDOT:PSS and the active layers. The

photon absorption and charge harvesting increased remarkably due to the presence of CuO NPs in the active layer. EDX mappings revealed a uniform distribution of both Au and CuO NPs in the PEDOT:PSS and active layers; respectively.

## References

- [1] Gunes, S., Neugebauer, H., and Sariciftci, N. S., 2007. Conjugated Polymer-Based Organic Solar Cells. *Chemical Reviews*, 107: 1324-1338.
- [2] Brown, M. D., Suteewong, T., Kumar, R. S. S., *et al.* 2011. Plasmonic dye-sensitized solar cells using core-shell metal-insulator nanoparticles. *Nano Letters*. 11: 438-445.
- [3] Kim, S. S., Na, S. I., Jo, J., *et al.* 2008. Plasmon enhanced performance of organic solar cells using electrodeposited Ag nanoparticles. *Appl. Phys. Lett.* 93: 073307(1-3).
- [4] Chou, S. Y., and Ding, W., 2013. Ultrathin, high-efficiency, broad-band, omni-acceptance, organic solar cells enhanced by plasmonic cavity with subwavelength hole array. *Opt. Express*. 21: 60-76.
- [5] Claire, M. C., Chen, J., Eun, C., Cho, L., Wang, V. and Younan X., 2011. Gold nanostructures: a class of multifunctional materials for biomedical applications. *Chem. Soc. Rev.* 40: 44–56.
- [6] Mahmoud, A. Y., Izquierdo, R., and Truong V. V., 2014. Gold Nanorods Incorporated Cathode for Better Performance of Polymer Solar Cells. *J Nanomater.* 2014: 464160.
- [7] Xiaohua, H., Mostafa, A. E., 2010. Gold nanoparticles: Optical properties and implementations in cancer diagnosis and photothermal therapy. *Journal of Advanced Research*. 1: 13–28.
- [8] Wright, M., and Uddin, A., 2012. Organic-inorganic hybrid solar cells: A comparative review. *Solar Energy Mater. Solar Cells*. 107: 87–111.
- [9] Chen, X., Zuo, L., Fu, W., *et al.* 2013. Insight into the efficiency enhancement of polymer solar cells by incorporating gold nanoparticles. *Sol. Energy. Mat. Sol.* 111: 1-8.
- [10] Gan, Q., Bartoli, F. J., and Kafafi, Z. H., 2013. Plasmonic-Enhanced Organic Photovoltaics: Breaking the 10% Efficiency Barrier. *Adv. Mater.* 25: 2385–2396.
- [11] Bundgaard, E., Shaheen, S.E., Krebs, F.C., Ginley, D.S., 2007. Bulk heterojunctions based on a low band gap copolymer of thiophene and benzothiadiazole. *Solar Energy Materials and Solar Cells*. 91: 1631–1637.
- [12] Fung, D.D.S., Qiao, L.F., Choy, W.C.H., C. Wang, W. E. I., Sha, F. Xie and S. He, 2011. Optical and electrical properties of efficiency enhanced polymer solar cells with Au nanoparticles in a PEDOT–PSS layer. *J. Mater. Chem.* 21: 16349–16356.
- [13] Hsu, M.H., Yu, P., Huang, J. H., *et al.* 2011. Balanced carrier transport in organic solar cells employing embedded indium-tin oxide nanoelectrodes. *Appl. Phys. Lett.* 98: 073308-1.

- [14] Li, G., Shrotriya, V., Yao, Y., and Yang, Y., 2005. Investigation of annealing effects and film thickness dependence of polymer solar cells based on poly3-hexylthiophen. *J. Appl. Phys.* 98: 043704-1.
- [15] Kim, K., and Carroll, D. L., 2005. Roles of Au and Ag nanoparticles in efficiency enhancement of poly(3-octylthiophene)/C60 bulk heterojunction photovoltaic devices. *Appl. Phys. Lett.* 87: 203113.
- [16] Krebs, F.C., Thomann, Y., Thomann, R., and Andreasen, J.W., 2008. A simple nanostructured polymer/ZnO hybrid solar cell-preparation and operation in air. *Nanotechnology.* 19: 424013.
- [17] Nguyen, B.P., Kim, T., and Park, C.R., 2014. Nanocomposite-Based Bulk Heterojunction Hybrid Solar Cells. *J. Nanomater.* 2014:243041.
- [18] Eisenhawer, B., Sensfuss, S., Sivakov, V., Pietsch, M., Andra, G., and Falk, F., 2011. Increasing the efficiency of polymer solar cells by silicon nanowires. *Nanotechnology.* 22: 315401.

## CHAPTER 8

### Conclusions and Future Work

#### 8.1 Summary and Conclusions

Low power conversion efficiency is a major concern of organic polymer solar cells since its initial development. It is believed that the lack of knowledge in several major steps; including exciton generation, exciton diffusion, exciton dissociation, charge carrier transportation, and charge extraction may have attributed to this difficulty in improving the power conversion efficiency. Our work focuses on enhancing the power conversion efficiency and expanding the current understanding of the above mechanisms in organic solar cells. In order to address these issues, nanoparticles of specific inorganic materials were incorporated in the polymer thin films. The experimental results suggest that these hybrid nanostructured thin films improve the performance of the devices through optical, electrical and morphological enhancement. The main research conclusions are summarized below:

1. CuO NPs incorporated P3HT/PC70BM thin films were used to improve optical, electrical and morphological properties. It was found that the CuO NPs enhance the optical absorption by enhancing the P3HT crystallinity in the P3HT/PC70BM thin films. Furthermore, CuO NPs improve the surface roughness of the solid state organic thin films. These factors proportionally enhanced the performance of the devices by increasing EQE,  $J_{sc}$  and PCE. However, excess amounts of CuO NPs reduced the electrical performance by increasing the film thickness and the agglomeration of the CuO NPs in the active layer.
2. Thermal annealing of P3HT/PC70BM/CuO NPs thin films at 150°C for 30 minutes further improved the morphology and crystallinity of the active layer. Furthermore, adding 0.6 mg of CuO NPs to the active layer resulted in the formation of the smallest polymer

crystallites, which was nearly 38.58 nm, after annealing. The surface roughness increased in the thin films with CuO NPs, which is a further indication of enhanced crystallinity.

3. ZnO NPs buffer layer which was assembled on the top of P3HT/PCBM/CuO active layer significantly increased the optical absorption of the devices. The electron affinity of the ZnO to the polymer semiconductors improved the dissociation rate of the excitons generated in the donor structure. Also, the ZnO NPs buffer layer improved the electron mobility, and charge collection at the anode. These factors increased the  $J_{sc}$  and PCE of the devices.
4. Au NPs which were incorporated in the PEDOT:PSS layer did not improve the optical absorption significantly of the devices; since the LSPR was distributed horizontally through the PEDOT:PSS thin film, instead of penetrating upward into the P3HT/PC70BM layer. However, the Au NPs improved the morphological properties; such as the surface roughness of the PEDOT:PSS films. In addition, Au NPs improved the electrical conductivity of the hole transport layer, thus reducing the series resistance. Consequently, the reduced resistance and enhanced morphology increased the EQE,  $J_{sc}$  and PCE.

## 8.2 Future Outlook

Throughout this work, it became clear that the incorporation of inorganic nanoparticles in the bulk heterojunction polymer solar cells is a promising approach to enhance the performance of organic solar cells. However, Future investigations are needed in several areas related to this work; such as: (1) to explore the effect of CuO NPs both in the PEDOT:PSS and active layers. Our findings revealed the effect of CuO NPs in the active layer. However, the incorporation of CuO NPs in the hole transport layer (PEDOT:PSS), along with CuO NPs are in the active layer,

could further improve the electrical and morphological properties of the PEDOT:PSS layer; (2) the incorporation of both CuO NPs and Au NPs in the active layer can further improve the light absorption in the device. Therefore, it is suggested that future studies explore the mutual effect of both NPs in the active layer.

In addition, further consideration needs to be given for increasing the long term structural stability and life time of the devices. For longer applications, the bulk heterojunction solar cell systems, which are not in equilibrium state, can undergo structural changes. The heating, due to solar radiation, can change the structure of the polymer chains and this heat does not contribute to charge carrier generation. Therefore, a main challenge will be to understand the effect of structural degradation from thermal aging of the polymer and to develop a solution accordingly. Similar to the morphological effect, the optical absorption also changes with time. Consequently, an investigation on the optical absorption performance with different time intervals is an essential future work in this field. Furthermore, the reduced series resistance is important to optimize the fill factor of the devices, therefore, work attempting to minimize these resistances is critical for improving the performance of solar cell devices.



# CURRICULUM VITAE

Aruna Wanninayake

Place of Birth: Sri Lanka

## Education:

Ph. D., University of Wisconsin, Milwaukee, 2016

Thesis: Nanostructured Organic/Inorganic Semiconductor Photovoltaics: Investigation on Morphology and Optoelectronics Performance

M.S., Physics, University of Wisconsin, Milwaukee, 2013

M.S., Cosmology, Creighton University, Nebraska, 2011

Research: “Fifth force and dark matter”

M.Sc., Materials Physics, University of Peradeniya, Sri Lanka, 2008

Research: “A study on  $\text{Cu}_2\text{O}/\text{Cu}_x\text{S}$  thin film solar cells”

B.Sc., Physics, Mathematics, University of Kelaniya, Sri Lanka, 2006

Research: “Development a PC interfaced bar code reader”

## Peer-Reviewed Journal Publications:

1. Aruna Wanninayake, Benjamin Church, Nidal Abu-Zahra. “Plasmonic Effect of Au Nanoparticles on Enhancing Power Conversion Efficiency of ZnO Buffer Layer Assembled Organic Solar Cells”, Solid State Communications, to be submitted, expected submission date: 01/20/2016
2. Aruna Wanninayake, Benjamin Church, Nidal Abu-Zahra. “Thermal Annealing Effect on ZnO Buffer Layer Assembled Organic Solar Cells synthesized with CuO Nanoparticles”, Physica Status Solidi (a), submitted, 01/08/2016
3. Aruna Wanninayake, Benjamin Church, Nidal Abu-Zahra. “Effect of ZnO Nanoparticles on the Power Conversion Efficiency of Organic Photovoltaic Devices Synthesized with CuO Nanoparticles”, Electronic Materials Letters, under reviewing, 12/11/2015
4. Aruna Wanninayake, Shengyi Li, Benjamin Church, Nidal Abu-Zahra. “Electrical and Optical Properties of Hybrid Polymer Solar Cells Incorporating Au and CuO Nanoparticles”, AIMS Materials Science, 3(1): pp35-50, (2016), doi: 10.3934/matricsci.2016.1.35

5. Aruna Wanninayake, Shengyi Li, Benjamin Church, Nidal Abu-Zahra. "Thermal Annealing of Bulk Heterojunction Polymer Solar Cells Incorporated with Au and CuO Nanoparticles", *International Journal of Renewable Energy Research*, 5(4): pp1080-1091, (2015)
6. Aruna Wanninayake, Subhashini Gunashekar, Shengyi Li, Benjamin Church, Nidal Abu-Zahra. "Performance Enhancement of Polymer Solar Cells using Copper oxide Nanoparticles", *Semicond. Sci. Technol.* 30: 064004 (7pp), (2015), doi:10.1088/0268-1242/30/6/064004
7. Aruna Wanninayake, Subhashini Gunashekar, Shengyi Li, Benjamin Church, Nidal Abu-Zahra. "CuO based Bulk Hetero-junction Solar cells: Investigations on Morphology and Performance", *J. Sol. Energy Eng.* 137(3): 031016 (7 pp), (2015), doi: 10.1115/1.4029542
8. Aruna P. Wanninayake, Subhashini Gunashekar, Shengyi Li, Benjamin C. Church, Nidal Abu-Zahra, "Effect of Thermal Annealing on the Power Conversion Efficiency of CuO-Bulk Heterojunction P3HT/ PC70BM Solar cells", *J. Sustainable Energy Eng.*, 3(2) pp. 107-126(20), (2015), doi: <http://dx.doi.org/10.7569/JSEE.2014.629521>

### **Seminar and Conference Proceedings:**

1. Nidal H. Abu-Zahra, Aruna P. Wanninayake, Polymer Solar Cells Synthesized with Copper Oxide Nanoparticles, ICEERET 2015: XIII International Conference on Energy Efficiency and Renewable Energy Technologies, Marrakech, Morocco April, (2015)
2. Aruna Wanninayake, Gintaras Duda, Using 5<sup>th</sup> Force Searches to Place Limits on New Scalars in the Dark Sector, APS April Meeting, California, USA (2011)
3. Aruna Wanninayake, Using 5<sup>th</sup> Force Searches to Place Limits on New Scalars in the Dark Sector, St. Alberts Day meeting, Creighton University, Nebraska, (2011)
4. Aruna P. Wanninayake, G. Duda, Dark Matter and Fifth Force, Nebraska Academic of Science (NAS), April (2011)
5. Aruna P. Wanninayake, T. J. Torpin, and G. Duda, Theoretical Determination of Form Factors Used in Dark Mater Studies, Nebraska Academic of Science (NAS), April (2010)
6. T. J. Torpin, Aruna P. Wanninayake, and G. Duda, Dark Matter Detection Methods, Nebraska Academic of Science (NAS), April (2010)
7. KMDC Jayathilake, W Siripala, WTMAPK Wanninayake, JKDS Jayanetti, Fabrication and characterization of Electrodeposited nanocrystalline / microcrystalline Cuprous Oxide thin films solar cells, Proc. 9<sup>th</sup> Annual Research Symp. 2008, University of Kelaniya (2008)